The Dissertation Committee for Arnoldo Delfino Estrada Jr. Certifies that this is the approved version of the following dissertation:

High-Resolution Measurement of Dissolved Oxygen Concentration In Vivo Using Two-Photon Microscopy

Committee:

Andrew Dunn, Supervisor

James Tunnell

Thomas Milner

Grady Rylander

David Ress

High-Resolution Measurement of Dissolved Oxygen Concentration In Vivo Using Two-Photon Microscopy

by

Arnoldo Delfino Estrada Jr., B.A.; M.S.E.

Dissertation

Presented to the Faculty of the Graduate School of

The University of Texas at Austin

in Partial Fulfillment

of the Requirements

for the Degree of

Doctor of Philosophy

The University of Texas at Austin

May 2011

Dedication

I dedicate this dissertation to my son Daryk Allan Estrada. Being your dad will always be my greatest accomplishment. Additionally, I dedicate this dissertation to my grand parents and my parents. It only took us thirty-nine years, but we did it!

Acknowledgements

I would like to thank my advisor Dr. Andrew K. Dunn. Thanks for your guidance through graduate school and this research effort. Your help was invaluable. Thanks also for providing an atmosphere where it was always okay to ask questions, even dumb ones. Thanks, to all of the members of my dissertation committee. Your inputs were extremely useful and have resulted in a much better research effort and a much better dissertation.

I offer my utmost gratitude to the members of my family. Thanks to my parents for tolerating a sometimes-odd child who would perform sometimes-dangerous experiments in and around the house. Thanks for never telling me to stop taking apart all of the household electronics. Instead of putting an end to all of my tinkering, you simply told me to be careful and put a fire extinguisher in my room. I appreciate all of the sacrifices you both have made to allow me to follow my interests in math and science. Yes it was me who burned the back yard and fence. But, it was in the name of science.

Thanks to Michelle Estrada. You have given me the best thing that has ever happened to me in our son. You have had a profound impact on the person I am today. Additionally, you made it much easier for me to follow my dream of getting a Ph.D. Thank you! If there is anyway I can reciprocate, I would be happy to do so.

Thanks to Eric Vasquez and Andy Morales. You guys have been brothers to me since we were kids. Thanks for always being there for me and giving me an escape from the pressures of graduate school when I needed it.

Thanks to my amazing sisters Maria Gonzalez, Letty Villareal and Julie Ruiz. I appreciate all of the love and support from you guys over the years.

Thanks to my incredible aunts and uncles. I am fortunate to have such a loving and supportive extended family. Whether it was money when I needed it most, a coat for the winters at Cornell, phone calls offering support, enthusiasm for my academic accomplishments, or simply words of encouragement, you all have helped to make this Ph.D. possible. Thanks for being such great examples of how to be a good uncle for my nieces and nephews. I hope I can repay your generosity to the next generation of our family.

Thanks to the many amazing people I have met along my way through graduate school. I would like to especially acknowledge the following people for making my years in graduate school great ones: The beautiful and talented Lonnissa Nguyen (aka. my graduate school sister), Ashwin Parthasarathy, Adrien Ponticorvo, Priya Veena, Prinda Wanakule, Eileen Dawson, Tracy Ooi, Jae Sook Park, Jinze Qiu, Michelle Flesher, Trey Flesher, Colleen Brock, and Cynthia Borden.

Lastly and most importantly I thank my son Daryk Estrada. You may not even be aware of the sacrifices you have made in order for me to receive my Ph.D. There were many occasions I wanted to spend more time with you but had to study for a test or spend the weekend doing experiments in the lab. I often wondered if it was right for me to pursue my Ph.D. given that I was losing so much time with you. Seeing the intelligent, thoughtful and strong young man that you have become over the last six years has put to rest any worries I had that the sacrifice of lost time together was too great. I am proud to be your dad.

High-Resolution Measurement of Dissolved Oxygen Concentration In Vivo Using Two-Photon Microscopy

Publication No._____

Arnoldo Delfino Estrada Jr., Ph.D.

The University of Texas at Austin, 2011

Supervisor: Andrew Dunn

Because oxygen is vital to the metabolic processes of all eukaryotic cells, a detailed understanding of its transport and consumption is of great interest to researchers. Existing methods of quantifying oxygen delivery and consumption are non-ideal for in vivo measurements. They either lack the three-dimensional spatial resolution needed, are invasive and disturb the local physiology, or they rely on hemoglobin spectroscopy, which is not a direct measure of the oxygen available to cells. Consequently, many fundamental physiology research questions remain unanswered. This dissertation presents our development of a novel in vivo oxygen measurement technique that seeks to address the shortcomings of existing methods. Specifically, we have combined two-photon microscopy with phosphorescence quenching oximetry to produce a system that is capable of performing depth-resolved, high-resolution dissolved oxygen concentration (PO_2) measurements. Furthermore, the new technique allows for simultaneous visualization of the micro-vasculature and measurement of blood velocity. We demonstrate the technique by quantifying PO_2 in rodent cortical vasculature under normal

and pathophysiologic conditions. We also demonstrate the technique's usefulness in examining the changes in oxygen transport that result from acute focal ischemia in rodent animal models.

Table of Contents

List of Tables

List of Figures

Chapter 1: Introduction

IMPORTANCE OF MEASURING DISSOLVED OXYGEN

Oxygen plays a unique and vital role in the metabolic processes of all eukaryotic cells. Due to oxygen's combination of high electronegativity and relative abundance in the atmosphere, cells have evolved to utilize oxygen as the ultimate electron acceptor in the primary chemical pathway used to produce high-energy ATP molecules. These molecules ultimately drive the majority of cells' energy consuming processes. In the absence of oxygen, cells cannot produce sufficient energy to sustain critical life processes and therefore quickly die. Because of oxygen's unique role in cellular respiration, a detailed understanding of its transport and consumption is of great interest to biomedical researchers.

Oxygen transport in complex organisms can be conceptualized as occurring on two spatial scales. On the macroscopic or system level, oxygen transport can be characterized best by looking at the cardiovascular system and hemodynamics. However, equally important is the microscopic or cellular level understanding of oxygen transport. At this spatial scale oxygen transport is best characterized by quantifying dissolved oxygen (DO) concentration gradients, diffusion and cellular respiration. Researchers must have the ability to quantify both hemodynamic parameters and intravascular and extravascular DO concentration to understand the complete process of oxygen delivery from the atmosphere to cells.

Measurements of hemodynamic parameters such as blood flow and oxygenated and deoxygenated hemoglobin concentration ([HbO] and [Hb] respectively) have been used to quantify the overall oxygen delivery to regions of tissue and to look at relative changes in oxygenation. Both clinicians who wish to ascertain the overall oxygenation

condition of a patient and researchers who wish to study oxygen transport and how it relates to cellular respiration commonly employ techniques for quantifying hemodynamic parameters [1-8]. Additionally, quantification of changes in hemodynamic parameters during functional activation of the brain can be correlated to changes in the metabolic rate of oxygen consumption; therefore, it is used by researchers to indicate changes in the cellular respiration of adjacent tissue due to activation. However, most of the commonly used methods for quantifying [HbO] and [Hb] cannot actually measure absolute concentration. Instead they measure changes in these parameters. For example, while oxygen saturation is the value most commonly reported in hemodynamic measurements, it is only a relative measure, defined as the ratio of oxygenated hemoglobin to total hemoglobin. Strictly speaking, oxygen saturation cannot tell you how much oxygen is available to tissue because it does not give you any information about the absolute concentration of oxygenated hemoglobin. If a patient were anemic, a measure of their oxygen saturation could still report a normal value. Additionally, measurement of hemodynamics can at best give relative changes in cellular respiration. Furthermore, because hemodynamic parameters are confined to the vasculature, a detailed view of regions of higher or lower cellular respiration in the adjacent tissue is not possible.

Similar to measurement of hemodynamic parameters, measurements of DO concentration, unbound to hemoglobin, have been used by researchers and clinicians to quantify oxygen transport and consumption. However in contrast to measurement of hemodynamics, measuring DO concentration can yield absolute quantification of the oxygen that is directly available to cells. Looking at spatial gradients in DO concentration and temporal dynamics of those gradients can yield direct, absolute information about oxygen transport and levels of cellular respiration down to the spatial scale of individual cells. Furthermore, in principle, the ability to measure DO

concentration is not confined to the vasculature, making it possible to follow oxygen transport and consumption all the way to the individual cell. This capability is necessary for researchers to fully understand the complete process of oxygen delivery and consumption.

UNITS OF DISSOLVED OXYGEN CONCENTRATION

Although it would be most straightforward to refer to DO concentration in the conventional units of moles per liter, the scientific literature often refers to DO concentration in humans and animals as the partial pressure of oxygen. In a mixture of ideal gases, each gas has a partial pressure, which is the pressure the gas would have if it alone occupied the volume. This concept in conjunction with Henry's law, which relates gas pressure, solubility and gas concentration in solution, provide the rationale for describing a gas concentration in terms of a partial pressure of gas. When one refers to a specific partial pressure of DO, it should be understood that they are referring to the resulting DO concentration when subjected to a gas pressure of that specific partial pressure value. The practice of referring to DO concentration in the body as a partial pressure of gas originated in early alveolar physiology research and has continued to the present. One shortcoming of this practice is that it assumes a constant temperature and solubility constant (Henry's law constant). Although this may be a reasonable assumption under normal physiologic conditions, under pathophysiologic conditions this assumption does not always hold true. Despite this fact, I have decided to keep with the most broadly accepted terminology and will refer to DO concentration as the partial pressure of oxygen (PO_2) and use units of millimeters of mercury (mmHg) in this dissertation.

NEED FOR A BETTER TECHNIQUE FOR MEASURING PO_2

There are currently many important research questions that cannot be answered because scientists lack an adequate technique for measuring PO_2 in vivo and with high resolution. It is surprising to learn that questions as fundamental as the primary site of oxygen delivery within the vasculature system remain unanswered. For years, scientists believed that oxygen delivery to tissue was simply the reverse process of oxygen uptake within the lungs. It has been demonstrated for some time that oxygen uptake in the lungs occurrs at the capillaries surrounding the alveoli of the lungs. For the most part, scientist believed that oxygen delivery also occurred at capillaries within the tissue. However, primarily due to advances in the ability to make accurate PO_2 measurements, new evidence has emerged that challenges the traditional understanding of how oxygen is delivered to cells. Recent research has shown that in fact the primary site of oxygen exchange appears to be at the arterioles [9, 10]. Contrary to what is taught in current physiology texts, recent research has also shown that post-capillary venules frequently have higher PO_2 values than capillaries [9, 10]. Although these latest studies have provided valuable new insights into the physiology of oxygen transport, important questions remain. For instance, recent evidence appears to suggest that microvascular arteriolar walls can consume very large amounts of oxygen [11]. It has been proposed that this ability provides a mechanism for the arterioles to regulate the amount of oxygen available to the tissue by serving as an oxygen sink during periods of low oxygen demand. More detailed PO_2 measurements are needed to confirm this hypothesis; however, the ability to make these more detailed measurements currently does not exist.

In a further attempt to achieve a more detailed understanding of oxygen transport on the microscopic scale, scientists have endeavored to develop better models of the transport process at the microvasculature. The traditional Krogh cylinder model, which relies on capillaries as the primary site of exchange, has been shown to not fully predict tissue oxygenation [10]. Recent efforts, which incorporate three-dimensional vasculature models from in vivo imaging, have shown promise at more accurately describing tissue oxygenation [12]. Unfortunately, researchers do not currently have adequate methods to measure PO_2 in vivo in a three-dimensional manner so as to quantify the accuracy of these new models.

Our understanding of blood oxygen level dependent, functional magnetic resonance imaging (BOLD fMRI) signals could also benefit from an improved PO_2 measurement modality. BOLD fMRI measurements have been used for visualizing increased levels of functional activation in human subjects while performing cognitive tasks. The source of contrast for BOLD is the differing magnetic resonance signatures of HbO and Hb. This method measures the hemodynamic response of the brain in response to activation. However, the measurement researchers generally are interested in is the level of neural activity associated with the BOLD signal. To date, researchers have not been able to conclusively establish how a given BOLD signal relates to a certain degree of neural activity [13-16]. Researchers have reasoned that if the neural-vascular coupling mechanism was better understood, then neural activity could be better linked to BOLD fMRI measurements. Since direct measurement of neural activity has proven very difficult, researchers are trying to measure changes in PO_2 as an indicator of changes in cellular respiration- and, by extension, changes in adjacent neural activity [17]. Again, inadequate methods of measuring PO_2 have hampered researchers' efforts.

Further problem domains that are in need of better PO_2 measurement capabilities include cortical spreading depression research [18-20], tumor angiogenesis research[21, 22], and stroke research [23, 24].

EXISTING PO_2 MEASUREMENT TECHNIQUES

Clark Electrode Oximetry

The most ubiquitous method for measuring PO_2 in biological samples is currently the Clark electrode. Invented by Leland Clark in 1956, this electrode consists of a cathode and anode immersed in an electrolyte solution, all encased in a membrane through which oxygen can diffuse.

Figure 1: Example of Clark electrode

The Clark electrode works based on an electrochemical reaction that occurs when a small negative bias voltage is applied between the reference lead (anode) and the sensing lead (cathode). When the bias voltage is set appropriately, oxygen is reduced at the cathode at a rate that is proportional to the concentration. The current through the cathode will therefore be a linear indicator of the PO_2. The advent of the Clark electrode allowed researchers to perform repeated, in situ PO_2 measurements in tissue for the first time. The original design was optimized for tissue measurements by making the tip smaller (< 50 μm). This improvement provided the electrode with a fast response time, high spatial resolution and low oxygen consumption.

Although the Clark electrode has led to advances in our gross understanding of oxygen transport both in the vasculature and in the extravascular regions, it is not well suited for investigating the oxygen transport system on the microvascular scale. The primary reason for this is that the tip must be inserted into the region being measured. Therefore multiple measurements, distributed throughout a region of tissue, would be highly invasive and would disrupt the physiology. Furthermore placing the electrode tip accurately throughout some volume of tissue would be difficult thus preventing rapid measurements at different locations.

Electron Paramagnetic Resonance Oximetry

Electron paramagnetic resonance (EPR) oximetry is a magnetic resonance based method that uses a paramagnetic electron spin probe that interacts with molecular oxygen [25]. In a fashion similar to nuclear magnetic resonance, the magnetic moments of the spin from unpaired electrons align with an applied magnetic field. After a radio frequency excitation source is applied, a net absorption occurs in the spin probe, which

flips more lower energy than higher energy magnetic moments to the antiparallel direction. The rate at which the magnetic moments relax is proportional to PO_2. Therefore, with proper calibration, PO_2 measurements can be made by quantifying the relaxation rate of the electron spin magnetic moments. The advantages of this technique are that it can produce three-dimensional PO_2 spatial maps, measure interstitial and intravascular PO_2, and if the correct spin probe is used, be noninvasive. However, the biggest drawback of the technique is that the spatial resolution for in vivo measurements is at best 200 μm [26]. Because oxygen is primarily delivered to cells through vasculature smaller than this size, EPR cannot currently be used to investigate oxygen transport down to delivery to cells.

Phosphorescence Quenching Oximetry

For approximately 25 years, scientists have used the phosphorescence quenching oximetry (PQO) technique to make in situ DO measurements in biological samples [27-30]. The advent of this technique has led to significant advances in our understanding of the details of oxygen transport and consumption [9, 10]. PQO is an optical technique that can be used to make repeated PO_2 measurements both in the vasculature and in the extravascular region. Because it is an optical technique, it offers high spatial resolution. Additionally, it has adequate temporal resolution to observe dynamic processes related to oxygen transport, consumption and cellular respiration.

PQO relies on the use of a phosphorescent molecular probe molecule that is optically excited from the ground state S_0 to its singlet state S_1 (figure 1). Because the probe molecule is phosphorescent, it will quickly undergo an intersystem crossing and transition to the long-lifetime triplet state T_1.

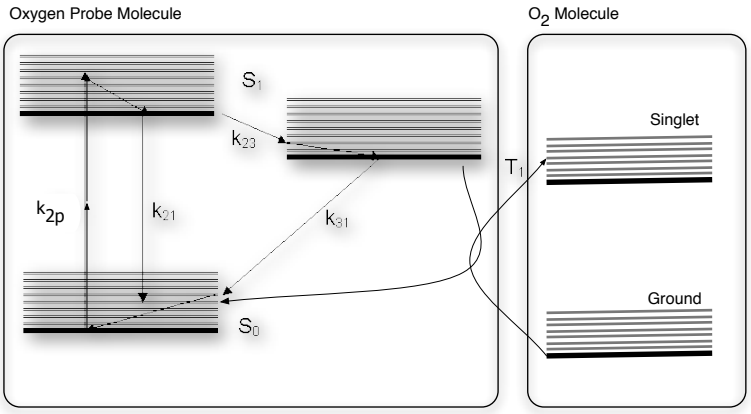

Figure 1: Diagram of phosphorescence quenching by oxygen

In the absence of oxygen, the molecule can relax to the ground state from T_1 either by emitting a phosphorescence photon or via non-radiative decay mechanisms. In either case, the overall rate at which relaxation to S_0 occurs will be a property of the phosphorescent probe molecule and can be represented by the rate constant k_{31}. If N_T represents the number of phosphorescent probe molecules in T_1, depopulation of those molecules from T_1 is described by the following differential equation:

$$\frac{dN_T}{dt} = -N_T k_{31} \qquad (1)$$

$$N_T(t) = N_T(0) \cdot e^{-k_{31}t}$$

The phosphorescent decay lifetime is related to the rate constant as $\frac{1}{\tau_0} = k_{31}$, where τ_0 is the unquenched lifetime.

In the presence of oxygen, probe molecules in their triplet states can collide with dioxygen molecules and occasionally transfer their energy. When this type of collisional quenching occurs it creates an additional mechanism for the phosphorescent molecules to relax to the ground state. The differential equation describing the rate of relaxation will have an additional term:

$$\frac{dN_T}{dt} = -N_T(k_{31} + k_q PO_2) \qquad (2)$$
$$N_T(t) = N_T(0) \cdot e^{-(k_{31}+k_q PO_2)}$$

In the equation above k_q is the rate constant that describes the dynamics of the energy exchange process due to collisional quenching. The rate at which excited probe molecules relax from the T_1 state will be the intrinsic relaxation rate plus the rate of collisional quenching. Furthermore the rate of collisional quenching will be proportional to the PO_2. In the presence of oxygen, the observed phosphorescence lifetime is therefore related to the rate constants and PO_2 as:

$$\frac{1}{\tau} = k_{31} + k_q PO_2 \qquad (3)$$

Since k_{31} is simply the unquenched lifetime, equation 3 can be rewritten as:

$$\frac{1}{\tau} = \frac{1}{\tau_0} + k_q PO_2 \qquad (4)$$

Equation 4 is known as the Stern-Volmer equation and relates the observed decay lifetime to the local PO_2. To use the Stern-Volmer equation to determine PO_2, two calibration parameter-the unquenched lifetime and quenching constant-must first be determined.

Although PQO has proven to be a very powerful technique for quantifying DO, its major limitation is that measurements are depth-integrated. As such, observed phosphorescent decays are always weighted averages over the imaging depth dimension. Making PO_2 measurements with high spatial resolution in the depth-dimension is therefore impossible in all but a few carefully selected experimental conditions. In general, the PQO technique, as it exists today, has been used to make PO_2 measurements on the surface of various tissues [31-35]. The limitations of PQO have prevented the technique from being applied as a tool to look at oxygen transport on the microscopic scale over an extended volume of tissue.

COMBINING TWO-PHOTON MICROSCOPY WITH PQO

Because oxygen diffusion is a three-dimensional phenomenon, a technique capable of three-dimensional measurements is needed to fully characterize oxygen transport. Furthermore, since oxygen exchange primarily occurs in the microvasculature, only a technique that has a spatial resolution of a few microns would adequately characterize the oxygen transport process down to the delivery of oxygen to cells. The goal of this research project is to combine two-photon microscopy (TPM) with PQO in order to develop a technique that is capable of detailed DO measurements making this detailed characterization possible. The rationale for combining these two techniques is that PQO would benefit from the inherent spatial confinement associated with two-

photon excitation [36-38] thus making the technique depth-resolved. Aside from being depth-resolved, the PQO technique should function as it does in the one-photon case since the phosphorescence and quenching processes are largely independent from the excitation process. Therefore, researchers will still benefit from work done previously to establish PQO as a mature and effective DO measurement technique. Additionally, all of the strengths of TPM for high-resolution imaging of the microvasculature and quantification of blood flow will prove useful in characterizing oxygen transport and consumption on the cellular scale.

Combining TPM with PQO will in principle result in a technique that has micron-scale resolution, is inherently three-dimensional and provides absolute DO values. Although Mik et al. [39] demonstrated the first combination of two-photon excitation with PQO, the technique they presented did not allow for imaging in conjunction with PO_2 measurement. Therefore their technique could not be used to characterize anatomy along with oxygen transport.

SPECIFIC AIMS

In this dissertation, I present our work to generate a novel technique that combines the advantages of TPM and PQO. I discuss our efforts to optimize the technique in which we evaluate different phosphorescent oxygen probes, techniques for measuring decay lifetimes and instrumentation options. More specifically, the aims of this research were as follows:

1. Develop the hardware and software needed for an imaging system capable of three-dimensional, image-guided intravascular PO_2 measurement based on TPM and the phosphorescence quenching oximetry technique.

2. Optimize the system to provide the best PO_2 sensitivity, as well as the best temporal and spatial resolution while minimizing the potential impact to the physiology.
    a. Evaluate different combinations of porphyrin-based vs ruthenium-based oxygen probes and time-domain vs frequency-domain lifetime determination in vitro.

3. Demonstrate the technique by producing a high-resolution, depth-resolved mapping of intravascular PO_2 in mouse cortex under normal physiological conditions.

4. Characterize the blood velocity and PO_2 changes in vessels adjacent to highly localized thrombosis in mouse cortex.

Chapter 2: Instrumentation and Methods

INTRODUCTION

Combining PQO with TPM requires the addition of a lifetime detection system to the basic two-photon microscope instrumentation. The design of our optics and instrumentation was made to be versatile so that we could evaluate various phosphorescent molecular oxygen probes and lifetime determination techniques. We chose to limit ourselves to palladium-porphyrin-based oxygen probes and ruthenium-based oxygen probes, as these are the most used and best characterized in the scientific literature for PQO. Since the two types of probes have lifetimes that differ by three orders of magnitude, the timing requirements of the lifetime excitation system are drastically different. We chose to include a second excitation source whose repetition rate was well suited for ruthenium-based oxygen probes. In this chapter, I present the details of our custom-built two-photon microscope setup and the lifetime detection system we implemented. I also discuss some of the methods we employed to achieve our unique oxygen-transport measurement capabilities.

LIFETIME DETERMINATION METHODS

Time-Domain Lifetime Determination

The phosphorescence decay lifetime (τ) is defined as the time it takes the phosphorescence intensity to decay by a factor of e^{-1}. The most straightforward manner of quantifying this value is using the time-domain method. In this method, we excite the phosphor with an impulse of excitation light, measure the phosphorescence intensity decay, and fit the data to a single exponential decay model (equation 5).

$$I(t) = I_0 \cdot e^{-t/\tau} \qquad (5)$$

τ is therefore determined from the fitting algorithm. Figure 3 is a plot of our decay data, which illustrates the process. A potential shortcoming of this method is that it can be inefficient or damaging since the excitation occurs as a low duty cycle, high peak power process.

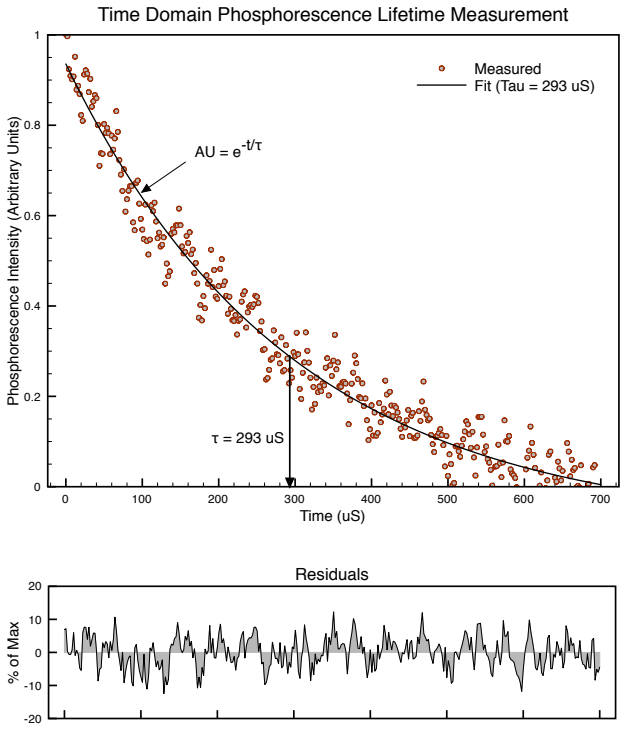

Figure 3: Illustration of time-domain lifetime determination method.

Frequency-Domain Lifetime Determination

Another method often used to determine the decay lifetime is the frequency-domain method. This method can be understood by thinking of the phosphor as an optical low-pass filter. Its decay behavior in response to a short pulse of excitation light is essentially the phosphor's impulse response. The cutoff frequency of this low-pass filter can be thought of as approximately $f_c = 1/2\pi\tau$. The behavior of the system in response to a sinusoidally modulated excitation signal can be analytically determined by taking the convolution of the excitation signal with the impulse response [40]. Doing so confirms that the phosphorescence will be phase-shifted with respect to the excitation, and its modulation depth (defined as the ratio of amplitude to offset of the sinusoid) will be reduced as we drive the system with frequencies beyond the cutoff frequency. The reduction of the modulation depth, which is commonly known as the demodulation factor, is quantified as the ratio of modulation depth of the resulting phosphorescence to the modulation depth of the excitation. This behavior is exactly analogous to what would be seen in a standard Bode plot of an electrical low-pass filter. The magnitude of phase shift and demodulation factor can be used to determine the decay lifetime for a given excitation modulation frequency. Equation 6 describes the relationship:

$$\begin{aligned} I_{phos} &= \text{Impulse Response} \otimes \text{Excitation} \\ &= \int_0^\infty I_0 e^{-t/\tau} \cdot \left[a + b\cos(\omega(t-t')) \right] dt' \\ &= A + B(\omega,\tau)\cos(\omega t - \phi_1) \text{ where } \tan(\phi_1) = \omega\tau \end{aligned} \tag{6}$$

where $\omega = 2\pi f$. The demodulation factor will be:

$$M_1(\omega,\tau) = \frac{1}{\sqrt{1+\omega^2\tau^2}} \qquad (7)$$

The phase shift and modulation depth are determined from fitting the phosphorescence signal to equation 6. Figure 4 illustrates the process. The lifetime is then calculated by taking the phase shift and or demodulation information together with the mathematical model.

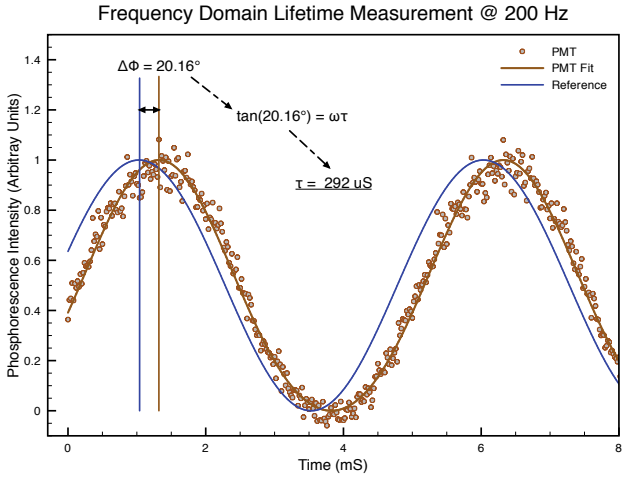

Figure 4: Illustration of frequency-domain lifetime determination using phase shift information.

MOLECULAR OXYGEN PROBES

Porphyrin-Based Molecular Oxygen Probes

Porphyrin-based oxygen probes are the predominant molecular probes used for *in vivo* PQO. In fact, the technique was first developed and published using a porphyrin probe. It's use for *in vivo* and *in vitro* oxygen sensing is very well established in the literature [9, 27, 28, 31, 41]. Furthermore, the technology has been successfully commercialized. Porphyrin-based fiber optic oxygen point measurement probes are

becoming the new standard for in situ oxygen sensing. These types of probes have long lifetimes (~100s of us) and quenching constant values that make them well suited for measurement of physiological PO_2 [27, 28]. However, the long lifetimes of porphyrin probes make DO imaging impractical for point scanning techniques such as 2PM. Therefore, a porphyrin-based oxygen probe combined with 2PM would necessitate point sampling of DO.

Ruthenium-Based Molecular Oxygen Probes

Although less well established in the scientific literature for *in vivo* measurements, ruthenium-based oxygen probes also show promise for this application. Ruthenium oxygen probes have recently started gaining the research community's attention because they have much shorter lifetimes than porphryin probes [42, 43]. Ruthenium-based fiber optic oxygen point measurement probes are also commercially available. These types of probes have lifetimes on the order of hundreds on nanoseconds. Ruthenium-based measurements may therefore have a temporal resolution that is three orders of magnitude better than porphyrin-based measurements and would allow true imaging of DO as opposed to point sampling. Furthermore, our preliminary testing shows that ruthenium probes have significantly higher two-photon action cross-sections than porphyrin-based probes (data presented in Chapter 5). The potential benefits of ruthenium are mitigated by the fact that its short lifetime makes it less sensitive to changes in DO. Additionally, ruthenium has been shown to be toxic to animals in high doses, and it has a high clearance rate by the kidneys [43]. Its usage *in vivo* is not well established in the literature, nor is its quenching constant *in vivo* well characterized. However, Paxian et al. have shown that by using a continuous infusion protocol, it is

possible to perform ruthenium-based PO_2 imaging *in vivo* while avoiding toxicity effects [43].

CONSTRUCTION OF THE TWO-PHOTON MICROSCOPE

It is assumed that the reader understands the basic principles of two-photon microscopy. The following references serve as good review articles if needed [37, 38, 44].

To a large extent, the construction of our microscope followed the guidelines presented by Tsai et al. [45] . This book chapter discusses how to build an upright two-photon microscope suitable for *in vivo* imaging. We deviated from these guidelines in the ultimate design of our collection optics. Since publication of the chapter, researchers have begun emphasizing the need to use collection optics that can detect all of the photons coming from the back aperture of the objective when imaging in highly scattering samples. As will be discussed below, the second iteration of our collection optics achieves much higher collection efficiency than the optics we designed when following the guidelines from the book chapter.

DIAGRAM

The following is a diagram depicting the essential elements of our two-photon microscope.

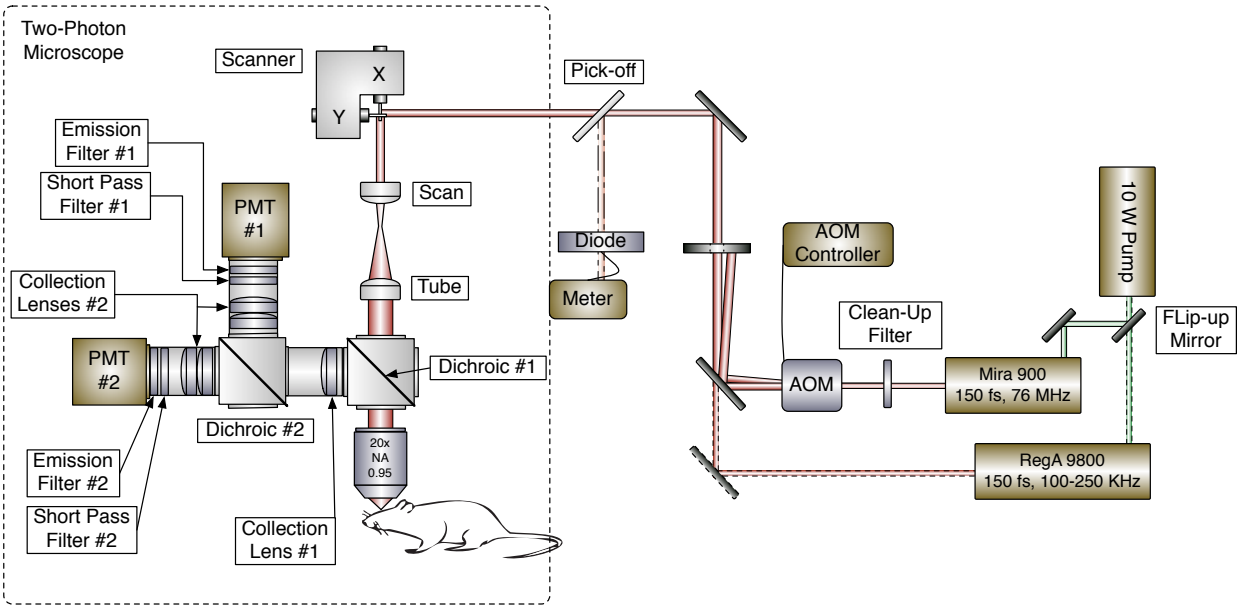

Figure 5: Two-photon microscope diagram.

Excitation Optics

Excitation Sources

The primary excitation source used for two-photon imaging is a Ti:Sapphire ultrafast laser system consisting of a Coherent, Mira 900 pumped by a 10 Watt Coherent, Verdi. The Mira 900 is tunable from 760 nm to 920 nm and has an average power of 2 Watts at 800 nm. When modelocked, the Mira 900 produces 150 fs pulses (26 nJ per pulse) at 76 MHz. The pulse width was measured using a Swamp Optics, Grenouille 8-50.

We found it necessary to use a Chroma Technology, HQ780-LP long-pass filter to block residual fluorescence coming from the Mira 900. The filter transmits wavelength above 750 nm. The residual fluorescence from the laser is collinear with the laser light

and eventually is scattered by the first dichroic and objective, where it can be detected by our photomultiplier tubes (PMTs). Although this fluorescence is six orders of magnitude lower than the laser light, it extends down to ~730 nm, which is in the pass-band of our 700 nm emission filter. Without the high-pass filter to block this fluorescence, imaging with the 700 nm filter results in a poor signal to background ratio; therefore, it produces low quality images.

In addition to the Mira 900, our system includes a Coherent, RegA 9800 regenerative amplifier excitation source. The RegA 9800 is pumped by the same 10W Verdi. The RegA 9800 is setup to operate at 800 nm and has an average power of 1.5 W. Its repetition rate can be set to 100 KHz or 250 KHz. The pulse width is 150 ns. The resulting pulse energy is ~ 6 μJ. Excitation source selection is accomplished by a flip-up mirror, which directs the pump laser to either the Mira 900 or the RegA 9800.

Beam Expander

After employing the laser scanner, we use a Keplerian telescope beam expander to properly fill the back aperture of the microscope objective. The aperture of our laser scanning system is 3 mm, while the back aperture of our primary objective is 17 mm. A beam expansion of a factor of 6 is accomplished by using a f = 20 mm (Thorlabs, LB1450-B) scan lens and a f = 125 mm (Thorlabs, LB1106-B) tube lens separated by 165 mm. Additionally, it is desirable to image the mirrors from the laser scanner onto the back aperture of the objective. When this imaging requirement is met, the angular displacement produced by the scanner will not result in a lateral displacement of the expanded beam on the back aperture. To image the scanning mirrors on the back aperture, the scan lens is placed 20 mm from the laser scanning mirrors, and the back

aperture of the objective is placed 125 mm from the tube lens. Failure to image the scanning mirrors on the back aperture results in vignetting of the images, due to excitation power is loss on the periphery of the back aperture as the beam is laterally displaced during scanning.

Laser Scanning System

Our laser scanning system is a pair of Cambridge Technology, 6125HB galvanometer scanners driven by Cambridge Technology, 671215H-1HP servo driver amplifier boards. We chose 3mm silver-coated mirrors for our scanning system. However, in hindsight, 5 mm mirrors would have been a more appropriate choice as optical power loss from the scanner aperture would be reduced and we do not scan fast enough to make the reduced inertia of the 3 mm mirrors a critical issue. Additionally, 5 mm mirrors would need less beam expansion, which would allow for thinner lenses with less aberration. A pair of high-power 28 V power supplies is used to energize the servo driver amplifier boards.

Collection Optics

Microscope Objective

It has been demonstrated that for two-photon imaging in highly scattering samples, better contrast and deeper imaging can be achieved using low magnification objectives with high numerical aperture (NA) [46, 47]. Oheim et al. report a factor-of-10 increase in collected fluorescence at large depths when imaging with a 20x objective vs. a 60x objective, with similar NA. The reason for this result is that when imaging deeply in highly scattering samples, such as tissue, the fluorescence photons appear to originate

over an extended area. Since lower magnification objectives will have greater fields of view, they will therefore be able to "see" more of the scattered photons, which exit the tissue over an extended region. A high NA is of paramount importance for optimal fluorescence signal collection because it will provide a greater acceptance angle for the emitted fluorescence. Additionally, the higher NA results in a smaller excitation spot size, thus yielding higher-resolution images.

Our primary two-photon imaging objective is an Olympus XLUMPLFL20X-W2. This is a 20X water immersion objective with an NA = 1.0. Such a low magnification given the large NA is accomplished by having a 17 mm back aperture. The large back aperture presents an optics design challenge when trying to relay all of the light from the objective to our PMTs.

Photomultiplier Tubes

In order to maximize signal-to-background ratio, and therefore image quality, as well as to maximize imaging depth, the collection optics must have the greatest collection efficiency possible. As discussed above, maximization begins with having as high an NA objective as possible. For highly scattering samples, greater collection efficiency is achieved with lower magnification objectives. Once the objective collects the emitted photons, great care must be taken to ensure that these photons reach the detectors (PMTs, in our case). Instructions for how to build two-photon microscopes describe the optimal collection optics design as the one where the back aperture of the objective is imaged onto the detector [45]. This arrangement ensures that photons emanating from the back aperture of the objective at various angles will converge again at the detector. In highly scattering conditions, the fluorescence photons will appear to come from an extended

region on the surface of the sample and have an isotropic angular distribution [46, 47]. When this light is collected by the objective and propagates back through the back aperture, it will not be collimated, but will have an angular distribution whose maximum angle will be determined by the properties of the objective. Figure 6 demonstrates the angular distribution of light propagating from the back of an objective. For the Olympus 20X objective that we use as our primary imaging objective, the maximum angle from the back aperture was experimentally determined to be between 12 and 15 degrees (personal communication with Dr. Chris Schaffer of Cornell University).

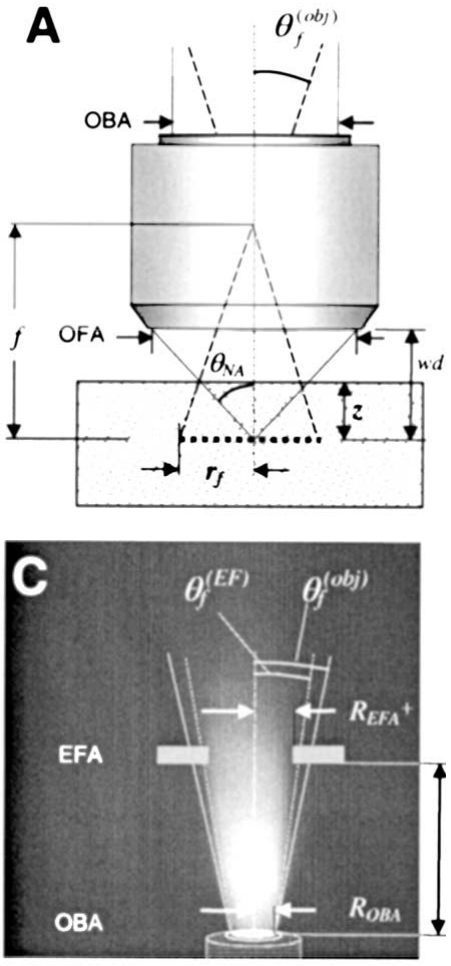

Figure 6: Depiction of the angular distribution of light coming from back aperture of objective. Reproduced from [46].

Since the back aperture of our Olympus objective (described above) is 17 mm in diameter, and the detecting surface of our PMT is 5 mm by 5 mm, collection optics must produce an image of the back aperture onto the detector that is minified by a factor of 3.4. The product of the area of the back aperture and the solid angle of the light cone exiting the back aperture (known as the etendue or $A\Omega$ product) must be conserved from object plane to image plane. Minification by 3.4, implies that the solid angle of the light cone from the back aperture as it is imaged onto the detector will be increased by a factor of 3.4^2. Large acceptance angle PMTs are thus needed to accommodate this expansion.

Our original microscope design incorporated Hamamatsu H7422P-40 PMTs. These PMTs offer the best combination of high quantum efficiency and low dark current (~ 100 counts / s). To achieve such a low dark current, the manufacturers put a thermoelectric cooling element and PMT detector unit in an enclosure with an optical window. This design minimized the acceptance angle of the detecting element in the PMT module.

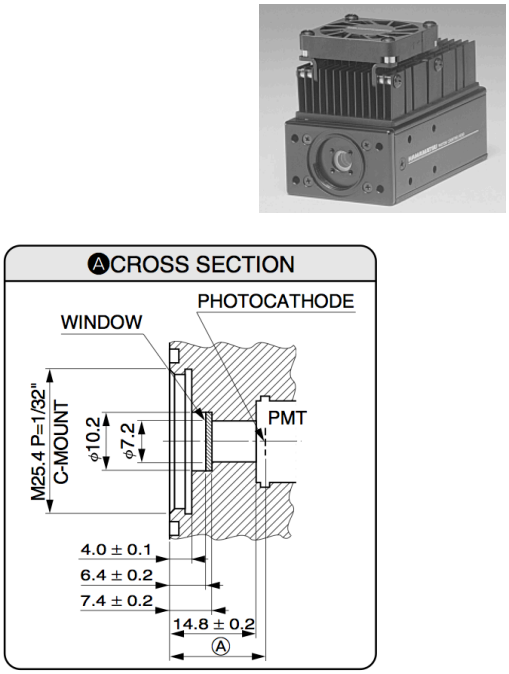

Figure 7: Image of H7422P-40 PMT module cross section.

Figure 7 depicts the arrangement of the apertures and recessed photocathode, which resulted in the reduced acceptance angle. Ideally, the limiting aperture of our collection optics would be defined by the back aperture of the objective, ensuring that all rays coming from the objective are collected. The design of the H7422P-40 PMT module made it impossible to accomplish this. In our first iteration design of the collection optics, the 7.2 mm diameter aperture always defined the limiting aperture, which was 8.9 mm from the photocathode. The equivalent NA of this PMT is ~ 0.37. In order to collect all of the photons coming from the large back aperture of our primary imaging objective, a PMT with a larger acceptance angle was necessary.

For the second iteration design, we special-ordered a pair of Hamamatsu, H10770PB-40 PMTs. This PMT is identical to is the one used in the H7422P-40 assembly, but it does not have the enclosure necessary for the thermoelectric cooler (see

Figure 8). Because there is no secondary enclosure with limiting apertures, the acceptance angle is greatly increased.

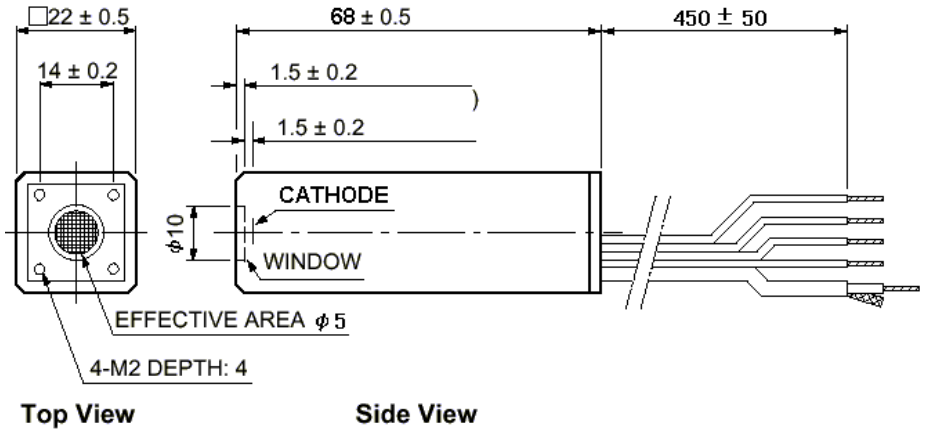

Figure 8: Image of H10770PB-40 PMT.

The H10770PB-40 is the actual detecting subcomponent of the H7422P-40. Therefore the detector performance of the H10770PB-40 PMT is identical to the performance of the H7422P-40, with the exception of the dark current. The increased acceptance angle comes at the expense of dark current, as there is no longer a thermoelectric cooler. The dark current for the H10770PB-40 is 6000 counts per second. Although this rate is 60x greater than the dark current for the H7422P-40 model, given our pixel dwell time of 2 μs, the result is still less than one dark count per second per pixel. Therefore, the design trade-off is favorable for low-light imaging applications such as two-photon microscopy. The H10770PB-40 PMT's aperture is a 10 mm diameter opening, which is 1.5 mm from the photocathode. The effective NA of this PMT is 0.95. With proper optics design, it is possible for the back aperture of the objective to be the limiting aperture of the system when using this PMT.

Two-Inch vs. One-Inch Optics

Setting up the collection optics such that the back aperture of the objective is imaged on the detector is a necessary but not sufficient condition to ensure complete collection of the photons coming out of the back aperture of the objective. To ensure that all the light is collected, the back aperture itself must be the limiting aperture of the system. This is equivalent to saying that the exit pupil, as seen from the detector, must be the back aperture and that the entrance pupil, as seen from the back aperture, must be the detecting surface of the detector. In our first iteration of the collection optics design, the H7422P-40 PMT enclosure contained the limiting aperture. In addition to the PMT, the one-inch diameter optics and opto-mechanics of our first design also provided apertures that limited some of the light from the objective from reaching the detector. Figure 9 is a ray trace of our original one-inch collection optics configuration for our original 8 mm back aperture objective. This analysis showed that if the light coming from our objective had an isotropic angular distribution with a maximum angle of 12 degrees, only 12% would be collected.

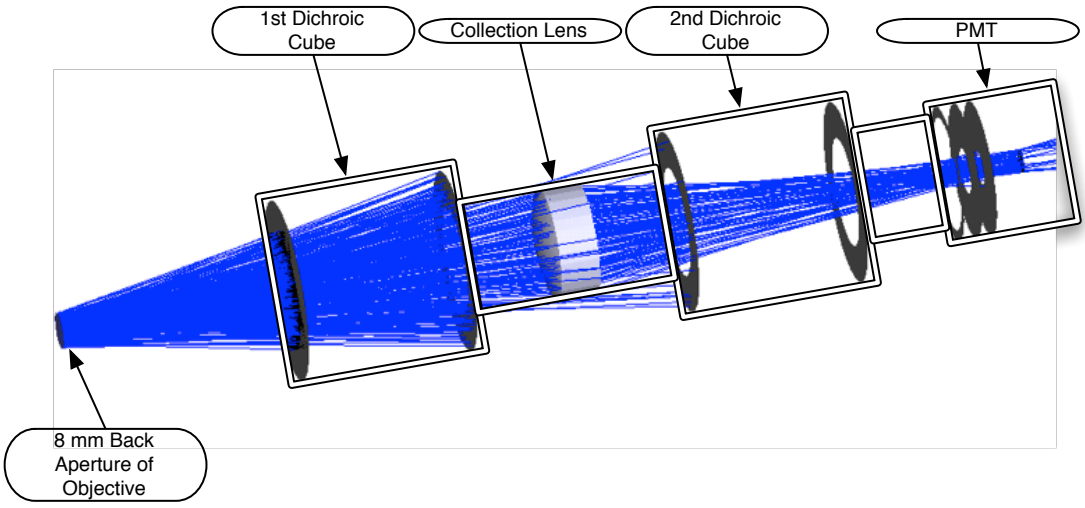

Figure 9: Ray trace diagram of our original 1” collection optics design.

To improve collection efficiency, our collection optics design was changed so as to eliminate all undesirable limiting apertures. Our current design uses two-inch diameter optics, as shown in Figure 10.

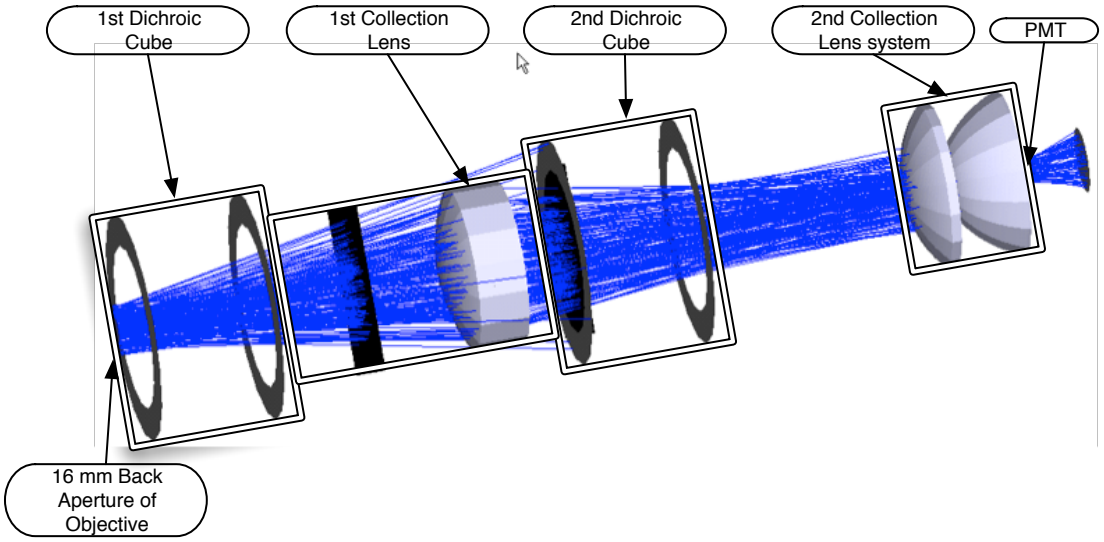

Figure 10: Ray trace diagram of current 2” collection optics design.

Ray trace analysis shows that the current two-inch design collects 95% of the light coming from the 18 mm back aperture of our Olympus 20X objective when we model isotropic angular distribution with a max angle of 12 degrees.

The optics for our new design are laid out as follows. The objective is placed as close as possible to the cube that holds Dichroic #1 (see Figure 5). The spacing between the back aperture of the objective and the front surface of Collection Lens #1 is ~100 mm. Collection Lens #1 is an f = 100mm lens (Thorlabs, AC508-100-A). Collection Lens #2 is actually a lens system consisting of two lenses in contact with each other. The first lens in the system is an f = 50 mm lens (Edmund Optics, NT32-971). The second

lens in the system is an f = 40 mm aspheric lens (Optosigma, 023-2550). The net focal length of the lens system is ~25 mm. The front surface of the first lens in Collection Lens System #2 is 120 mm from the back surface of Collection Lens #1. The PMT is placed 40 mm from the back surface of the second lens of Collection Lens System #2.

To achieve this optics design, we used Thorlabs 60 mm cage components and SM2 lens tubes. Figure 11 depicts the optomechanical setup of our collection optics.

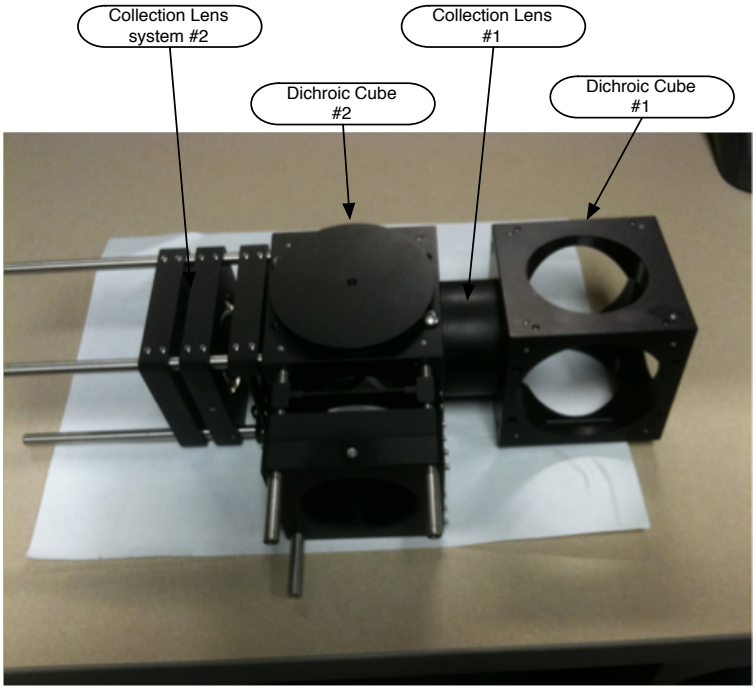

Figure 11: Optomechanics for 2" collection optics design.

Filters and Dichroic Mirrors

Our collection optics employ two dichroic mirrors and two pairs of interference filters. The first dichroic mirror is used to reflect only the fluorescence toward the

detectors and transmit the excitation light. Dichroic #1 is a Chroma 56 mm x 61 mm 740dcxxr. The second dichroic mirror is added so that we can simultaneously detect two fluorophores. It transmits wavelengths above 580 nm toward PMT #2 and reflects wavelengths below 560 nm toward PMT #1. Dichroic #2 is a Chroma 56 mm x 61 mm 570dcxxr.

Directly in front of each PMT are a short-pass filter and a band-pass filter. The band-pass filter ensures that only light from the fluorophore of interest reaches the PMT. Given that dichroic mirrors have poor blocking, this feature is particularly important when imaging multiple fluorophores. The short-pass filter offers additional blocking of the excitation light, which results in improved signal-to-background ratio imaging. The short-pass filter we use in front of PMT#1 is a one-inch Semrock, FF01-680/SP-25 with a cut off of 660 nm, and the short-pass filter in front of PMT#2 is a one-inch Semrock, FF01-750/SP-25 with a cut off of 720 nm. Table 1 lists the band-pass filters we use for imaging and DO measurement.

Pass Band	**Usage**	**Manufacturer**	**Part Number**
700 $\pm$ 35 nm	Porphyrin based PQO measurement	Chroma	ET700/75m-2p
610$\pm$ 35 nm	Rhodamine, Ruthenium based PQO measurement	Chroma	HQ610/75m
510$\pm$ 40 nm	Fluorescein imaging	Chroma	HQ510/80m-2p
400 $\pm$ 30 nm	Second harmonic imaging	Semrock	FF01-417/60

Table 1: Band-Pass filters.

Instrumentation

In addition to the excitation sources, optics and detectors, the two-photon microscope requires the following pieces of instrumentation:

Diagram

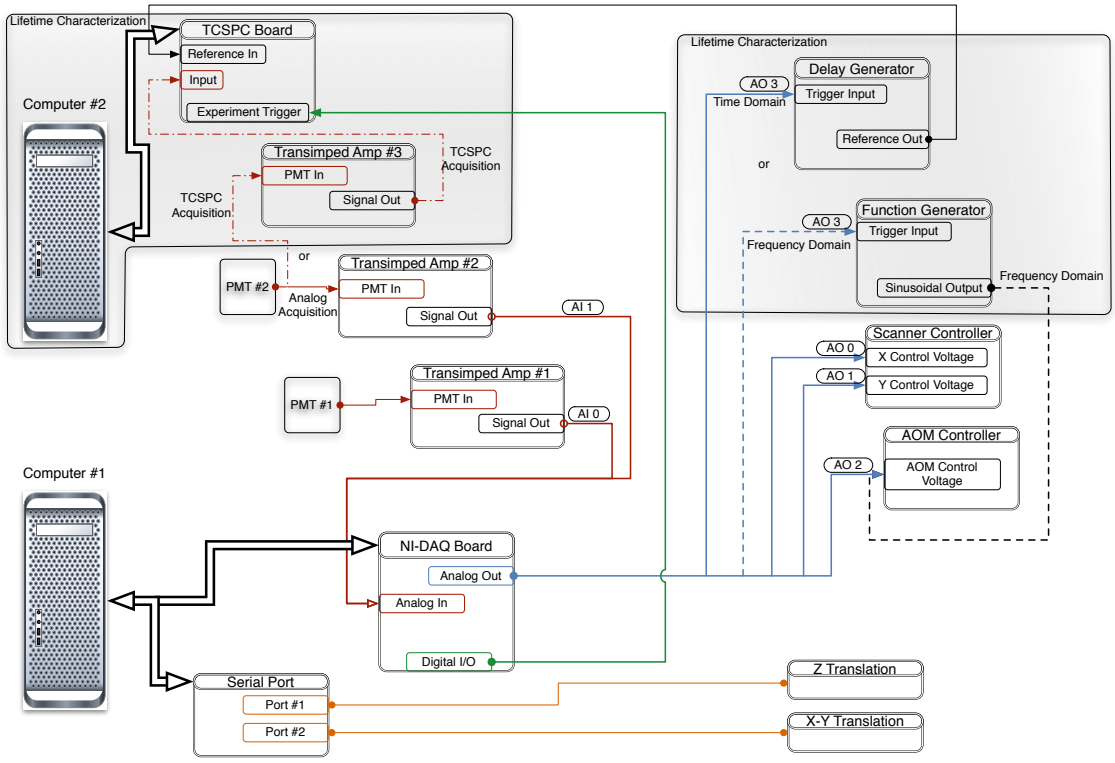

Figure 12: Diagram of the instrumentation of our two-photon microscope setup.

Instrument	Make / Model	Function	Software Module
NI-DAQ Board	NI / PCI-6259	Analog IO, Digital IO	NA
AOM Driver	NEOS/21080-1AM	Modulation of excitation source	Aomcontrol.cpp
Scanner Controller	Cambridge Technology /671215H-1HP	Drives both scanners	Scanengine.cpp
Function Generator	SRS /DS345	Sinusoid generation for frequency-domain measurements	NA
Delay Generator	SRS/DG645	Supplies reference pulse for TCSPC measurement	NA
TCSPC Board	Becker and Hickl / DPC-230	Lifetime acquisition	Vendor Application
Transimpedance amp #1	SRS/SR570	Convert current signal to voltage and amplify (1 MHz bandwidth)	NA
Transimpedance amp #2	SRS/SR570	Convert current signal to voltage and amplify (1 MHz bandwidth)	NA
Transimpedance amp #3	Becker and Hickl/AFAC-26DB	Convert current signal to voltage and amplify (1 GHz bandwidth)	NA
X-Y translation	Velmex/	x-y translation of animal under objective	vxmDriver.cpp
Z translation	Generic	Vertical translation of objective	zStepDriver.cpp

Table 2: Instrumentation

Computer Control

Operation of the microscope is primarily driven by Computer #1 (Figure 12) via a multifunction data-acquisition board (National Instruments, PCI-6259). The multifunction board contains four 16-bit analog outputs with 2 MHz sample rate, thirty-two 16-bit analog inputs with 1 MHz sample rate, and digital input and output

capabilities. The computer also drives some of the instrumentation via the serial port interface. Computer #2 houses the Becker and Hickl DPC-230 board, which is used for lifetime characterization (see below).

Custom software written in C++, using the QT GUI programming toolkit, controls the microscope instrumentation. The software is written with a "model view control" design pattern. Image data is displayed through the National Instruments Vision Library, which also allows us to select regions of interest. DO measurement locations are determined interactively via the point selection tool, which is part of the National Instruments Vision Library. Additionally, each piece of instrumentation under computer control has its own software class. The control portion of the code interfaces with an instance of the corresponding class in order to control that instrument (see Table 2).

Z-Translation System

Z translation in our system is accomplished by moving the objective up and down vertically as the sample remains fixed. Movement is done through the use of a Nikon MDB64010 modular focusing unit. A custom adapter piece attaches the objective and collection optics to the modular focusing unit. In our case, the collection optics are fixed to the objective. Figure 13A illustrates how Dichroic Cube #1 is attached to the modular focusing unit. The objective threads into a dovetailed adapter piece, which slides into a slot directly underneath Dichroic Cube #1.

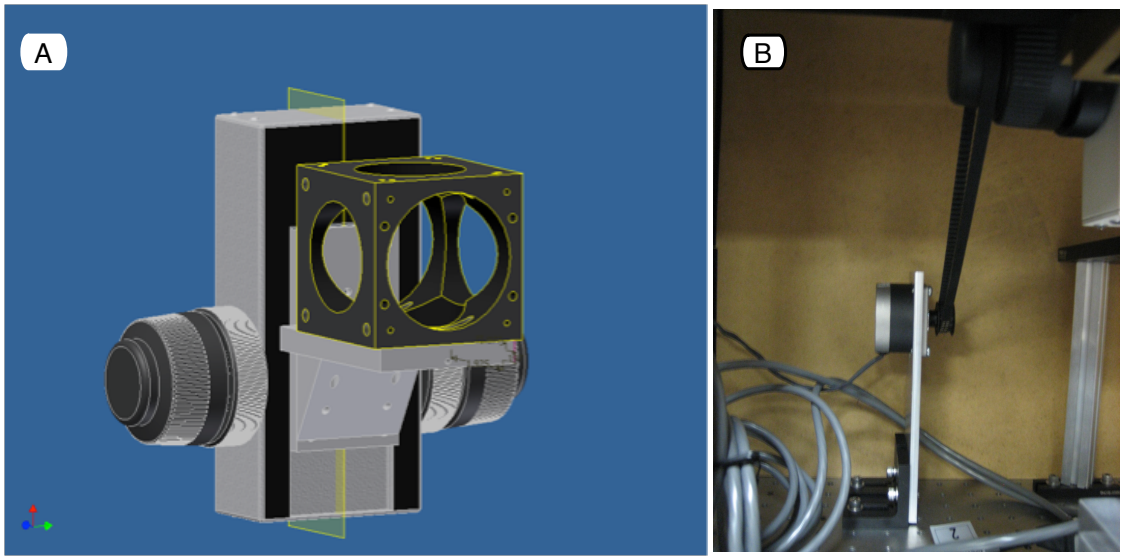

Figure 13: Illustration of modular focusing unit used for z-translation. A. Solid model of translation unit with Dichroic Cube #1. B. Stepper motor and drive belt.

Z-translation is placed under computer control via a stepper motor and belt system, which engages the fine focus knob of the modular focusing unit (Figure 13B). The computer drives the stepper motor controller through a serial port interface.

Animal Positioning System

To properly position the mouse or rat cortex under the microscope objective, we anesthetize the animal and place it in a custom immobilization frame, which is then placed on a motorized x-y translation stage (Velmex, MAXY4009W1-S4). The stage has a range of 127 mm and a resolution of 1 µm. The controller for the translation stage connects to the computer through a serial port interface and can be controlled by our software.

LIFETIME CHARACTERIZATION SYSTEM

Our lifetime characterization system consists of a means of delivering a modulated two-photon excitation source and a system for adequately recording the optical response. As described earlier, one of the goals of this research is to compare porphyrin-based and ruthenium-based molecular oxygen probes. These two approaches occur on time scales that differ by three orders of magnitude. Our instrumentation must therefore be able to accommodate both of these approaches. Furthermore, we are interested in comparing time-domain lifetime and frequency-domain lifetime determination methods. Consequently, our system must be able to deliver pulses of excitation as well as sinusoidally modulated pulse trains from a two-photon excitation source.

Two-Photon Phosphorescence Quenching Oximetry, Excitation Setup

To implement time-domain, porphyrin-based PQO, it is necessary to generate pulses of excitation with an on-time of approximately one-tenth the lifetime and a period of approximately 3 to 5 times the lifetime. Since porphyrin-based probes have lifetimes between tens and hundreds of microseconds, the pulse train from our two-photon excitation source must be appropriately gated so as to meet the on-time and period requirements for PQO. Our system uses the Mira 900 and AOM to accomplish this. Figure 14 illustrates gating of the 76 MHz pulse train from the Mira with the AOM.

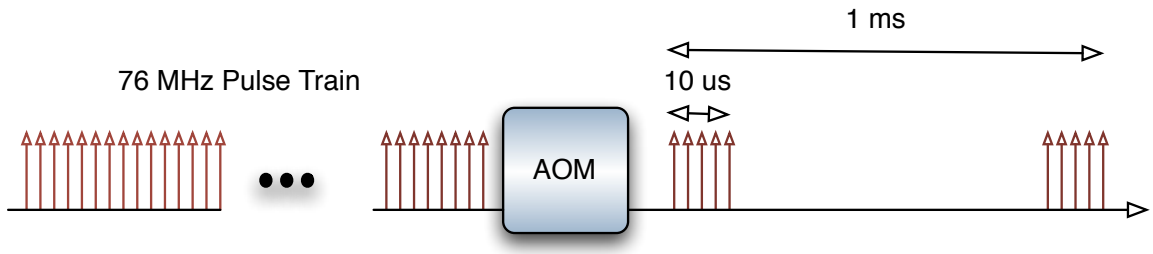

Figure 14: Gating of the 76 MHz pulse train from the Mira 900 for time-domain, porphyrin-based lifetime measurements.

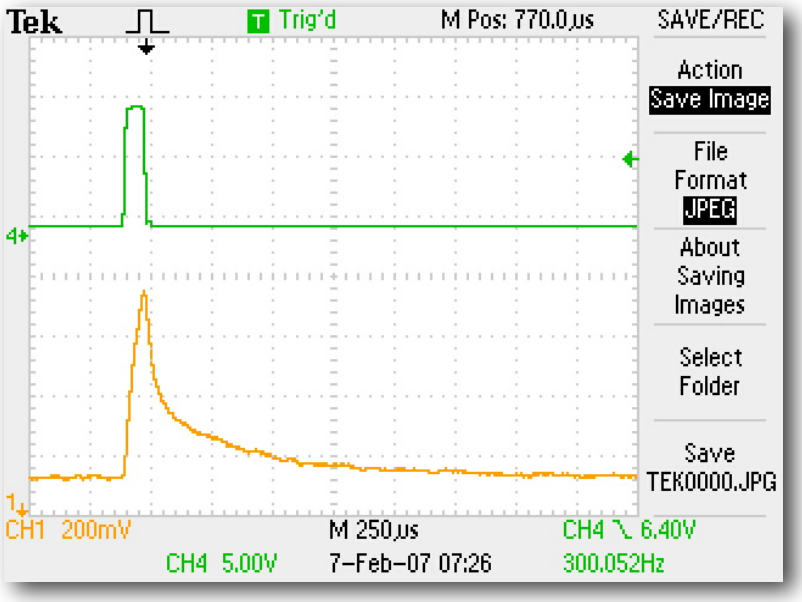

Figure 15: Oscilloscope trace of AOM control signal (top) and Oxyphor R2 decay signal (bottom).

The AOM is controlled by a voltage signal between zero and one volt. At zero volts, the first-order diffracted beam through the AOM is completely extinguished. At one volt, the first-order diffracted beam is maximally transmitted. The software generates the control voltage and synchronizes the gating with acquisition of the

phosphorescence decay signal. Figure 15 demonstrates the AOM control voltage and corresponding phosphorescence signal.

For frequency-domain, porphyrin-based lifetime measurement, a sinusoidal control voltage is sent to the AOM. The pulse train from the Mira 900 is then sinusoidally modulated. The modulation frequency is nominally $\sim f \approx 1/2\pi\tau$, where tau is the lifetime.

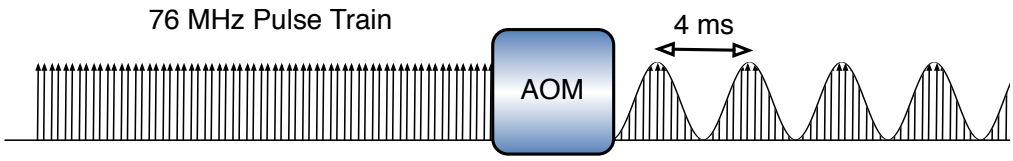

Figure 16: Modulation of 76 MHz pulse train from the Mira 900 for frequency-domain, porphyrin-based lifetime measurements.

We use a Stanford Research Systems, DS345 function generator to supply the AOM control voltage signal. Because of the non-linearity of the AOM response, the sinusoid amplitude and offset parameters of the function generator had to be adjusted so as to result in a single, pure sinusoid after the AOM. To accomplish this, a photodiode was used to monitor the optical signal from the AOM. A fast Fourier transform (FFT) was taken, and the amplitude and offset were adjusted until all harmonics were < 50 dB of the fundamental. The function generator is triggered by a synchronization signal that our software generates. The trigger output signal from the function generator is then used to synchronize the acquisition of the phosphorescence signal.

For time-domain ruthenium-based PQO measurements, we use the RegA 9800 excitation source. The expected lifetime of ruthenium ranges from ~ 100 ns to 700 ns. As desired, the repetition period of this laser (4 μs) is approximately 5 times the expected

lifetime; therefore, no AOM gating is required. Although the pulse width of 150 fs is dramatically smaller than the desired one-tenth lifetime, its high pulse energy allows for sufficient excitation of the ruthenium-based probe molecule to provide ample signal.

Frequency-domain ruthenium-based lifetime measurements are generated using the same instrumentation as frequency-domain porphyrin-based measurements. The only difference is that the modulation frequencies are three orders of magnitude higher (100 – 800 kHz).

Two-Photon Phosphorescence Quenching Oximetry, Acquisition Setup

Once the phosphorescent molecular probe has been excited, the optical response must be acquired and saved. The stored data must then be analyzed, and a lifetime value must be determined from the fitting routines along with the appropriate mathematical model. The time scales involved for porphyrin-based lifetime measurements are slow enough that it is feasible to apply our standard acquisition instrumentation used for imaging. In this scenario, the software stores the phosphorescence signal as a separate file on the computer for post-processing. Since the computer controls the synchronization of the AOM modulation, no additional signals are needed to synchronize the acquisition with the modulation.

For ruthenium-based measurements, which occur on a time scale three orders of magnitude faster than porphyrin-based measurements, the standard imaging acquisition instrumentation is not fast enough to adequately characterize the optical response. Therefore, acquisition for all ruthenium-based measurements is done using a Becker and Hickl, DPC-230 photon correlator board. This board, which operates as a time-correlated photon-counting board (TCSPC), is specifically designed to make fluorescence lifetime

and fluorescence correlation measurements. The DPC-230 has a maximum temporal resolution of 160 ps and can make measurements that span 10 orders of magnitude (up to 3.5 ms) in time. To achieve these long time scales, the board operates in a variant of the traditional TCSPC mode called multichannel scaler mode (See manual for complete description). This feature allows the data rates to be manageable over longer time-period measurements. Because of the unique capability of the board to make very high temporal resolutions over such a wide temporal window, the board can be used for ruthenium-based measurements and porphyrin-based measurements. In Chapter 5, I compare the standard analog acquisition method to acquisition using the DPC-230 for porphyrin-based measurements.

Chapter 3: Preliminary Results

INTRODUCTION

The following text in this chapter is taken directly from the manuscript of a journal article we published which describes our preliminary efforts and results combining TPM with PQO. The article titled "Microvascular Oxygen Quantification Using Two-Photon Microscopy", was published in Optics Letters, Volume 33(10), 2008.

ABSTRACT:

An instrument is demonstrated which is capable of three-dimensional vasculature imaging and PO_2 quantification with high spatial resolution. The instrument combines two-photon microscopy with phosphorescence quenching to measure PO_2. The instrument was demonstrated by performing depth-resolved microvascular PO_2 measurements of rat cortical vessels down to 120 μm below the surface. Two-photon excitation of porphyrin was confirmed and measured PO_2 values were consistent with previously published data for normoxic and hyperoxic conditions. The ability to perform three-dimensional PO_2 measurements using optical techniques will allow researchers to overcome existing limitations imposed by polarographic electrodes, magnetic resonance techniques and surface-only PO_2 measurement techniques.

MICROVASCULAR OXYGEN QUANTIFICATION USING TWO-PHOTON MICROSCOPY

Because oxygen is vital to the metabolic processes of all eukaryotic cells, a detailed understanding of its transport and consumption is of great interest to researchers. Problem domains that exemplify this interest include basic physiology, cortical spreading

depression, stroke and tumor angiogenesis to name a few. Current methods for in vivo measurement of intravascular and tissue dissolved oxygen concentration (PO_2) at the cellular level are non-ideal. Either they lack the three-dimensional spatial resolution desired, are invasive and disturb the local physiology, or they rely on hemoglobin spectrophotometry, which is not a direct measure of the oxygen available to cells. It has been suggested that combining two-photon excitation with the PO_2 quantification via phosphorescence quenching [27, 28] could lead to a new method that is well suited for high resolution PO_2 measurement in vitro and in vivo [48].

The phosphorescence quenching technique relies on changes in the phosphorescence lifetime of a molecular probe (most commonly palladium-porphyrin) as it is quenched by oxygen. PO_2 quantification based on this principle has been shown to be an effective and accurate method for measuring dissolved oxygen concentration both in tissue and in vasculature [31, 49-51]. The relationship between lifetime and PO_2 is described by the Stern-Volmer equation: $1/\tau = 1/\tau_0 + k_q \, pO_2$, where τ is the measured phosphorescence lifetime, τ_0 is the lifetime of the phosphor under zero-oxygen conditions and k_q is the quenching constant. Porphyrin-based oxygen probes are typically used for this type of application because porphyrin is known to be exclusively quenched by oxygen and its use in vivo has been well established in the literature [27, 28, 31, 39, 50-52]. These types of probes have long lifetimes (~100s of μs) and quenching constant values that make them well suited for measurement of physiological oxygen concentrations.

Combining two-photon microscopy with oxygen determination via phosphorescence quenching would in principle have micron-scale resolution, have inherent three-dimensional sectioning and provide absolute PO_2 values. Because oxygen diffusion is a three-dimensional phenomenon, an instrument capable of three-dimensional

measurements is needed to fully characterize oxygen delivery to cells. Although Mik et al. [39] demonstrated the proof of concept by measuring in vivo tissue oxygen concentration along the axial direction using a two-photon excited phosphorescence lifetime technique, to date there have been no reports in the scientific literature of combining two-photon imaging with PO_2 sensing using phosphorescence quenching in vivo. This is most probably due to the low two-photon action cross-section of porphyrin [48] and the timing mismatch between the repetition rate of common two-photon excitation sources (ns) and the porphyrin lifetime (μs).

In this Letter, we describe an instrument that combines two-photon microscopy with PO_2 quantification using two-photon excited phosphorescence lifetime quenching. The instrument is capable of simultaneously imaging vascular morphology and measuring three-dimensional PO_2 gradients. Although we only demonstrate intravascular PO_2 measurements here, other groups have reported tissue PO_2 determination using a one-photon phosphorescence lifetime quenching technique [50]. Provided the two-photon excitation source can produce similar levels of excitation, the instrument we describe should similarly be able to measure tissue PO_2. Additionally, with appropriate fluorescence labeling the potential exists to simultaneously image cells. This approach therefore has the capability of providing a complete three-dimensional picture of PO_2 dynamics from delivery by the vasculature to consumption by the cells using only optical methods. In this paper we demonstrate the simultaneous three-dimensional imaging of microvasculature and image guided measurement of intravascular PO_2 in rat cortex.

Instrumentation Description

The instrument is capable of three-dimensional, image guided PO_2 measurements because of the simple introduction of an accusto-optic modulator (AOM) to a standard two-photon fluorescence microscope setup to serve as a temporal gate to the laser pulse train (Figure 17).

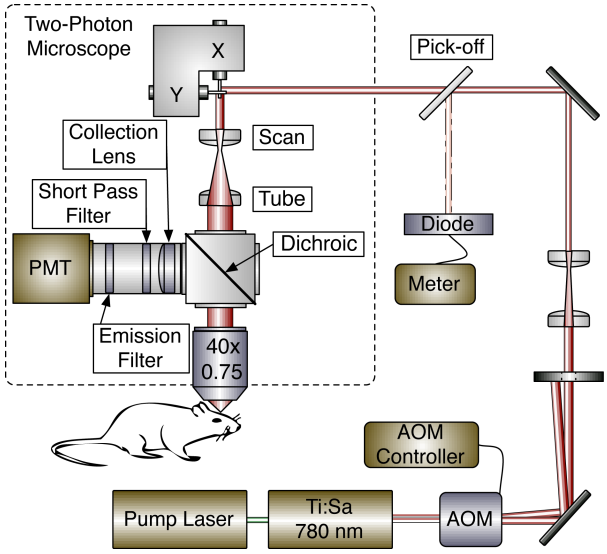

Figure 17: Experimental setup for TPM and porphyrin-based PO_2 measurement

The AOM (NEOS Technologies 23080-2-LTD) is needed to overcome the timing mismatch between the phosphorescence lifetime of porphyrin in vivo (50-200 μs) and the time between pulses from our two-photon excitation source (~13 ns). Light (λ = 780 nm) from a Ti:Sapphire oscillator (Coherent Mira 900, 10W pump) is passed through the AOM under computer control. The first order diffracted beam is directed to beam conditioning optics, to galvanometer scanning mirrors (Cambridge Technology, 6125HB) and finally to an objective (40x 0.7 NA water immersion). In imaging mode, a continuous voltage is applied to the AOM, and the pulse train from our excitation source is completely transmitted to the microscope. However, in PO_2 measurement mode, the

AOM is made to gate the pulse train by providing a control voltage signal with a duty cycle of 1% and a repetition rate of 1 kHz. For PO_2 measurement, pulses are therefore allowed to reach the sample for 10 μs out of every 1ms. Fluorescence and phosphorescence signals are detected by a PMT (H7422P-50, Hamamtsu Corp.). Acquisition of phosphorescence decays was synchronized with gating of the AOM, enabling multiple excitation events to be averaged quickly to improve the signal to noise ratio as needed.

Methods

To demonstrate the capabilities of this new instrument, we simultaneously mapped a region of vasculature and performed microvasculature PO_2 measurements of rat somatosensory cortex while the fraction of inspired oxygen (FiO_2) was varied. Sprague-dawley rats were anesthetized for surgery with urethane (1.5 g/kg, 0.3 g/kg supplements as needed) by intraperitoneal injection, and an intravenous line was inserted into the femoral vein. The skull and dura were removed over a 3x3 mm area. A well was created around the exposed area, filled with agarose, then sealed with a coverslip which was secured to the stereotaxic frame with a metal coverslip holder as described elsewhere [53]. Dextran-conjugated fluorescein was injected intravenously at a concentration of 83 mg/kg for visualization of cortical vasculature. A solution of 28 mg/ml Oxyphor R2 (Oxygen Enterprises) and 20 mg/ml of BSA (BP671-10 Fisher Scientific) dissolved in physiologic saline was created, and 3 ml/kg of this solution was then injected intravenously. Sequences of vasculature images were recorded from the fluorescein emission at different depths. From these images multiple points within individual vessels were interactively selected for PO_2 measurements using our software. The selected

points were translated to galvanometer positions and 2000 phosphorescence decay curves were recorded at each location and averaged together. Because of a transimpedance amplifier with limited bandwidth and an AOM driver with a slow turn off time, the first 50 μs of data was discarded so as to ignore any artifacts from scattered excitation light. A single exponential decay model was fit to the average phosphorescence decay curve at each location to determine the phosphorescence lifetime. Using published values for the porphyrin quenching constant and unquenched lifetime [54], the lifetimes were converted to PO_2 values using the Stern-Volmer relationship. PO_2 measurements were taken at various depths. At each depth location the FiO_2 was varied and PO_2 data were acquired.

In *in vitro* experiments we verified that the presence of fluorescein had no effect on the porphyrin lifetime at the concentrations used *in vivo*. The phosphorescence lifetime was then measured in the absence of oxygen and was found to be unchanged and to approximately match reported values (~500 μs) [54]. *In vitro* experiments also confirmed two-photon excitation of porphyrin by observing that the phosphorescence intensity varied as the square of the excitation intensity (Figure 19B).

Results and Discussion

Figure 18 shows typical results for cortical vessels under normoxic and hyperoxic conditions at depths of 120 and 100 μm. The figure depicts vasculature images at two locations with PO_2 measurement overlays for the two FiO_2 conditions.

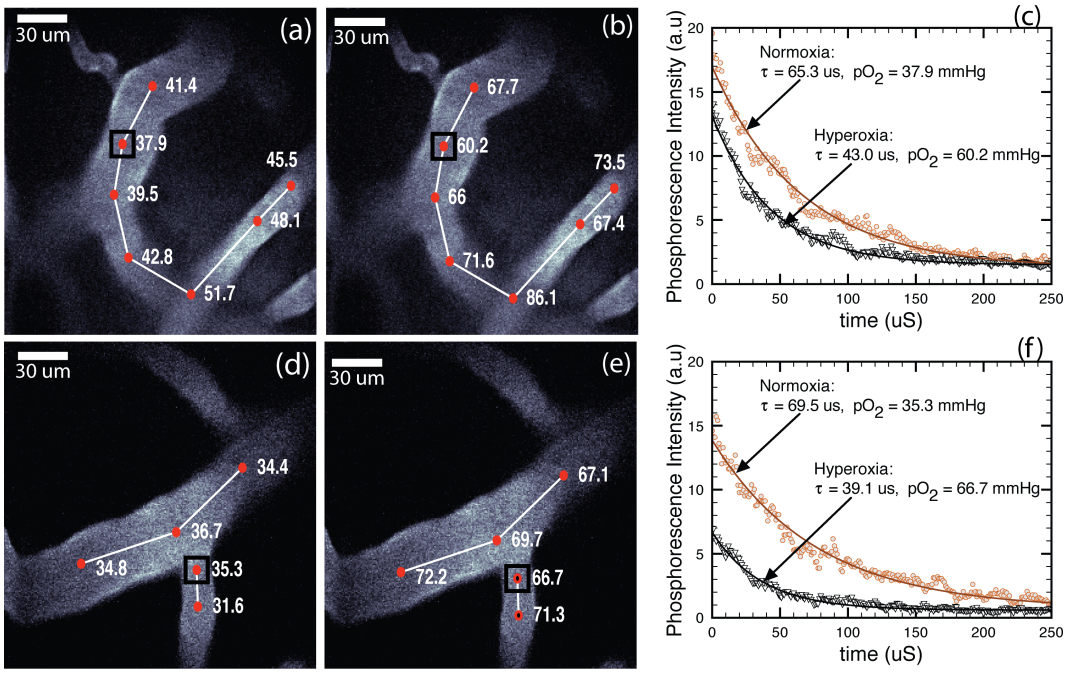

Figure 18: Image of arteriole network 120 µm below the surface under normoxia (a), and hyperoxia (b). The phosphorescence decay data with best fit curves for the highlighted point in panels (a) and (b) is depicted in (c). Image of arteriole network 100 µm below the surface under normoxia (d) and hyperoxia (e). The phosphorescence decay data with best fit curves for the highlighted point in panels (d) and (e) is depicted in (f). pO_2 values in units of mmHg.

Vasculature imaging was done using a power of ~ 3 mW , and PO_2 measurements were taken with an average power of ~ 1.5 – 2 mW after the 1% duty cycling. Our combination of objective and laser wavelength resulted in an excitation focal volume of 0.5 µm (radial) by 1.3 µm (axial) in size. For intravascular PO_2 measurements, the focal volume moves downstream with the blood flow as it phosphoresces. Therefore, the spatial resolution of the PO_2 measurement is a function of the local flow rate and the lifetime of the probe at that location. For our experiments, we estimate the resolution to be ~ 10 µm or better. The measured PO_2 values are in good agreement with values reported in the literature for arterioles under similar conditions. For instance, Shonat [55]

reports that for rat cortical arterioles of similar size, using similar anesthesia, arterioles had a PO_2 of ~40 mmHg in the normoxia case and ~60 mmHg in the hyperoxia (60% FiO_2) case.

Figures 18C and 18F show the nature of the fitting of the averaged phosphorescence signals for the highlighted points within each image. The highlighted PO_2 measurements in Figs. 2a and 2b had a standard error of $\pm$1.7 mmHg and $\pm$3.5 mmHg respectively, whereas the standard error of the PO_2 measurements highlighted in Figs. 2d and 2e were $\pm$1.3 mmHg and $\pm$1.6 mmHg respectively. The standard error can be improved as needed by simply averaging more phosphorescence decay events, at the expense of temporal resolution. We found that ~2000 decays was sufficient to produce an error of < 2 mmHg for the majority of our in vivo measurements down to a depth of approximately 300 μm across 10 rats. For greater depths, more averaging is needed because of the signal to noise ratio decrease caused by the loss of excitation intensity at the focal volume. The poor signal to noise ratio which results from the low two-photon cross-section can also be mitigated to some extent by increased porphyrin concentration. We confirmed that for a given intravascular PO_2, the measured decay lifetime did not vary with the concentration of porphyrin in the blood over a range from 130 μM to 430 μM. Although these concentrations are relatively high compared to the conditions used to determine the reported [54] quenching constant and unquenched lifetime, these values do not seem to vary strongly with concentration. We estimate that we have a systematic error in our PO_2 calculation no greater than 10% as a result. To more accurately calculate PO_2 from the measured decay lifetime, one would need to perform a calibration of these parameters under similar high concentration conditions. As oxygen probes with higher two-photon action cross sections become available, signal to noise should improve. This

will result in lower concentrations required, lower average excitation power required and improved temporal resolution.

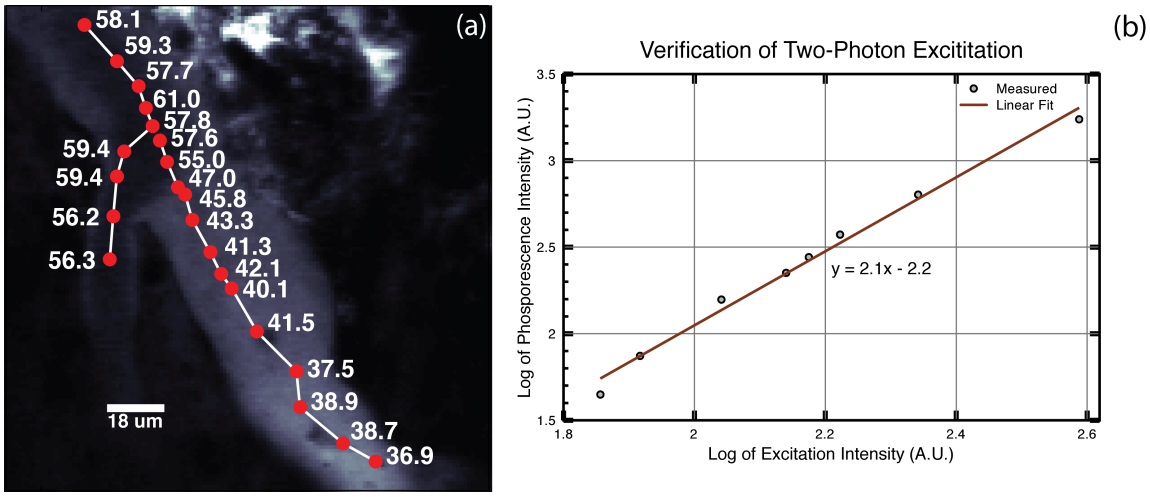

Figure 19: (A) Image of branching cortical vessel 60 µm below the surface. A clear pO_2 gradient is visible due to an occlusion in the lower branch of the vessel. pO_2 values in units of mmHg. (B) Verification of two-photon excitation of porphyrin.

Figure 19 further demonstrates the unique capabilities of the instrument. The image shows a branching vessel 58 µm below the surface where one branch contains a highly localized occlusion. The vasculature image was created by averaging 10 consecutive frames. Red blood cell motion in the unoccluded branch shows up as an area of lower intensity since only the blood plasma is labeled with dextran-conjugated fluorescein. The PO_2 measurements indicate that oxygen is still able to reach the lower branch that is devoid of erythrocytes. However, the PO_2 values in that section are reduced and show a decreasing gradient as we move away from the unoccluded branch.

Conclusion

The instrument described in this Letter is distinct from other PO_2 sensing techniques in that it has the ability to provide image-guided, depth resolved PO_2 measurements at high resolution. Since only a simple modification to a standard two-photon microscope setup is required, three-dimensional PO_2 sensing capability can be easily incorporated into many existing two-photon imaging setups.

This work was funded by grants from the National Institutes of Health (NS050150), American Heart Association (0735136N) and National Science Foundation (CBET/0737731).

Chapter 4: Interfering Luminescence from Microscope Objective

INTRODUCTION

In the previous chapter, we presented our preliminary results developing a three-dimensional, high-resolution method of measuring PO_2. After publishing our early work, we realized that our PO_2 measurements occasionally did not agree with our experimental manipulations. For example, on occasion, we would observe that changing the fraction of inspired oxygen, such that the oxygen saturation was significantly changed, failed to produce the appropriate change in our PO_2 measurements. Investigating the source of this inconsistency revealed that light, which was similar to the optical signal produced by our porphyrin PQO probe, was being generated by interaction of our excitation light with the glass in our optics. Furthermore, this generated light was always present and always interfered with our measurements. Under the conditions needed to excite our PQO probe, large amounts of luminescence from the optics were produced, such that the signal-to-background ratio of our phosphorescence signal could be as low as two. To the best of our knowledge, the existence of this type of luminescence has gone largely unreported. We believe that the reason it has gone unreported is that few research groups are engaged in long lifetime measurements (in the μs range), at emission wavelengths near 700 nm, using an excitation source tuned to a wavelength of ~800 nm. Even though interfering luminescence is most easily observed when performing lifetime measurements, it is also noticeable when performing two-photon imaging of fluorophores that emit near 700 nm when the excitation source is tuned to ~800nm. This is routinely done when imaging gold nanoparticles [56, 57]. Under these conditions, the interfering luminescence would appear as an increased background signal and would therefore degrade image contrast. This is particularly true at greater depths where the excitation power is increased.

Ultimately, interfering luminescence may be what limits imaging depth under these imaging conditions. It is unlikely that the source of the increased background would ever be attributed to luminescence originating from the optics in the microscope.

Although fluorescence from objectives has been reported, the phenomenon we have observed is clearly not fluorescence. Very little in these reports matches the properties of the light we have observed. In this chapter, we present the findings of our experiments to characterize this luminescence. Furthermore, we hypothesize about the mechanism of its production and discuss the consequences for reliable two-photon PQO given the existence of this interfering light.

INTERFERING LUMINESCENCE CHARACTERIZATION EXPERIMENTS

Our microscope could detect an optical signal that was very similar in spectral content and temporal profile to Oxyphor R2 phosphorescence, even when no sample was placed under the microscope objective. We detected and recorded this interfering luminescence via the same procedure we use to detect phosphorescence from our PQO probe during lifetime measurements. Specifically, the same excitation, AOM gating of the pulse-train from the source, band-pass filter, and detector used during PQO measurements were employed to investigate the interfering luminescence. The excitation source was tuned to 800 nm for all of the following experiments unless stated otherwise. For some experiments, the output of our detector was directed to an analog input channel of our multi-function DAQ board (National Instruments, PCI-6259) for recording the signal. In contrast, for other experiments, the output of the detector was routed to the photon correlator board (Becker and Hickl, DPC-230).

Localization of Source

We localized the primary site of unwanted light generation during our PQO measurements to the microscope objective. This finding was confirmed by observing that the luminescence signal disappeared when we removed the objective from the microscope. To confirm that the disappearance of the luminescence signal was not simply due to reduced scattering of the excitation light toward the detector, a large mirror was placed where the objective would have been. The mirror directed excitation light back towards the detector. Increased scattered light could be detected for the time period when the AOM was on. However, no luminescence signal was detected after the AOM was switched off (Figure 20), as was the case when the microscope objective was in place. With the microscope objective in place, a decaying luminescence signal could be detected for tens to hundreds of microseconds after the AOM had extinguished the excitation source (Figure 21).

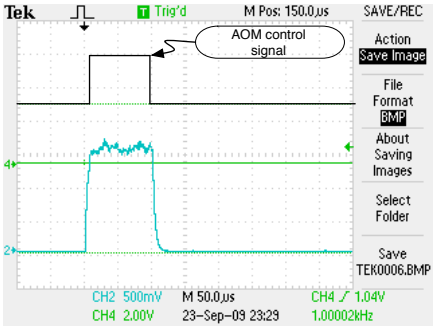

Figure 20: Oscilloscope trace of detector signal with no microscope objective in excitation beam path.

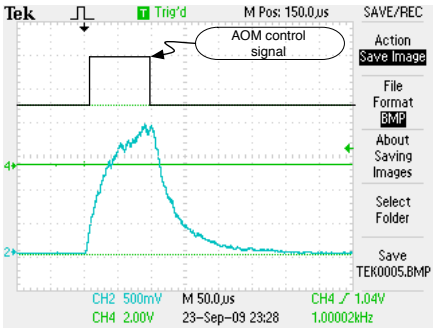

Figure 21: Oscilloscope trace of detector signal with microscope objective in excitation beam path.

We tested various materials by placing them in the excitation beam path where the objective would have been. We found that all common optical glass we tested exhibited this luminescence. The microscope objective is most likely the primary contributor of interfering luminescence because it is the component in the excitation path that contains the largest amount of glass. Additionally, the collection optics are designed to capture as much of the light from the objective's back aperture as possible. All makes of microscope objectives tested exhibited this luminescence. However, so-called low fluorescence objectives were not tested. Plastic materials did not exhibit the luminescence.

Temporal Profile

We tested how the AOM's on-time affected the temporal profile and magnitude of the interfering luminescence. Measurements were made in the same manner as PQO measurements with the exception that an extra blocking filter was used at the detector for increased blocking of scattered excitation light. The microscope objective was in place. However, no sample was placed under the objective, and the beam remained parked in its

center position. A photon correlator board recorded the luminescence signal from the detector. Photons were integrated on the board for a period of 60 seconds.

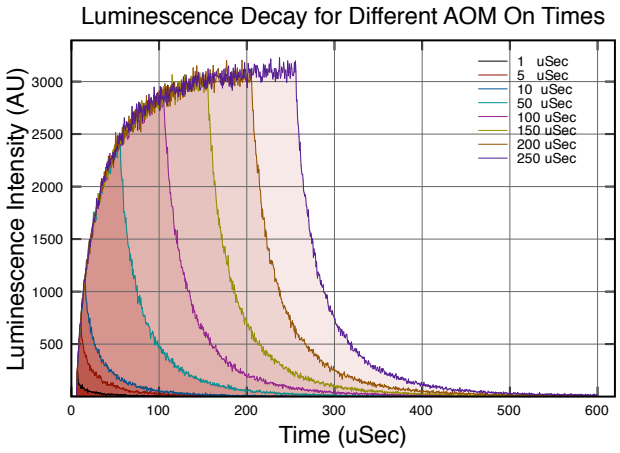

Figure 22: Luminescence decay for different AOM on-times.

The data show that the decay time of the interfering luminescence from the objective did not change as we varied the AOM on-time (Figure 22). The rising portion of the luminescence signal corresponds to the time period when the AOM was on. We fit this portion of signal to a $y(t) = a(1 - e^{-t/\tau})$ model and found that the characteristic time was ~ 30 µsec. The decaying portion of the signal corresponds to the time period when the AOM was off and was fit to a $y(t) = a(e^{-t/\tau}) + b$ model. The characteristic decay time was ~ 40 µsec. The data also show that the magnitude increased as the AOM on-time was increased. In fact, the interfering luminescence appeared to behave like a capacitor that charges up when the AOM is on and discharges when the AOM is off.

Spectral Profile

To test the spectral content of the interfering luminescence, we placed an optical fiber connected to a spectrometer (Ocean Optics, USB 4000) where the phosphorescence detector would normally be in our microscope.

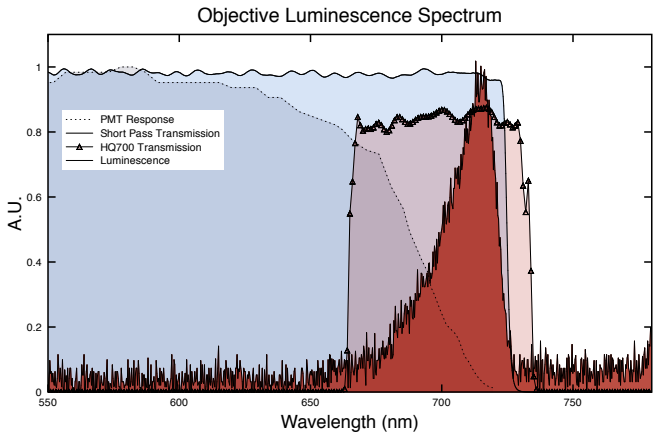

Figure 23: Luminescence spectrum of microscope objective.

The data indicates that the emission spectrum of the interfering luminescence overlaps, at least partly, with the spectrum of our porphyrin PQO probes and is in the pass band of our PQO filter (Figure 23). Although it appears that the luminescence spectrum cuts off abruptly around 720 nm, this cut-off is actually caused by the reflection cut-off of the primary dichroic. The complete emission spectrum most likely continues past 720 nm.

Intensity vs. Temperature

To explain the mechanism of the interfering luminescence, we first hypothesized that, due to absorption of the excitation light, the glass might become rapidly heated

while the AOM was on. When the AOM was turned off, the glass then rapidly cooled. The transient heating may have lead to increased black body radiation in the spectral range of our filters. Subsequent tests using infrared sensitive cameras disproved this theory: the temperature of the glass increased by only a few degrees Celsius even when the AOM was held on constantly and the laser power was turned up beyond levels we use in our PQO measurements. However, other experiments, which looked at the link between temperature and luminescence intensity, provided evidence that the mechanism of the interfering luminescence is at least thermally mediated.

To test the dependence of the luminescence intensity on the glass's temperature, we chose not to use the microscope objective as the source of the interfering luminescence. In its place, we used a much less expensive two-inch double convex lens (Thorlabs, LB1723) that also produced an appreciable amount of luminescence. The lens was placed in a styrofoam container filled with liquid nitrogen and positioned in the beam's path, near where the objective would have been. We recorded the luminescence signal as the lens cooled from room temperature. The signal was recorded in the usual way using the PQO emission filter, detector, and photon correlator board.

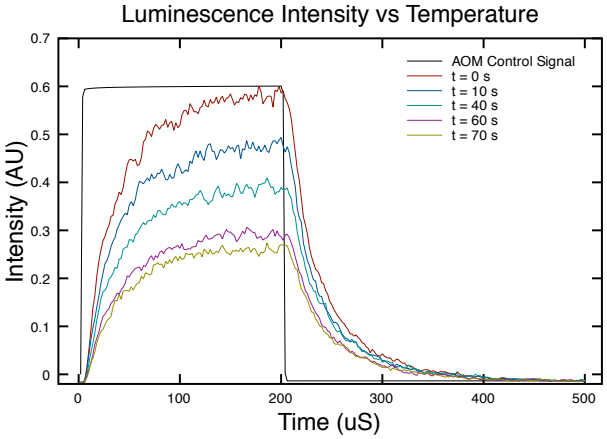

Figure 24: Luminescence intensity from glass after cooling with liquid nitrogen.

The data indicate that cooling the glass partly suppresses the luminescence-generating mechanism (Figure 24). We can conclude from this data that the mechanism behind the interfering luminescence is at least thermally mediated.

Intensity vs. Excitation Power

Given that the excitation source was tuned to 800 nm and the spectrum of the interfering luminescence is at least partially anti-stokes shifted, conservation of energy requires that more than one excitation photon be absorbed for every luminescence photon generated. To test if the mechanism behind the luminescence relied on simultaneous multiphoton absorption, we looked at dependence on the luminescence intensity as a function of the excitation intensity. If a multiphoton absorption process were occurring, we would expect to see a dependence that was a higher order than linear, such as quadratic or cubic.

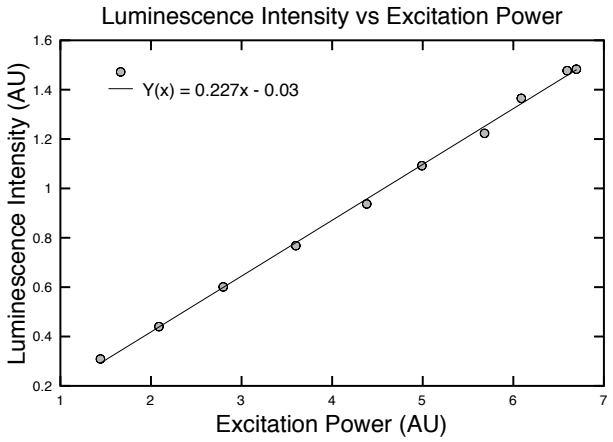

Figure 25: Dependence of luminescence intensity on excitation power.

The data do not show a significant nonlinear dependence, which implies that more than one photon is not absorbed simultaneously for every luminescence photon (Figure 25). However, since energy must be conserved, we can assume that some form of sequential absorption process is occurring. A sequential absorption process does not necessarily have a quadratic or cubic dependence on the excitation power: the probability of excitation to the energy state necessary to produce the anti-stokes shifted photon is not the product of the independent probabilities of absorbing two or three photons simultaneously. Instead, it is the conditional probability of absorbing a photon, given the fact that a previous photon has been absorbed. We further confirmed that simultaneous absorption of multiple photons was not involved in generating the interfering luminescence by running our excitation source in continuous-wave mode. The production of the interfering luminescence was identical regardless of whether the excitation source was operating in mode-locked or continuous-wave modes.

Intensity vs. Excitation Wavelength

We tested whether or not the intensity of the interfering luminescence would vary as we changed the excitation wavelength. We used the same setup described in all of our previous characterization experiments. The only difference was that we operated the AOM in continuous mode and connected the output of the detector to the analog input of our multifunction DAQ board. Since we were not interested in the decay profile, we simply sampled the DC output level from the PMT to determine the luminescence intensity level. As we varied the excitation wavelength, we made sure to adjust the laser intensity such that the number of photons per second remained the same for all

wavelengths. To do this, we simply scaled the power up as we increased the wavelength by the ratio of the current wavelength to the first wavelength.

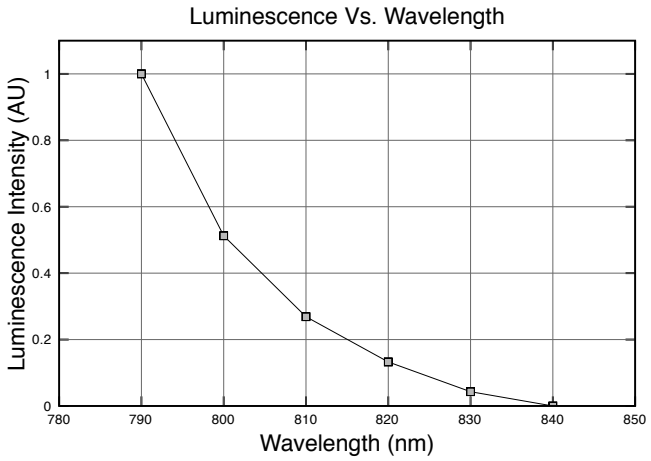

Figure 26: Luminescence intensity vs. wavelength.

The data show that the interfering luminescence decreases dramatically as we increase the excitation wavelength (Figure 26). This is likely due to the fact that, at longer wavelengths, the photon energy is not high enough to excite the glass material to one of the energy states involved in the sequential absorption process.

HYPOTHESIZED MECHANISM

Our current hypothesis about the mechanism behind the interfering luminescence is that our excitation source is inadvertently exciting metal dopant ions in the optical glass material and that these ions subsequently return to their ground states via radiative decay. Specifically, rare-earth metals, such as lanthanum, are often added to the composition of optical glass because their large atomic numbers and small atomic size

result in glass with relatively high indices of refraction. This is advantageous because optical elements can be made thinner, thus reducing spherical aberration properties. Although the exact glass composition in our objectives is proprietary and therefore unknown to us, Lanthanide-based flint and crown glasses are commonly used in optics.

Luminescence from rare-earth metals is very similar to luminescence from the transition metals platinum, palladium and ruthenium, which are at the core of the PQO probe molecules that we have tested. Like transition metals, rare-earth metal luminescence occurs via a quantum-mechanically unfavorable transition between triplet and singlet energy states [58-60]. Consequently, both types of luminescence can be classified as phosphorescence and have long lifetimes that range from microseconds to milliseconds. Additionally, rare-earth metals added to solid-state materials, such as glass or other crystalline structures, usually exist in a bivalent or trivalent state in the host material [60, 61]. The same is true for the transition metals in the PQO probe molecules tested, except that the "host material" in this case is an aromatic hydrocarbon molecule [59]. It is not uncommon for rare-earth metal luminescence to have an emission spectrum that extends into the near infrared, as was observed in our experiments. It is practically difficult to determine which rare-earth luminescent center might be involved based on the known emission lines from rare-earth metals, as interaction with the host material broadens and shifts the emission lines in unpredictable ways [60]. However, near-infrared emission from bivalent and trivalent rare-earth metals in solid-state host materials has been reported [60]. Given the similar natures of rare-earth metal luminescence and the luminescence from the transition metals in our PQO probes, it is not surprising that the interfering luminescence has temporal and spectral properties similar to the phosphorescence signal we measure when making oxygen measurements.

This similarity makes the problem of discriminating our PQO signal from the background of interfering luminescence a technical challenge.

As suggested in the "intensity vs excitation power" subsection of this chapter, the mechanism by which the luminescent centers are excited must involve absorption of two or more photons since the luminescence spectrum shows an anti-stokes shift in relation to the excitation wavelength. Since the efficiency of luminescence generation does not depend on whether the excitation source is mode-locked or continuous, it is safe to assume that the two-photon absorption involving a virtual energy state and simultaneous absorption of two-photons is not occurring. This assumption is further confirmed by the approximately linear dependence of the luminescence intensity on the excitation power. Multiphoton absorption that involves real energy states is typically called *upconversion*. This term refers to the conversion of lower-energy excitation photons to higher-energy luminescence photons [61]. There are many different mechanisms by which a material can combine the energy absorbed from multiple photons and deliver that energy to a single luminescent center. Based on the efficiencies observed, the most likely upconversion processes are excited-stated absorption (ESA) and energy transfer upconversion (ETU) [61]. Both of these processes involve sequential absorption of excitation photons. ESA occurs when a luminescent center undergoes an absorption event. Then, while in an excited state, it undergoes another absorption event. ETU takes place when two absorption events occur at two adjacent sites in the material. Energy is then transferred from one site to a luminescent center. This energy conversion places the acceptor in a higher energy state and the donor in a lower energy state. Both ESA and ETU involve real energy states with long lifetimes, which are necessary to allow time for the second absorption event or energy transfer event to occur. Based on the difference between the time constants associated with the rising and decaying portion of the

luminescence temporal profile, the most likely upconversion mechanism is ETU [61]. Furthermore, it appears that reducing the temperature of the glass host material either inhibits absorption or energy transfer, therefore resulting in reduced luminescence intensity. This explanation is plausible as the interatomic distances change as a result of the thermal expansion coefficient.

SUMMARY

We have reported the observation of luminescence from the microscope objective of our two-photon PQO system. We also reported on the characteristics and possible mechanism of this luminescence. Although more research is needed to definitively determine the mechanism behind the luminescence, this research effort falls decidedly outside this project's scope and is left for future work.

The luminescence described is very similar in temporal profile and spectral content to the PQO signal we are trying to detect. It is therefore difficult to filter out and negatively impacts our signal-to-background ratio, which presents a challenge for taking accurate and robust measurements. In an effort to improve the accuracy of our measurements under poor signal-to-background conditions, we developed and published a technique that relies on frequency-domain lifetime determination [62]. However, even though the technique was demonstrated to be useful in general, in this application it failed to produce the needed accuracy because our instrumentation did not posses adequate dynamic range. Also, the likelihood of saturation of the focal volume further restricted the usefulness of the technique for this application. We observed that the intensity of the interfering luminescence decreased dramatically at a longer excitation wavelength. This data provided a possible solution to the problem. Assuming our PQO molecular probe

showed good luminescence at longer excitation wavelengths, tuning the excitation laser to longer wavelengths could solve the poor signal-to-background problem.

Chapter 5: Method Optimization

INTRODUCTION

In this chapter, I discuss our efforts to optimize the signal-to-noise ratio (SNR) of the two-photon PO_2 measurement technique. Based on the scientific literature related to two-photon PQO [48, 63], we expected one of our research challenges to be low signal levels from our porphyrin-based molecular oxygen probe. It is known that centro-symetric molecules posses small two-photon action cross-sections. Recall that the product of the luminescence quantum efficiency and two-photon absorption cross-section is commonly referred to as the *two-photon action cross-section*. The two-photon action cross-section can be thought of as the "brightness" of a two-photon fluorophore. Many of the improvements to our collection optics discussed in Chapter 2 were motivated by the desire to mitigate the low cross-section of our original porphyrin-based oxygen probe.

EVALUATION OF OTHER MOLECULAR OXYGEN PROBES

Molecular Oxygen Probes Considered

In addition to Oxyphor R2 (the molecular oxygen probe used in our preliminary data), we evaluated other probes to see which one was best suited for two-photon PQO. To determine which oxygen probe performed the best, we used the following criterion: the SNR of the PO_2 calculation in conjunction with the temporal resolution. In this case, we defined the temporal resolution as the time needed to achieve a PO_2 SNR arbitrarily set by us. The three molecular probes that we evaluated were Pd-meso-tetra-(4-carboxyphenyl) porphyrin (Oxygen Enterprises, Oxyphor R2), a ruthenium-based probe called Tris(2,2′-bipyridyl)dichlororuthenium(II) hexahydrate (Sigma-Aldrich, #224758), and a new porphyrin-based probe called PtP-C343, which became available during the

course of this work. PtP-C343 was chemically engineered by Dr. Sergei Vinogradov to solve the inherent low two-photon action cross-section associated with conventional porphyrin molecular oxygen probes [48, 64]. Although the probe was not yet commercially available, Dr. Vinogradov graciously provided enough PtP-C343 for us to perform our experiments.

Oxyphor R2

Oxyphor R2 is a commercially available oxygen probe that is highly water soluble and well established in the scientific literature as a one-photon oxygen probe [54, 65-68]. The compound is a polyglutamic dendrimer with a Pd-Porphyrin core (Figure 27). It is the Pd-Porphyrin core that absorbs light and phosphoresces. Attached to the periphery of the glutamic denrimer are 16 negatively charged carboxylate groups. This highly negative net charge makes the otherwise hydrophobic Pd-Porphyrin core water soluble at physiologic pH.

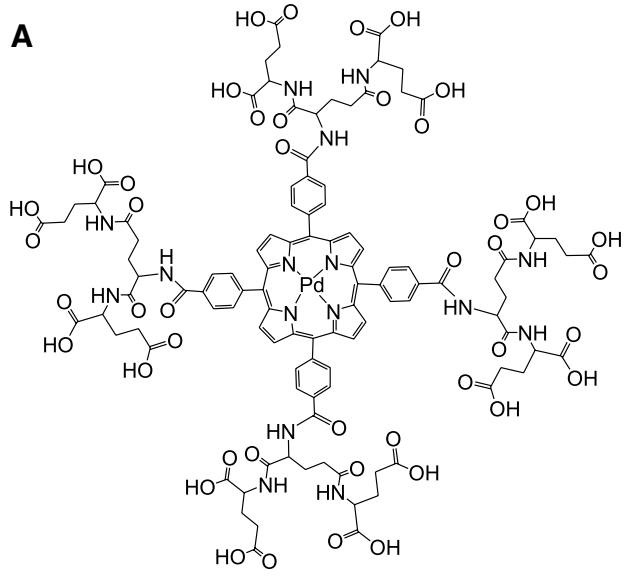

Figure 27: Chemical structure of Oxyphor R2. Reproduced from [68]

The dependence of the observed lifetime of Oxyphor R2 on PO_2 has been shown to follow the Stern-Vollmer relationship (Figure 28) [68].

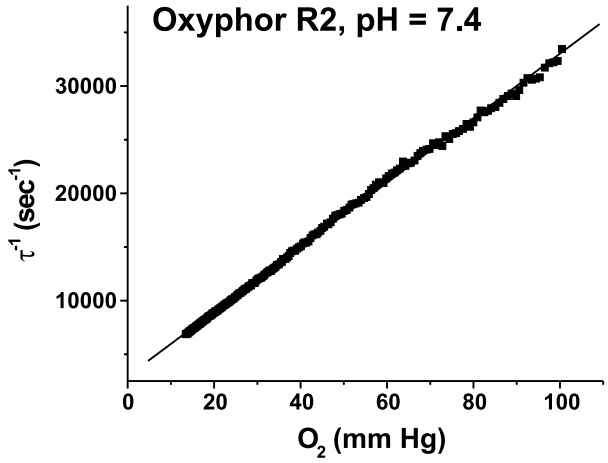

Figure 28: Reciprocal of observed lifetime of Oxyphor R2 as a function of PO_2. Reproduced from [68]

The calibration constants for Oxyphor R2 have been well characterized [68] unquenched lifetime was reported to be ~ 640 μS at 33 degrees Celsius. The quenching constant was reported to be 345 $mmHg^{-1}$ s^{-1}. Recall from Chapter 1 that the quenching constant is a measure of the kinetics and efficiency of energy transfer of the quenching process. The value of the quenching constant can therefore change dramatically when the local environment of the molecule affects these kinetics. This fluctuation occurs when Oxyphor R2 is dissolved in blood plasma, as is necessary for intravascular, *in vivo* measurements. Under these conditions, Oxyphor R2 spontaneously binds to the albumin in the blood, which impedes the access of oxygen to the porphyrin core. As the ratio of albumin to Oxyphor R2 increases, the value of the quenching constant is reduced. However, this effect quickly saturates given nominal Oxyphor R2 concentrations and the

normal concentration of albumin in blood plasma (4-6% by weight). The quenching constant reported above should be accurate to within 10% as long as the ratio of albumin to Oxyphor R2 is > 1.1 [52]. This ratio corresponds to maintaining the concentration of Oxyphor R2 in the blood below ~ 420 μM.

Ruthenium Complex

We chose to evaluate ruthenium complexes based on their wide use commercially as phosphorescence-quenching oxygen probes. In the majority of these commercial applications, the ruthenium complex is immobilized in a sol-gel at the end of a fiber optic probe, which is inserted into an aqueous sample. As such, these ruthenium complexes are not dissolved in the solution. We desired to test these complexes to determine how they would perform as injectable, two-photon PQO molecular probes for *in vivo* application. Although ruthenium probes are less established in the scientific literature than porphyrin-based phosphorescence-quenching oxygen probes, a number of articles describe the use of freely dissolved ruthenium probes for PQO. However, most of them refer to *in vitro* applications [69-73]. We were able to find only one article that described the use of a ruthenium complex for PQO *in vivo* [43]. In this research article, Paxian et al. image oxygen distribution within the exposed liver cortex of a rat. In the process, they document the potential toxic effects of the ruthenium complex and describe an injection protocol that keeps the concentration of the complex below the toxicity threshold. It should be noted that the Paxian paper relied on the intensity of the phosphorescence as an indicator of oxygen distribution. Therefore they demonstrated imaging of relative oxygen distribution only. The question of calibration was completely avoided. In all of these articles, one-photon absorption was used.

The ruthenium complex we used for evaluation was water-soluble at physiologic pH (Figure 29).

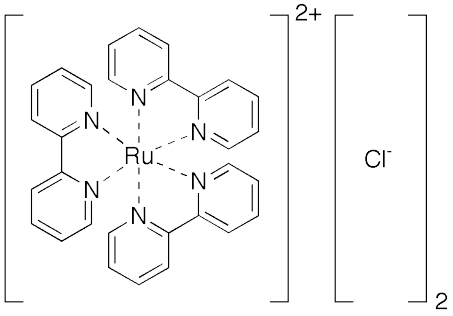

Figure 29: Structure of Tris(2,2′-bipyridyl)dichlororuthenium(II) hexahydrate.

Since the use of this ruthenium complex has not been well established in the scientific literature, its unquenched lifetime and quenching constant are not well characterized. Its lifetime in the presence of oxygen was observed to be ~ 50 ns at physiologic PO_2 values.

PtP-C343

As mentioned above, the PtP-C343 complex was specifically designed for use as a two-photon PQO molecular probe [48, 74]. Its design allows it to overcome the inherent low two-photon action cross-section of centro-symmetric porphyrin molecules. The structure of the complex is depicted below (Figure 30).

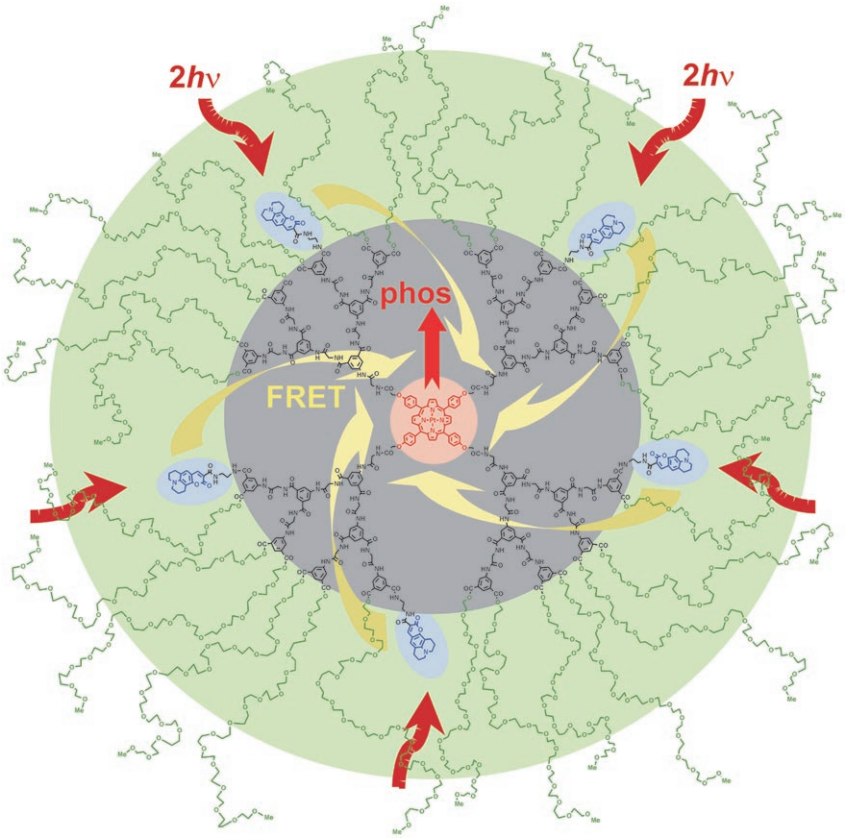

Figure 30: Structure of PtP-C343. Reproduced from [74]

The two-photon enhanced oxygen probe can efficiently absorb energy from the two-photon excitation source via several coumarin-343 moieties (Figure 30, depicted in blue). These moieties have relatively high two-photon absorption cross-sections. Once the energy is absorbed, it can be transferred into the Pt meso-tetraarylporphyrin core (depicted in red) through Fluorescence Resonance Energy Transfer (FRET). Polyarylglycine dendrimers (Figure 30, depicted in black) link the absorbing coumarin moities to the porphyrin core. Finally, oligoethyleneglycol residues (Figure 30, depicted in green) surround the inner part of the molecule. These residues provide a consistent inner environment for the porphyrin core, so that the quenching kinetics do not change

when this molecular probe is used in different environments. Albumin in the blood cannot affect the quenching kinetics since it cannot get close enough to the phosphorescent core to interfere with its interaction with oxygen [74]. Therefore, this two-photon enhanced molecular oxygen probe can be easily calibrated *in vitro*. We can expect the calibration constants to be applicable to intravascular and interstitial PQO measurements. The following plot shows the relationship between inverse lifetime and PO_2 (Figure 31).

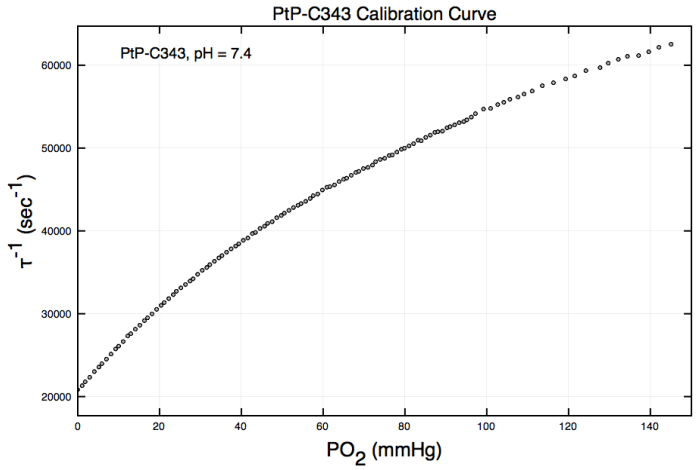

Figure 31: Calibration curve for PtP-C343. Data provided by Dr. Sergei Vinogradov, University of Pennsylvania

As can be seen from Figure 31, the relationship between inverse lifetime and PO_2 does not follow the standard Stern-Vollmer relationship, as is the case with Oxyphor R2. Dr. Vinogradov has provided us with an empirically determined expression to convert the observed phosphorescence lifetime to PO_2. The data from the plot above were re-plotted such that the observed lifetime was the independent variable and the PO_2 value the dependent variable. These data were then fit to an expression that was the sum of two decaying exponentials and an offset term (Figure 32).

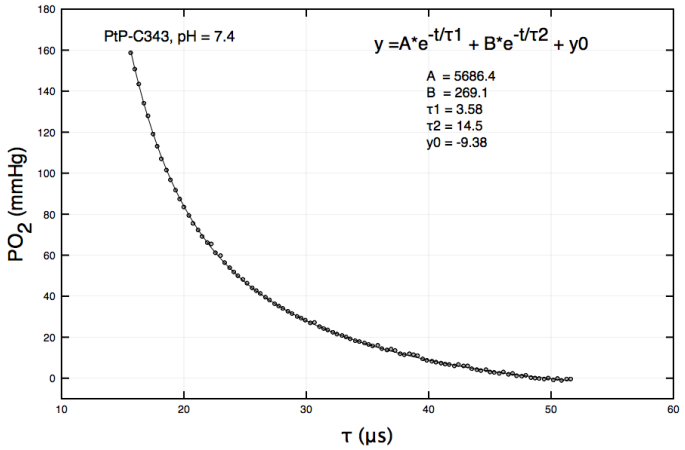

Figure 32: PO_2 vs. lifetime for PtP-C343. Data provided by Dr. Sergei Vinogradov, University of Pennsylvania

The parameters of the expression were varied so as to produce the best fit to the data. With the parameters determined, we now had an expression that could be used to determine the PO_2 value, once the phosphorescence lifetime was known. The quenching constant and unquenched lifetime were reported to be ~ 529.2 $mmHg^{-1}$ s^{-1} and ~55 µs (unpublished correspondence with Dr. Vinogradov).

Measurement of Relative, Two-Photon Action Cross-Sections

Measurements of an absolute two-photon action cross-section can be very challenging in practice. A much simpler approach is to measure the relative, two-photon action cross-section in which the cross-section to be determined is referenced to a fluorophore whose absolute cross-section is well characterized. Our goals in characterizing the two-photon action cross-sections of the three PQO molecular probes were to determine how these cross-sections varied with excitation wavelength and which

probe had the largest cross-section. Since we were only interested in comparisons amongst the three probes mentioned, measurement of the relative two-photon action cross-section was sufficient.

Theoretical Basis for Experiment

Assuming a Gaussian temporal profile of the pulses from our two-photon excitation source, as well as a thick sample, the generated luminescence is approximately given by the following equation [75].

$$F_{generated} = 1.41 C \eta \sigma_{2abs} n_0 \frac{\lambda_{exc}^2 I^2}{f\tau} \qquad (8)$$

In the equation above, C is the concentration of the fluorophore, η is the luminescence quantum efficiency, σ_{2abs} is the two-photon absorption cross-section, n_0 is the index of refraction, λ_{exc} is the excitation wavelength, I is the excitation intensity in units of photons $\cdot$ $sec^{-1} \cdot cm^{-2}$, and f and τ are, respectively, the repetition rate and pulse width of the excitation source. For our purpose of determining the best two-photon PQO probe, we are more interested in the two-photon action cross-section, as this will be one of the primary factors that determine the probe's SNR. The detected luminescence is the generated luminescence times the detection efficiency.

$$F_{\text{detected}} = F_{\text{generated}} \phi(\lambda) \qquad (9)$$

The detection efficiency term $\phi(\lambda)$ includes the collection efficiency of the optics and the spectral response of the detection instrumentation. The numerical aperture of the objective and the transmission of the fluorescence filters are what primarily drive the collection efficiency of the optics. In our case, the material that comprises the photocathode of our PMT primarily determines the spectral response of the detection instrumentation. When we combine these terms into equation 9 , we get the following:

$$F_{\text{detected}} = F_{generated}\phi_{optics}\int_0^{\infty} T_{filter}(\lambda)E_{normalized}(\lambda)R_{instrumentation}(\lambda)d\lambda \qquad (10)$$

In the equation, ϕ_{optics} is the fraction of solid angle from the sphere of generated luminescence that reaches the detector, $T_{filter}(\lambda)$ is the overall transmission spectrum of the filters, $E_{normalized}(\lambda)$ is the area-normalized emission spectrum of the fluorophore, and $R_{instrumentation}(\lambda)$ is the spectral response of the detection system. The integral of the filter transmission times the area-normalized emission spectrum represents the fraction of the total luminescence spectrum that reaches our detector. The following equation describes the ratio of the collected luminescence from the PQO probe solution to the collected luminescence from the reference solution (assuming a constant concentration and intensity):

$$\frac{F_{\text{detected}}}{F'_{\text{detected}}} = \frac{\sigma_2}{\sigma'_2}\frac{\int_0^{\infty} T_{filter}(\lambda)E_{normalized}(\lambda)R_{instrumentation}(\lambda)d\lambda}{\int_0^{\infty} T'_{\text{filter}}(\lambda')E'_{normalized}(\lambda')R_{instrumentation}(\lambda')d\lambda'} \qquad (11)$$

The quantity σ_2 in this equation represents the two-photon action cross-section. The primed quantities in the denominator are associated with the reference fluorophore. In practice, the integrals in the equation have limits of integration that are defined by the limits of the transmission filters' pass band. Since the samples being tested and the reference fluorophore may have significantly differing emission spectra, the transmission filters need not be the same. The numerator and denominator therefore represent distinct integrals with distinct limits of integration. The ratio of these integrals represents a scaling factor for each solution of PQO probe tested such that equation 11 can be rewritten as follows:

$$\frac{\sigma_2}{\sigma_2^{'}} = \frac{F_{\text{detected}}}{F_{\text{detected}}^{'}} S \qquad (12)$$

The scale factor is calculated by plugging in the area-normalized emission spectrum of each PQO probe, along with the corresponding filter transmission spectrum and PMT spectral response, into equation 11. The detected luminescence of the sample and reference are measurable quantities. The ratio of these measured quantities along with the scale factor S allow us to calculate the relative two-photon action cross-section.

Experimental Method

The reference fluorophore used was a solution of 100 μM of fluorescein (Fluka, 46955) dissolved in saline. The solution was placed into a 4 ml glass cuvette (Precision Cells, 23G10) and sealed. 100 μM solutions of ruthenium complex, Oxyphor R2, PtP-C343 were similarly dissolved in saline, placed in 4 ml cuvettes, and sealed. Additionally, 65 mg of glucose (Sigma, G7528-250G) and 6.5 mg of glucose oxidase

(Sigma, G7141-50 KU) were added to the cuvettes to remove any dissolved oxygen from the sample solutions just prior to sealing. The following is a depiction of our cuvette experimental setup (Figure 33).

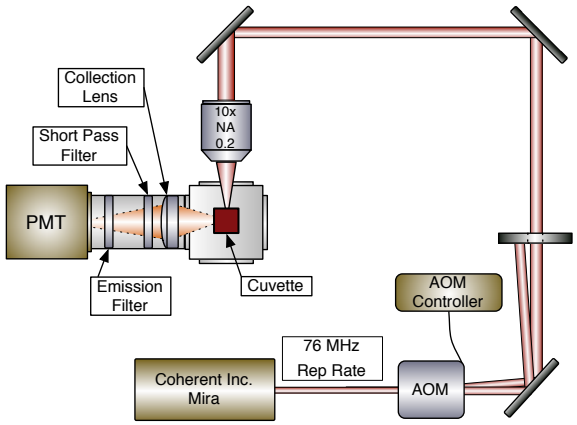

Figure 33: Cuvette experimental setup.

Note that, in contrast to an epicollection setup, this setup prevented the detection system from seeing the in-band light generated when the excitation light interacted with the glass in the objective. This blockage was important since the in-band light would interfere with the measurements. The short pass filter (Semrock, FF01-75m-sp) provided additional blocking of the excitation light. The emission filters were mounted onto a custom fabricated sliding holder, which allowed us to change filters on the fly and take measurements for all fluorophores in rapid succession. The filters used were a Chroma HQ510-80m-2p for fluorescein, a Chroma HQ610-75m for the ruthenium complex, and a Chroma HQ700-75m-2p for Oxyphor R2. The Chroma HQ510-80m-2p was used to detect the residual fluorescence from the coumarin-343 moieties, which results from less than 100% energy transfer efficiency. Additionally, the filter used for detecting the phosphorescence from the Pt-Porphyrin core of the PtP-C343 molecule was the Chroma

HQ700-75m-2p. For these measurements, we used a Hamamatsu H7422P-40 PMT as the detector. Figure 34 shows the normalized spectral response of our detection system including the short pass filter, transmission filters, and response of our PMT.

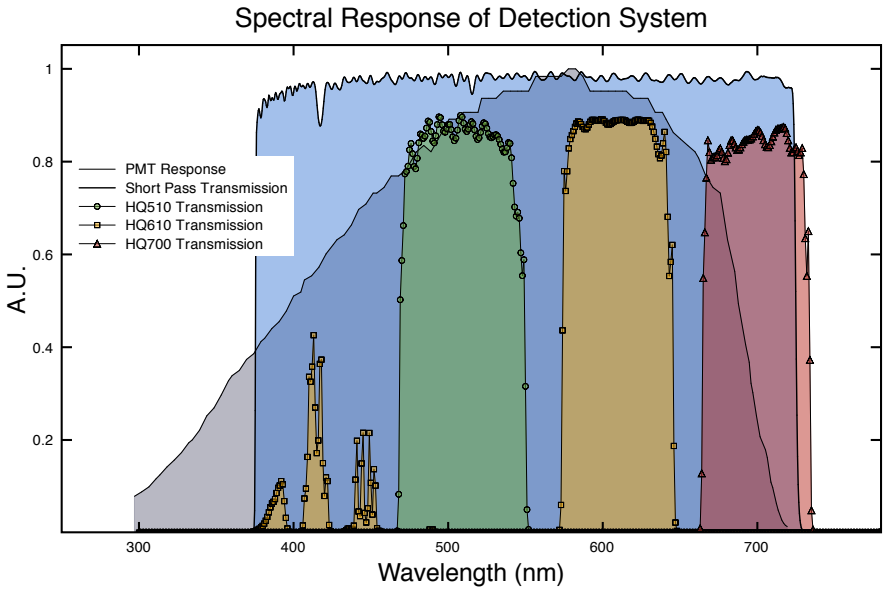

Figure 34: Spectral response of our detection system.

The PMT response curve and transmission curves shown above represent the $R_{instrumentation}(\lambda)$ and $T_{filter}(\lambda)$ used in calculating the integral from equation 11 above. The emission spectra for fluorescein and the PQO probes under consideration are presented in Figure 35 below. We measured the spectra for fluorescein, ruthenium, and Oxyphor R2 using a spectrophotometer. However, Dr. Vinogradov supplied us with the spectrum for the sample PtP-C343. For visual clarity, the spectra in the figure were scaled such that their peaks were equal to one. When used as the $E_{normalized}(\lambda)$ parameter in the integral from equation 11, the emission spectra were first normalized such that the area under the curve was equal to one.

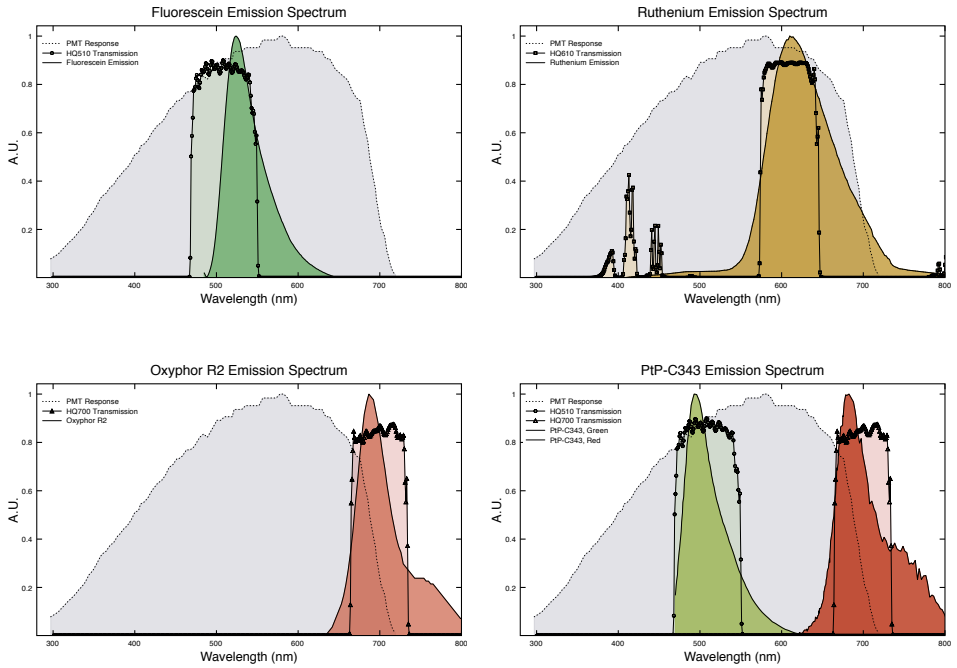

Figure 35: Emission spectra of fluorescein, ruthenium complex, Oxyphor R2, and PtP-C343.

Relative two-photon action cross-section measurements were taken at various excitation wavelengths to determine the wavelength that resulted in the largest cross-section. The excitation power was adjusted at each wavelength to maintain the same number of photons per second, even as the energy per photon was changing. The excitation source used was a Coherent, Mira 900.

Results and Discussion: Ruthenium Complex

Prior to the availability of PtP-C343, our efforts were focused on comparing the two-photon action cross-sections of Oxyphor R2 and the ruthenium complex.

Summarized below are the results of our initial relative cross-section experiments taken with an excitation wavelength of 800 nm (Figure 36).

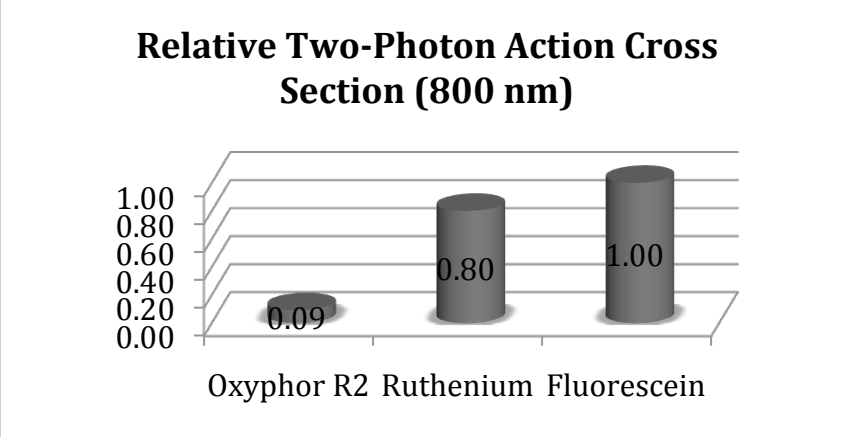

Figure 36: Two-photon action cross-section of Oxyphor R2 and Ruthenium complex relative to fluorescein.

As expected, the two-photon action cross-section of Oxyphor R2 was very low. Researching the published two-photon action cross-section of fluorescein and taking 9% of that value resulted in an estimate of the cross-section that was equal to 3.2 GM [75]. Similarly, an estimate of the ruthenium complex's cross-section, determined by taking 80% of fluorescein's cross-section, was 28.8 GM.

Based on the promising results from the initial relative cross-section measurement, we performed preliminary *in vivo* tests using ruthenium complex as our two-photon PQO probe. Sprague-Dawley rats served as our *in vivo* model. The rats were surgically prepared as described in the methods section of Chapter 3. This preparation included installing a cranial window for optical access to the cortical vasculature and inserting a femoral line for controlled administration of the ruthenium complex solution.

These preliminary *in vivo* tests demonstrated that ruthenium was not well suited for intravascular PO_2 measurements because it extravasated very rapidly.

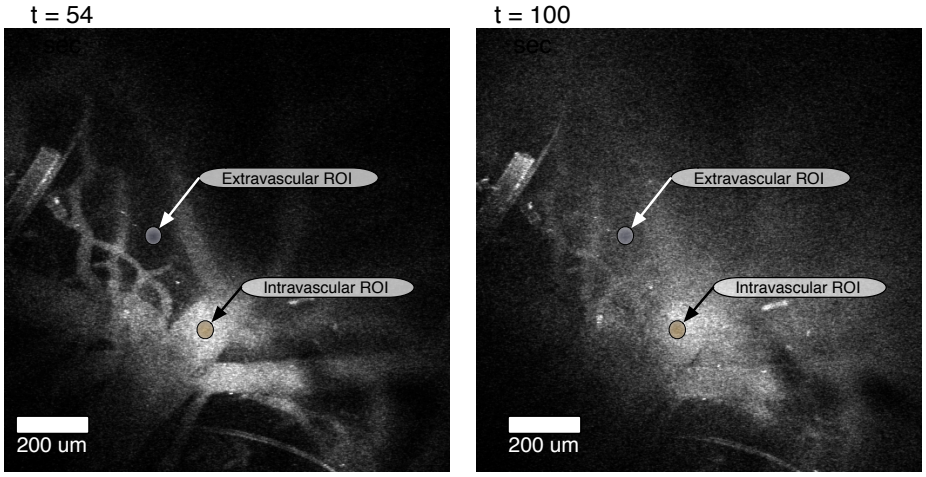

Figure 37: Two-photon luminescence image of rat cortical vasculature with ruthenium complex as contrast agent.

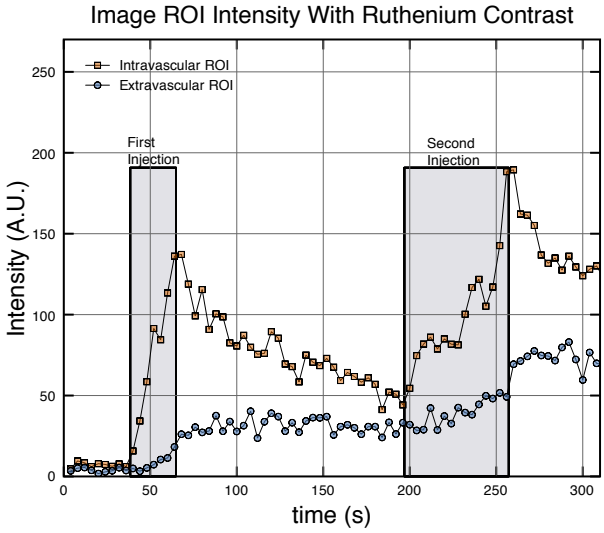

Figure 38: Temporal profile of average pixel intensity of intravascular and extravascular ROI.

Figure 37 above shows two two-photon images taken during and just after injection of 0.6 ml of 100 µM ruthenium solution through the femoral line. Figure 38 plots the average pixel intensity over time for the regions of interest (ROI) highlighted in Figure 37. These figures show that intravascular luminescence increases rapidly during injection but then quickly decays, signifying an increase followed by a reduction in the concentration of the ruthenium probe in the vasculature. Simultaneously, the extravascular luminescence increases during injection and maintains its intensity level. Extravascular luminescence increases further after a second injection. The small size of the ruthenium molecule allows it to easily pass through the blood brain barrier and accumulate in the brain parenchyma.

Phosphorescence decay data from intravascular and extravascular locations were recorded and plotted in Figure 39 below.

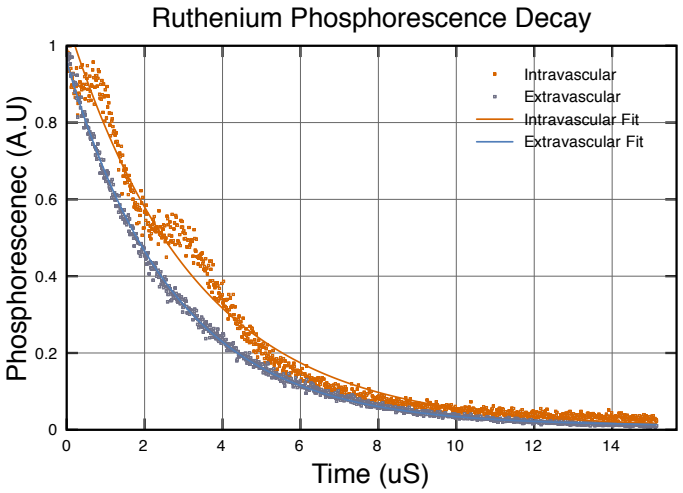

Figure 39: Intravasular and extravascular phosphorescence decay data of ruthenium complex.

The intravascular decay data demonstrate that the kinetics of the quenching process for this probe do not follow a standard single exponential decay process assumed

by the Stern-Volmer equation. This result is likely due to complex interactions between the ruthenium complex and proteins in the blood plasma. The extravascular decay data do show Stern-Volmer-like kinetics and fit well to a single exponential decay model. However, these data imply that the calibration of ruthenium needed to calculate the PO_2 value from a decay lifetime would need to be done in an environment that closely resembles the parenchyma. This is likely to be difficult in practice.

Thus, we chose to focus on porphyrin-based PQO probes for the remainder of this research due to: (1) our primary interest in developing two-photon PQO probes applicable to intravascular PO_2 measurements, and (2) the rapid extravasation and strange intravascular quenching kinetics of ruthenium. Since porphyrin-based probes bind to the albumin in the plasma with high affinity, they remain in the vasculature for hours. Additionally, accurate calibration can be done *in vitro* by ensuring that sufficient albumin is present in the porphyrin-based solution to saturate the quenching kinetics dependence. It should be noted that, although we chose not to pursue ruthenium-based probes in this work, our preliminary *in vivo* experiments demonstrate that they look promising for tissue PQO applications, provided calibration can be achieved. Therefore, they may warrant further investigation as a tissue PO_2 PQO probe. They are especially attractive for cortical tissue PO_2 measurement applications where the blood-brain barrier is usually an impediment.

Results and Discussion: Porphyrin-Based Probes

The measured "brightness" or luminescence intensity for each fluorophore was adjusted to compensate for the differences in detection efficiencies at different

wavelengths. The adjusted intensities were plotted against the excitation wavelength in Figure 40.

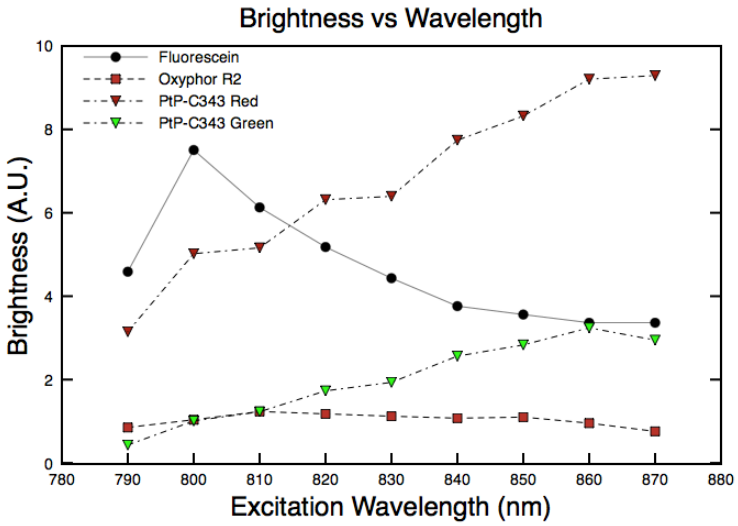

Figure 40: Adjusted luminescence intensity versus excitation wavelength for fluorescein, Oxyphor R2, and PtP-C343.

Oxyphor R2 produces less luminescence as the excitation wavelength increases from 790 nm to 870 nm. The opposite is true for both the green and red luminescence from the PtP-C343 probe. Note that in the range of excitation wavelengths tested, fluorescein has a maximum intensity at 800nm then decreases for longer wavelengths. The trend in our data matches published cross-section measurements for fluorescein [76]. Figure 41 below is a summary of the two-photon action cross-section relative to fluorescein as a function of excitation wavelength. Even though the absolute cross-section of Oxyphor R2 appears to decrease as the excitation wavelength increases, when referenced to fluorescein's cross-section, which decreases more rapidly, the relative cross-section increases slightly with increasing wavelength. The data show that PtP-C343 is up to ~ 7 times brighter than Oxyphor R2.

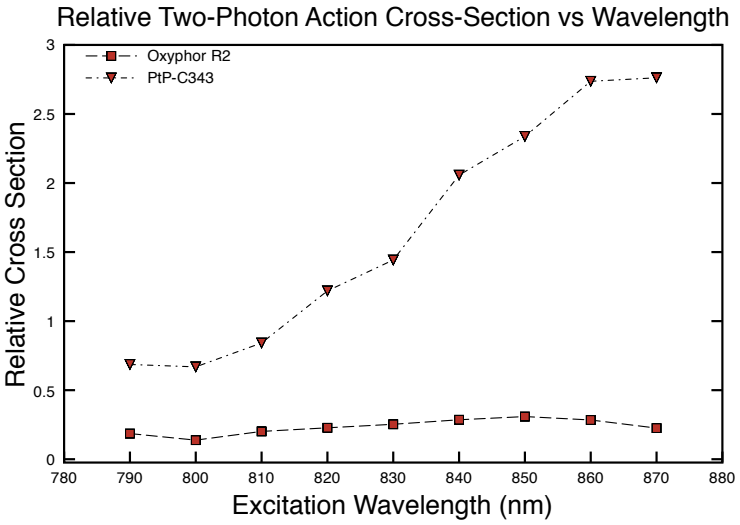

Figure 41: Two-photon action cross-section of Oxyphor R2 and PtP-C343 relative to fluorescein.

By referring to the published values of fluorescein's two-photon action cross-section at the wavelengths tested, we can convert the relative cross-section values to approximate absolute cross-sections. In Figure 42 below, we see the approximate cross-section values.

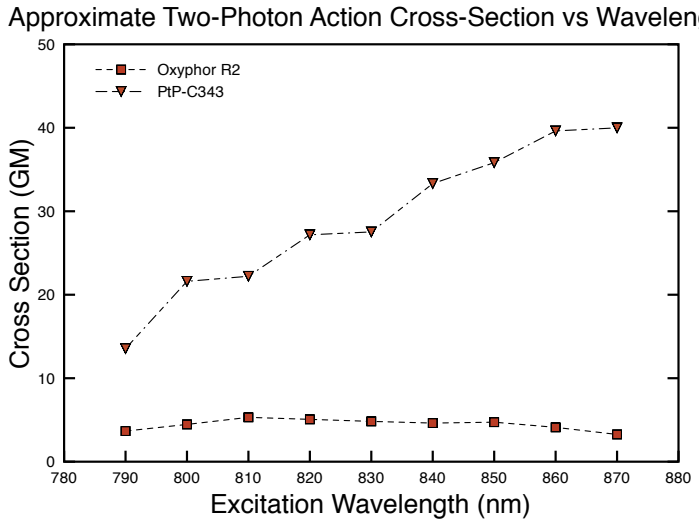

Figure 42: Approximate two-photon action cross-section of Oxyphor R2 and PtP-C343.

Here, we are interested in the two-photon action cross-section of PtP-C343 associated with the phosphorescence of the porphyrin core. This quantity is the two-photon absorption cross-section times the quantum efficiency of the phosphorescence process. In this case, the quantum efficiency includes the fret efficiency. From the data presented in Figure 40, we can ascertain that the absorption cross-section increases with wavelength since both the "red" and "green" luminescence from PtP-C343 increase with wavelength. Additionally, we can ascertain that the FRET efficiency also increases with wavelength since the "red" luminescence increases more rapidly than the "green." This finding suggests that more of the energy absorbed by the coumarin-343 moieties is being transferred to the porphyrin core as the excitation wavelength increases. If we plot the difference between the "red" intensity and "green" intensity divided by the value of the difference at 790 nm, we see that twice as much energy is transferred to the core at 870 nm than at 790 nm (Figure 43).

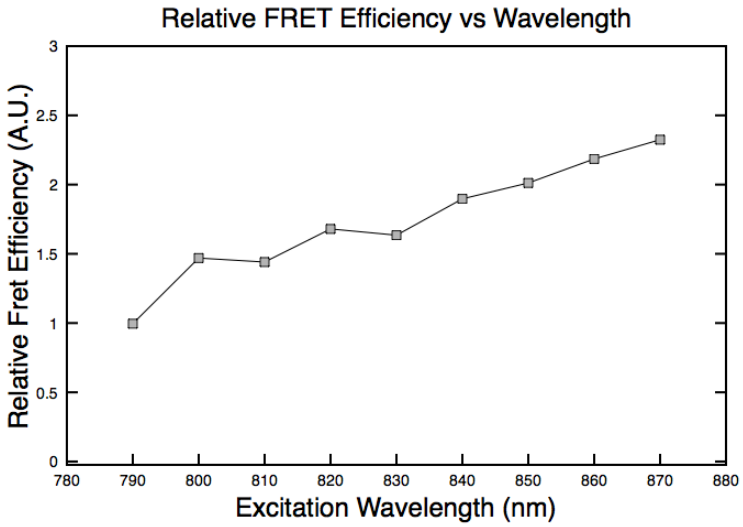

Figure 43: Relative FRET efficiency of PtP-C343 vs. wavelength.

It is significant that PtP-C343 has a larger two-photon action cross-section at longer excitation wavelengths, as the in-band light described in Chapter 4 decreases rapidly with increasing excitation wavelength. This results in a fortuitous situation where the phosphorescence signal is maximized while the background due to in-band light is minimized.

Comparison of Signal-To-Noise Ratio of PO_2 Calculation

Although we have shown that PtP-C343 is ~ 7 times brighter than Oxyphor R2, this does not necessarily mean that it will be the better two-photon PQO probe. The better probe will be the one that produces the best SNR of the PO_2 value in the shortest amount of time. In this section, we derive the expression that relates the SNR of the lifetime measurement to the SNR of the PO_2 calculation. Additionally, we present the results of our PO_2 SNR measurements for Oxyphor R2 and PtP-C343 as a function of integration time.

Theoretical Basis for Experiment

In PQO, PO_2 values are calculated from phosphorescence decay measurements using a calibration model such as the Stern-Volmer equation. Noise in the PO_2 calculations therefore arises as a result of error propagation from the noise in the lifetime measurements. To better understand how the noise translates from lifetime measurements to PO_2 calculations, we can look at how deviations in lifetime produce deviations in PO_2. If we assume that the Stern-Volmer equation relates PO_2 and lifetime

for a given PQO probe, we can solve the Stern-Volmer equation for PO_2 and differentiate with respect to the lifetime τ. Doing so results in the following:

$$\frac{dPO_2}{d\tau} = -\frac{1}{k_q}\frac{1}{\tau^2} \qquad (13)$$

As might be expected, the change in PO_2 per change in lifetime is a function of the quenching constant and the measured lifetime value. If we take the standard error of multiple lifetime measurements to be the discrete change in lifetime, we can use equation 13 above to determine the resulting standard error in the calculated PO_2 value.

$$\Delta PO_2 = -\frac{1}{k_q}\frac{1}{\bar{\tau}^2}\Delta\tau \qquad (14)$$

In the equation above, $\bar{\tau}$ represents the mean of the multiple lifetime measurements, and ΔPO_2 and $\Delta\tau$ represent the standard error in PO_2 and lifetime, respectively. To arrive at an expression for the SNR of our PO_2 estimate, the Stern-Volmer equation, solved for PO_2, is divided by the expression for its standard error.

$$\frac{\overline{PO_2}}{\Delta PO_2} = \frac{\frac{1}{k_q}\left(\frac{1}{\bar{\tau}} - \frac{1}{\tau_0}\right)}{-\frac{1}{k_q}\frac{1}{\bar{\tau}^2}\Delta\tau} \qquad (15)$$
$$= \frac{\bar{\tau}}{\Delta\tau}\left(1 - \frac{\bar{\tau}}{\tau_0}\right)$$

From the expression above, it is clear that the SNR of our PO_2 calculations equals the SNR of our lifetime measurement times the quantity: one minus the fractional change of the lifetime due to quenching. This result agrees with intuition since one would expect that the larger the fractional change in lifetime, the more accurately we can discriminate between PO_2 values. Furthermore, for a given lifetime SNR, PQO probes with lower quenching constants will produce better PO_2 SNR, as the lower quenching constant will produce larger fractional changes in the lifetime. Note that since the phosphorescence decay lifetime is a function of PO_2, the equation for the SNR of the PO_2 calculation above implies that the SNR will vary with PO_2. What follows is an equivalent expression for the SNR of the PO_2 calculation with a more explicit PO_2 dependence:

$$\frac{\overline{PO_2}}{\Delta PO_2} = \frac{\overline{PO_2}}{-\frac{1}{k_q}\frac{1}{\bar{\tau}^2}\Delta\tau} \qquad (16)$$
$$= -\frac{\bar{\tau}}{\Delta\tau}\bar{\tau}k_q\overline{PO_2}$$

As expressed by Figure 31 above, the PtP-C343 PQO probe does not follow Stern-Volmer kinetics. However, a similar process can be used to derive the expression

for the SNR of PO_2 calculations for this probe. In this case, the equation for calculating PO_2 from a measured lifetime is the following (calibration equation from Dr. Vinogradov):

$$PO_2 = Ae^{-\tau/T_1} + Be^{-\tau/T_2} + y_0 \tag{17}$$

The derivative with respect to the lifetime is as follows:

$$\frac{dPO_2}{d\tau} = -\frac{A}{T_1}e^{-\tau/T_1} - \frac{B}{T_2}e^{-\tau/T_2} \tag{18}$$

The SNR of PO_2 calculations using the PtP-C343 probe is therefore given by the following expression:

$$\begin{aligned}\frac{\overline{PO_2}}{\Delta PO_2} &= \frac{\overline{PO_2}}{\left[-\frac{A}{T_1}e^{-\tau/T_1} - \frac{B}{T_2}e^{-\tau/T_2}\right]\Delta\tau} \\ &= -\frac{\overline{\tau}}{\Delta\tau}\frac{\overline{PO_2}}{\overline{\tau}\left[\frac{A}{T_1}e^{-\tau/T_1} + \frac{B}{T_2}e^{-\tau/T_2}\right]}\end{aligned} \tag{19}$$

Dr. Vinogradov also supplied the value of the constants. A and B are 5686.4 mmHg and 269.1 mmHg, respectively. T_1 and T_2 are 3.58 μs and 14.5 μs, respectively. y_0 is -9.38 mmHg.

Similar to the equations for Oxyphor R2, the equations for PtP-C343 PO_2 SNR have the SNR of the lifetime measurement as a multiplicative factor. In general, we

would expect that the SNR of the lifetime measurement would depend on the "brightness" or two-photon action cross-section of the probe. A greater phosphorescence signal would be expected to result in a better lifetime SNR and therefore a better PO_2 SNR.

Experimental Method

All SNR measurements were made through the two-photon microscope setup using the Mira 900 as the excitation source and the AOM for gating of the pulse train (refer to Figure 5 in Chapter 2). To test which PQO probe performed the best we measured the SNR of our lifetime measurements and PO_2 calculations for various integration times. We determined the SNR of our lifetime measurements according to the following procedure. First, we collected 40 decays for each integration time tested. Each decay was least-squares fitted to a single exponential decay model to determine the lifetime. The standard deviation of these values was used as the standard error or, equivalently, the noise. The measured standard error of the PO_2 calculation was determined by first calculating the PO_2 values from the 40 lifetimes, then taking the standard deviation of the results.

The important parameters controlled for the experiment included the AOM on-time, the decay measurement range, the AOM repetition rate, the AOM on-voltage, and the integration time. Figure 44 depicts the definition of these parameters. The integration time is the total amount of time that phosphorescence decay photons are collected. The integration time divided by the repetition period is the number of decays collected.

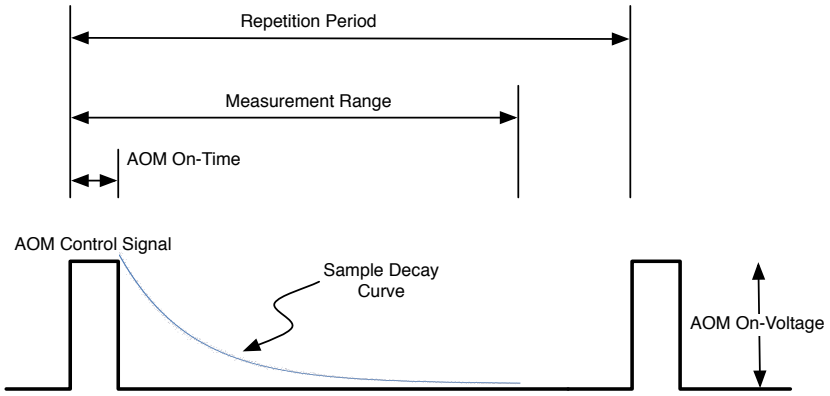

Figure 44: SNR experiment timing diagram.

The unquenched lifetimes of Oxyphor R2 and PtP-C343 differ by approximately a factor of 10. In order to keep the relevant parameters of the SNR comparison equivalent, the timing parameters associated with the experiment were set relative to their respective lifetimes. The following table summarizes the parameters used in the experiment.

	Oxyphor R2	**PtP-C343**
Unquenched lifetime: = τ_0 (μs)	621	54.8
AOM on-time: = 0.05 τ_0 (μs)	31	3
Measurement Range: =5.2 τ_0 (μs)	3200	285
Repetition Period: = 9 τ_0 (μs)	5589	493
AOM on-voltage: (V)	1.5	2.0
Excitation wavelength: (nm)	810	870
Average power at back aperture at wavelength (mW)	2	1.7
Quenching Constant: ($mmHg^{-1}$ s^{-1})	332	NA

Table 3: SNR comparison experiment parameters.

The same sealed cuvettes of 100 μM of Oxyphor R2 and PtP-C343 used in the two-photon action cross-section experiments were employed for these SNR experiments. As described in the experimental methods of "measuring the relative two-photon action cross-section", all dissolved oxygen was removed from the cuvettes prior to sealing. We used the Chroma HQ700 emission filter, Hamamatsu H7422P-40 PMT, and Olympus 20x 0.95 NA objective described previously. Furthermore, we used the Becker and Hickl DPC-230 photon correlator board to build up statistics on the arrival times of photons from the PMT and produce the decay histogram used to determine the decay lifetimes.

Results and Discussion

As mentioned above, all relevant timing parameters associated with the measurement of SNR were determined as factors of the unquenched lifetime of the PQO probes. This procedure allowed us to obtain an equivalent comparison of the intrinsic performance of the probes. For instance, an integration time of 1 second would represent ~ 1,600 decays of Oxyphor R2 and ~18,250 decays of PtP-C343. One would expect that the SNR of PtP-C343 could be greater than that of Oxyphor R2 just by virtue of the fact that more decays were collected. The plot below represents the SNR of our lifetime measurements versus integration time, under anoxic conditions, when all relevant parameters are tied to the unquenched lifetime of the probe under testing.

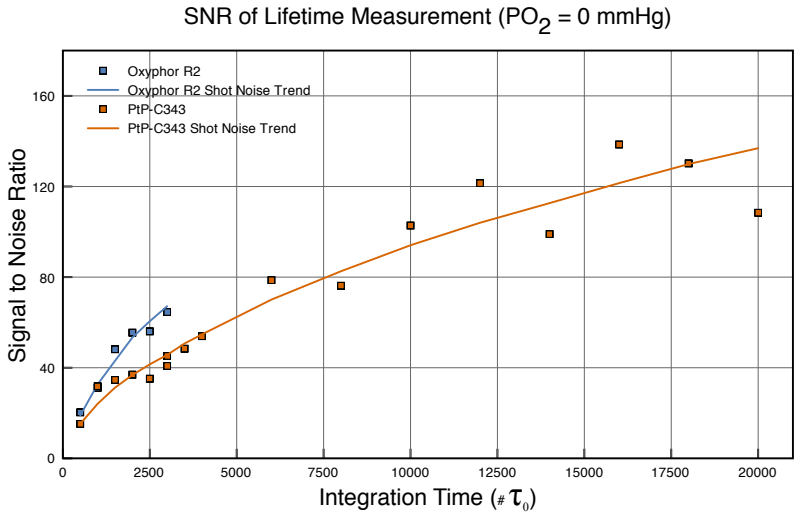

Figure 45: SNRs of lifetime measurement, with integration time taken as # of decay times, under anoxic conditions for Oxyphor R2 and PtP-C343.

From Figure 45, we see that, when integration time is taken as the number of decay times, the SNR of lifetime measurement is better for Oxyphor R2 than PtP-C343, under anoxic conditions. The integration time for Oxyphor R2 was measured out to only $3000\,\tau_0$ because, given the longer lifetime of Oxyphor R2, this represented the upper limit of absolute integration times that would be used in real, *in vivo* PO_2 measurements. Taking the abscissa of integration time to be the number of decay times was the more equitable method for comparing the intrinsic performance of the two PQO probes. However, taking the integration time to be the absolute time was the more practical and useful representation of the data (Figure 46).

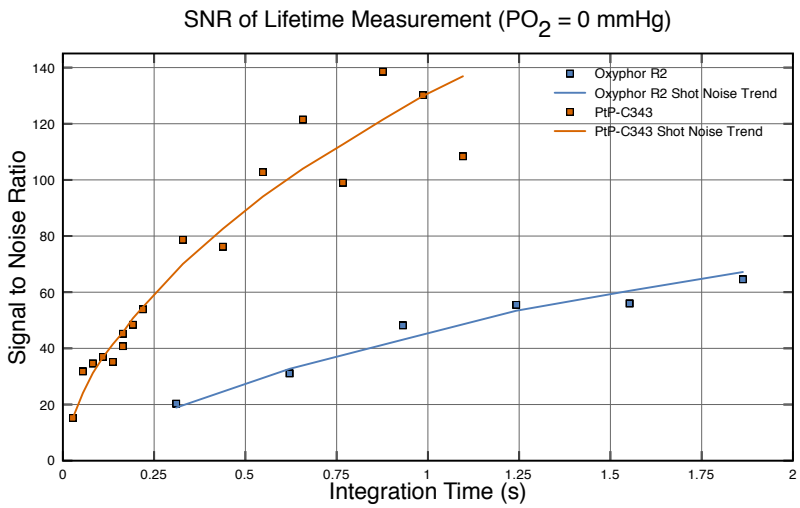

Figure 46: SNRs of lifetime measurement, with integration time taken as absolute time, under anoxic conditions for Oxyphor R2 and PtP-C343.

In this form, we can see that although the SNR of the lifetime measurement for Oxyphor R2 is better for a given number of decays, the SNR of the lifetime measurement for PtP-C343 is better for a given absolute integration time. This stems from the fact that, as determined from our cross-section experiments, PtP-C343 is ~7.5 times brighter than Oxyphor R2. We expect that the increased cross-section should result in improved SNR. In fact, a very useful finding of these data is that the SNR of the lifetime measurement scales as the square root of the number of photons collected under the decay curve. This is a common feature for optical measurements, where the predominant noise source of the system is the intrinsic shot-noise mechanism associated with arrival rate of photons at the detector. The solid lines in Figures 45 and 46 represent the square root of the scaled summations of the number of photons under the decay curve collected for each measurement. The most likely explanation for why the SNRs do not exactly follow the shot noise trend line is that the lifetime is determined from a fitting algorithm that

introduces an extra aspect of variability. It is likely that small changes in the initial estimates of the fitting parameters result in larger changes in the lifetime estimate. Given that the SNR scales as the square root of the number of photons collected in the measurement, the superior SNR of PtP-C343 is not surprising. We would expect that the SNR of PtP-C343 would be $\sim\sqrt{7.5}$. This is, in fact, the case.

Under anoxic conditions, the SNR of the PO_2 calculation obtained was the following (Figures 47 and 48):

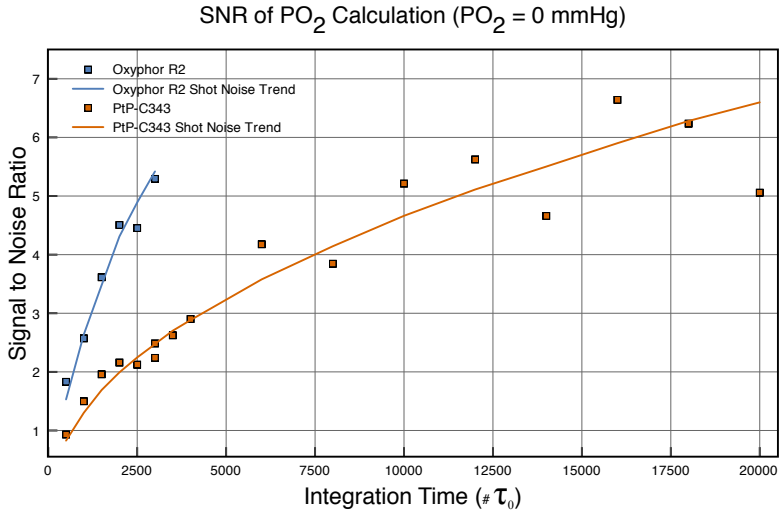

Figure 47: SNRs of PO_2 calculation, with integration time taken as # of decay times, under anoxic conditions for Oxyphor R2 and PtP-C343.

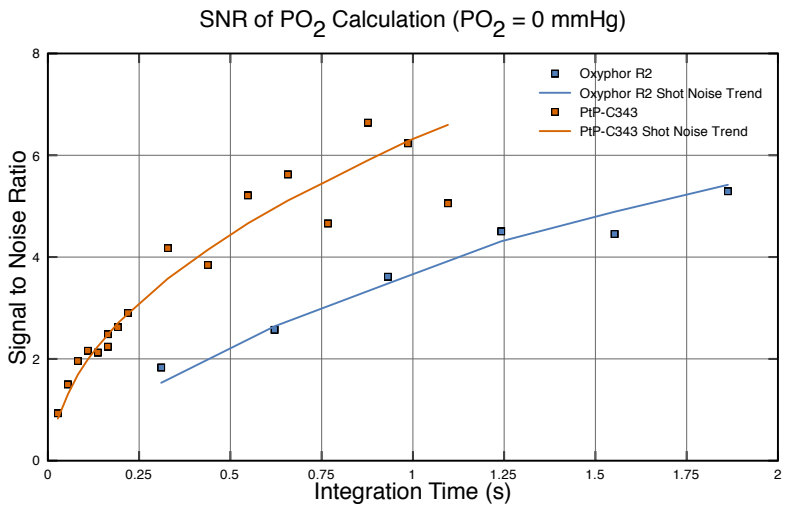

Figure 48: SNRs of PO_2 calculation, with integration time taken as absolute time, under anoxic conditions for Oxyphor R2 and PtP-C343.

Note that the SNR of the PO_2 calculations also follow a shot-noise limited trend line similar to the SNR of the lifetime measurements. Note also that the SNR of the PO_2 calculation is significantly lower than the SNR of the lifetime measurements. Because we have defined the SNR of the PO_2 calculation as the mean PO_2 value divided by the standard error of the PO_2 calculation, we expect the SNR to be near zero, as these measurements were taken under anoxic conditions.

We can estimate the SNR of our PO_2 calculations under non-zero oxygenation conditions by making use of equations 15 and 19, which express the PO_2 SNR as a function of the SNR of the lifetime measurement for Oxyphor R2 and PtP-C343. Since we know that the SNR of the lifetime measurement varies as the square root of the number of the photons collected under the phosphorescence decay curve, we can predict the value of the SNR at different PO_2 levels. Because the decay of phosphorescence follows a single exponential decay model, we know how the area under the decay curve will vary at different PO_2 levels. The area under curve is given by the following:

$$\text{Total Photons} = \int_0^{T_{span}} Ae^{-t/\tau} = -A\tau\left[e^{-T_{span}/\tau} - 1\right] \tag{20}$$

In this case, T_{span} is the measurement range. Because the measurement range is 5 times the expected lifetime, the decaying exponential term of the definite integral is approximately zero, and the area under the curve is approximately $A\tau$. Since the measured lifetime is decreased due to increased quenching at higher PO_2 levels, we expect to collect fewer photons under these conditions. If τ is the measured lifetime at some nonzero PO_2 level, and τ_0 is the measured lifetime under anoxic conditions, then the total number of photons collected will decrease from the anoxic case by a factor of $\frac{\tau}{\tau_0}$. Therefore, we can predict that the SNR of lifetime measurements will decrease from anoxic conditions as follows:

$$SNR_{oxygenated} = SNR_{anoxic}\left(\frac{\bar{\tau}}{\bar{\tau}_0}\right)^{\frac{1}{2}} \tag{21}$$

By replacing the lifetime SNR term in equations 15 and 19, we obtain expressions for the PO_2 SNR at non-zero PO_2 levels. The expected lifetime for a given PO_2 value is found by solving the calibration equation for lifetime instead of PO_2 value. The expression for the PO_2 SNR of Oxyphor R2 is the following:

$$SNR_{PO_2}(PO_2) = SNR_{\tau_0}\left(\frac{\bar{\tau}}{\bar{\tau}_0}\right)^{\frac{1}{2}} \bar{\tau} k_q PO_2 \qquad (22)$$

And the expression for the PO_2 SNR of PtP-C343 is the following.

$$SNR_{PO_2}(PO_2) = SNR_{\tau_0}\left(\frac{\bar{\tau}}{\bar{\tau}_0}\right)^{\frac{1}{2}} \frac{PO_2}{\bar{\tau}\left[\frac{A}{T_1}e^{-\bar{\tau}/T_1} + \frac{B}{T_2}e^{-\bar{\tau}/T_2}\right]} \qquad (23)$$

In the equations above, SNR_{τ_0} is the SNR of the lifetime measurement under anoxic conditions. For our comparison between the two PQO probes, we chose the lifetime measurement SNR at an integration time of 0.6 seconds, since this was a reasonable integration time for *in vivo* measurements. Below is a plot of the projected SNR in our PO_2 calculation as a function of PO_2 value (Figure 49).

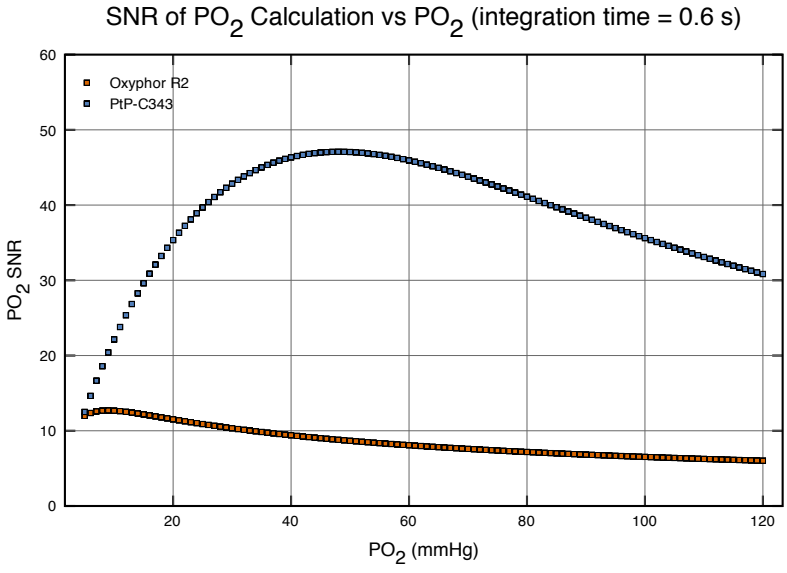

Figure 49: SNRs of PO_2 calculation versus PO_2 level for Oxyphor R2 and PtP-C343.

Taking the ratio of the PtP-C343's SNR to Oxyphor R2's demonstrates how much greater the PO_2 calculation SNR is for PtP-C343.

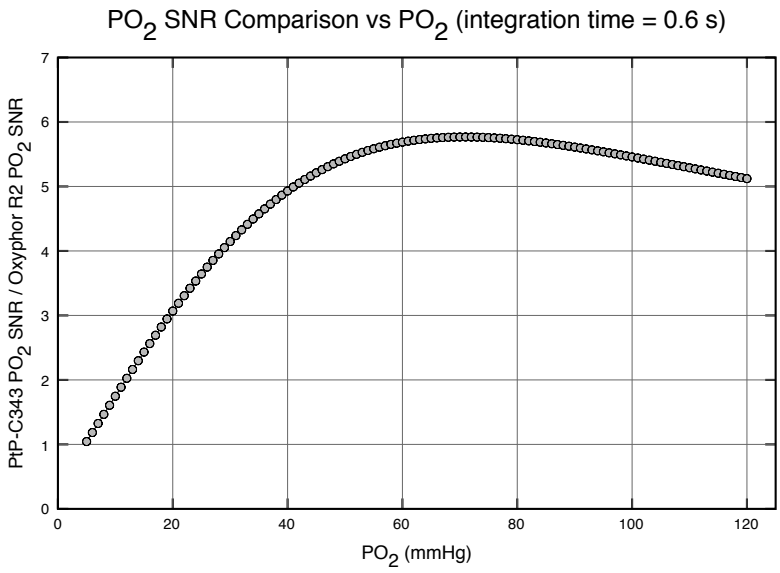

Figure 50: PO_2 calculation SNR of PtP-C343 relative to Oxyphor R2 versus PO_2 level.

From Figure 50 above, we see that the SNR of the PO_2 calculation at first increases, then decreases. The increase is due to the increasing PO_2 value, which is in the numerator of the SNR expression. The subsequent decrease is driven by the increased quenching at higher PO_2 values, leading to decreased SNR of the lifetime measurement and therefore decreased SNR of the PO_2 calculation.

OPTIMAL NUMERICAL APERTURE OF MICROSCOPE OBJECTIVE

As was discussed in Chapter 2, using a high NA, low magnification microscope objective maximizes collection efficiency and in general produces the best image results.

It was mentioned that the high NA was important because it results in a greater acceptance angle for collection of the emitted light. In general, a higher NA objective also produces a tighter focus of the excitation light, resulting in greater confinement of the generated fluorescence and therefore improved spatial resolution in both the radial and axial dimensions. With a higher NA objective, the same total amount of fluorescence is being produced from a smaller volume [76]. Therefore, a larger percentage of the fluorophore molecules in that volume must absorb and emit fluorescence. In general, this works as an advantage, producing better resolution. However, if the lifetime of the fluorescent molecule is much longer than the repetition period of the excitation source, the excited molecules will not have sufficient time to relax to the ground state, and saturation may occur. Further increases of the NA will then reduce the generated fluorescence since the focal volume will be reduced, but further increases in the percentage of fluorophore molecules excited are not possible. Given the relatively long lifetimes of the two PQO probes being tested, saturation is likely to occur. In fact, it can be advantageous to induce saturation, which ensures maximal phosphorescence signal. If we assume a saturation condition, producing a larger focal volume results in a stronger signal as the excitation volume will be larger. Under saturation, a trade-off exists between improving spatial resolution and maximizing the signal from our PQO probe. By under-filling the back aperture of our high NA objective with the excitation beam, we can produce larger focal volumes and therefore more signal under saturation, while maintaining superior collection efficiency. The back aperture of our Olympus 20X, 1.0 objective has a 17 mm diameter. We originally expanded the excitation beam from a diameter of 3 mm to a diameter of 18 mm using a 6X beam expander, as described in Chapter 2. In our optimization effort, we changed the beam expansion to only 4X. This was accomplished by changing the scan lens to a 30 mm focal length lens (Thorlabs,

AC254-30-B) while keeping the 120 mm focal length tube lens (Thorlabs, LB1106-B). The result was a 12 mm diameter excitation beam, which produced an effective NA of ~ 0.70 for the excitation while maintaining the 1.0 NA for the collection.

SUMMARY

In this chapter, I have presented our findings on ways to improve upon the two-photon PQO technique described in earlier chapters of this dissertation. In particular, we investigated techniques to enhance the combination of SNR and temporal resolution. We have found that the following parameters produce the best results. The PQO probe that produced the best SNR for a given measurement time was PtP-C343. Moreover, the optimal excitation wavelength to use with this probe is 870 nm. At this wavelength, SNR is maximized and generation of in-band background light is minimized, resulting in an optimal signal-to-background condition. Additionally, we found that signal is maximized when we induce saturation and under-fill the back aperture of our objective. Under-filling decreases the effective NA of our excitation while maintaining the full NA of the objective for collection. In our case, the back aperture of the microscope objective is 17 mm in diameter. We chose to expand the excitation beam to 12 mm in diameter.

Chapter 6: Further In Vivo Demonstrations

INTRODUCTION

In previous chapters of this dissertation, I have discussed the importance of developing a better method for measuring dissolved oxygen both within and outside the vasculature. I have also described our approach of combining two-photon microscopy with PQO and detailed the instrumentation needed to duplicate our system. Furthermore, I included one of our publications, which presents the first image-guided, two-photon PQO measurements. In this chapter, I will present images and data that further illustrate how the combination of two-photon microscopy with PQO is a powerful tool for researching oxygen transport at the microscopic scale. Additionally, I will briefly discuss the logical next steps to continue this research effort.

THREE-DIMENSIONAL IMAGING OF THE MICROVASCULATURE

As was noted in Chapter 1, one of the strengths of TPM is the ability to produce high resolution, depth-resolved images *in vivo*. Acquiring TPM image stacks, where images are acquired at incrementally deeper locations, results in a data set that can be used to produce three-dimensional model renderings of the vasculature. Spatial resolution typically achieved in this project was ~ 500 nm lateral and 1 μm axial. This resolution was more than adequate for imaging even the smallest blood vessels. For this project, we chose to focus on imaging cortical microvasculature as researchers have shown great interest in oxygen transport within the cortex [12, 77-82]. The following image exemplifies an image stack of mouse vasculature in the cortex displayed as a three-dimensional model (Figure 51).

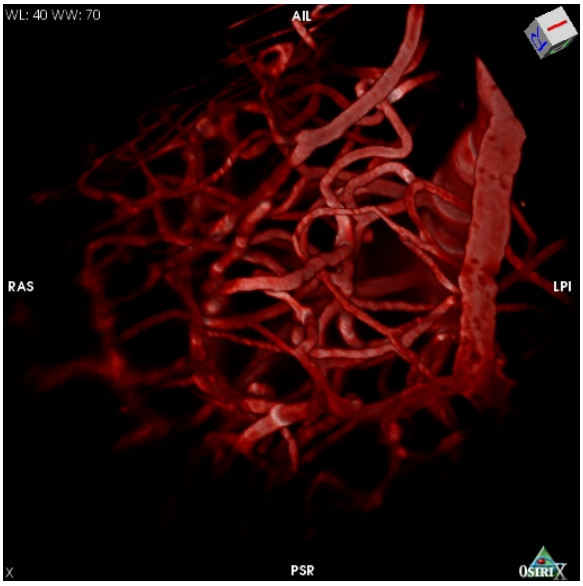

Figure 51: 100 µm x 100 µm image stack of mouse cortical vasculature from surface down to 420 µm.

The mouse surgical preparation followed a chronic, cranial window protocol described online [83]. Briefly, the procedure consists of anesthetizing the animal, removing the scalp, performing a craniotomy, implanting an optical window, and injecting a contrast agent for visualizing the vasculature. For the contrast agent, we injected 0.2 ml of 5% weight by volume fluorescein-dextran in saline retro-orbitaly.

BLOOD VELOCITY MEASUREMENTS

Another capability of TPM that is useful for investigating oxygen transport is absolute blood velocity measurement. TPM can provide this measurement because it has sufficient spatial and temporal resolution to track red blood cells as they move into the image's field of view. In practice, red blood cell tracking is done with a line scanning technique. By repeatedly scanning the excitation focal volume in a line through the

lumen of a fluorescently labeled blood vessel, banded images are produced with velocity information encoded in the slope of the bands. To understand how this works, remember that when a vasculature contrast agent is injected into the animal model, only the blood plasma is labeled. The red blood cells appear in the images as negative contrast artifacts flowing through the lumen of the vessel. When the focal volume is line-scanned once through the lumen, the image intensity values in that line will be bright through the plasma and dark through a red blood cell. In the next line of the image, the dark portion of the line will have shifted over slightly as the red blood cell will have traveled some small distance due to the blood flow. Repeating this process thousands of times results in a banded image where the x-direction represents the length of the line-scan and the y-direction represents the time over which the line scans were performed. Each pixel in the y-direction constitutes one line time. The slope of the dark bands therefore represent the distance traveled along the lumen of the vessel for a given line time increment. This value is, of course, the absolute velocity. Further explanation of this technique can be found in the following references [45, 77].

To do absolute velocity measurements, we performed the same chronic mouse surgical preparation referenced above, including the injection of vasculature contrast agent. Figure 52 is representative of the data produced from line-scan velocity measurements.

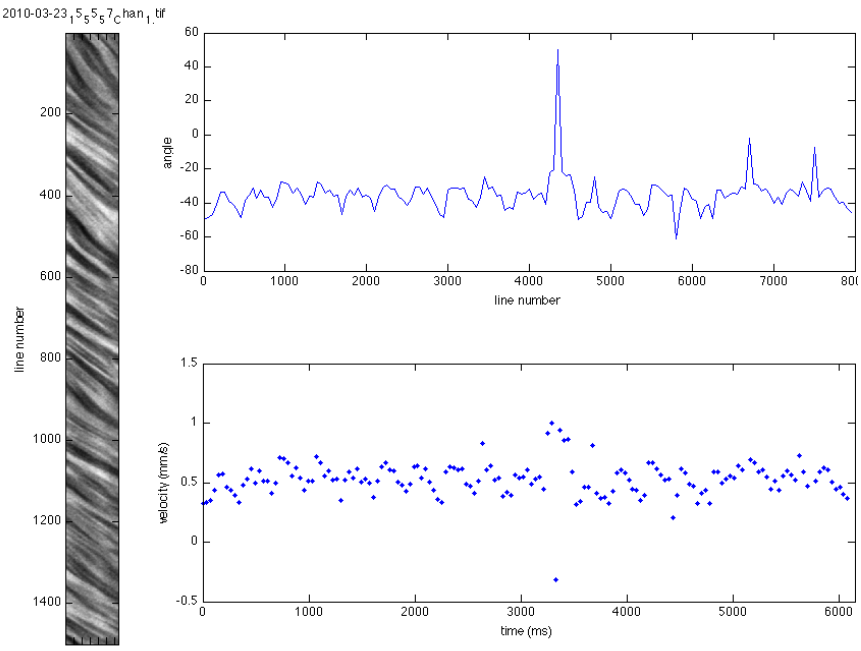

Figure 52: Example of absolute blood velocity measurement using TPM.

We processed the line scan images using Matlab routines supplied by Dr. Chris Schaffer's lab at Cornell University. The data show that detailed absolute velocity measurements are easily made in individual blood vessels. The ripples visible in the velocity profile are due to the pulsetile nature of blood flow caused by the pumping of the heart. The pulse rate implied from the plot matched the pulse rate measured with our mouse pulse oximeter.

CHARACTERIZATION OF ACUTE FOCAL ISCHEMIA

One obvious application of the technique described in this dissertation is to investigate how acute focal ischemia affects oxygen transport. This technique is capable of measuring blood vessel morphology, blood velocity, and dissolved oxygen concentration. The cross-sectional area times the velocity measures the blood flow rate.

Additionally, flow rate information combined with PO_2 results in a measurement of the mass flow of available oxygen through a region of vasculature. Furthermore, knowledge of mass flow dynamics is critical to experimental physiologists investigating the detailed effects of ischemia.

In this demonstration, our experimental animal models were Sprague-Dawley rats. The rats were surgically prepared as described in the methods section of Chapter 3. To induce the acute focal ischemia, we used a photo-thrombosis method [84, 85]. The method entails injecting a photosensitizing agent, which produces an elevated reactive oxygen species concentration when exposed to a photo-initiator. In our case, we used ~ 0.1 ml of 45 mg/ml Rose Bengal as the photosensitizing agent and a 532 nm laser source as the photo-initiator. Once the photosensitizing agent is activated and reactive oxygen species are produced, platelets in the blood respond by releasing clotting factors and initiating a clotting cascade. The result is a thrombus that completely restricts blood flow.

To produce the photo-thrombosis and verify the cessation of blood flow, we modified our microscope setup. Specifically, we added the ability to perform laser speckle contrast imaging (LSCI) so that we could easily visualize blood flow over a large field of view with high temporal resolution. LSCI is a technique that relies on dynamic light scattering and converts motion of scattering centers into image contrast [86]. A diode laser and camera (Basler, A641F) were added to the setup as the LSCI illumination source and imaging device, respectively (Figure 53). An additional dichroic cube was added between the scan lens and tube lens to reflect the LSCI image to the camera. The primary dichroic (Dichroic 1 in Figure 5) was transferred to the new dichroic cube when LSCI was performed.

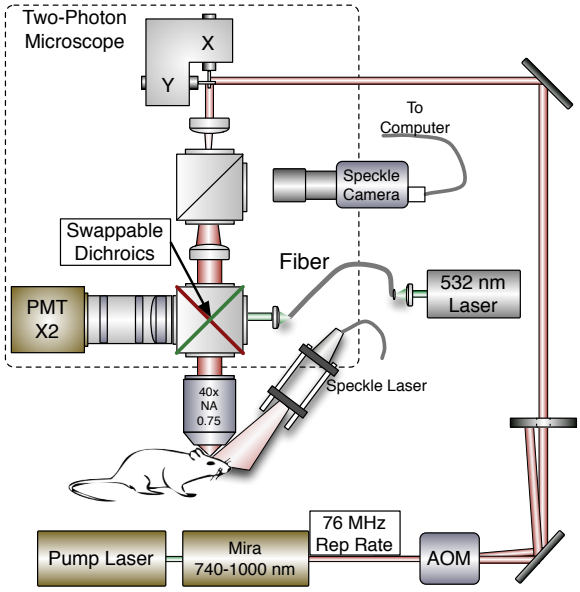

Figure 53: Modified microscope setup to enable LSCI and photo-thrombosis.

For photo-thrombosis, we added an optical fiber for delivery of the photo-initiator light. We coupled a 532 nm laser (Coherent inc, 5W) into the receiving end of the fiber. The delivery end of the fiber was attached to a collimation package to recollimate the laser light. During LSCI, the primary dichroic (Dichroic #1, figure 5) was swapped for a dichroic that was reflective to 532 nm light but transmitted the LSCI laser wavelength. It was therefore possible to perform LSCI while the photo-thrombosis was being formed so that we could monitor and control the process. The 532 nm light was reflected to the microscope objective, where it was focused to an approximately 60 µm spot on the sample. For TPM imaging, the 532 nm laser was turned off, and the primary dichroic was re-inserted.

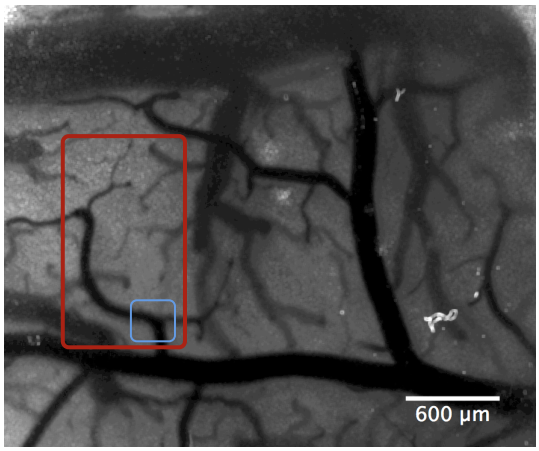

Figure 54: LSCI image of rat cortex before photo-thrombosis.

Figure 54 is an LSCI image before photo-thrombosis. The highlighted region (Figure 54, red) corresponds to the branch of vasculature where velocity and PO_2 data were taken before and after photo-thrombosis. Note that darker contrast represents higher flow.

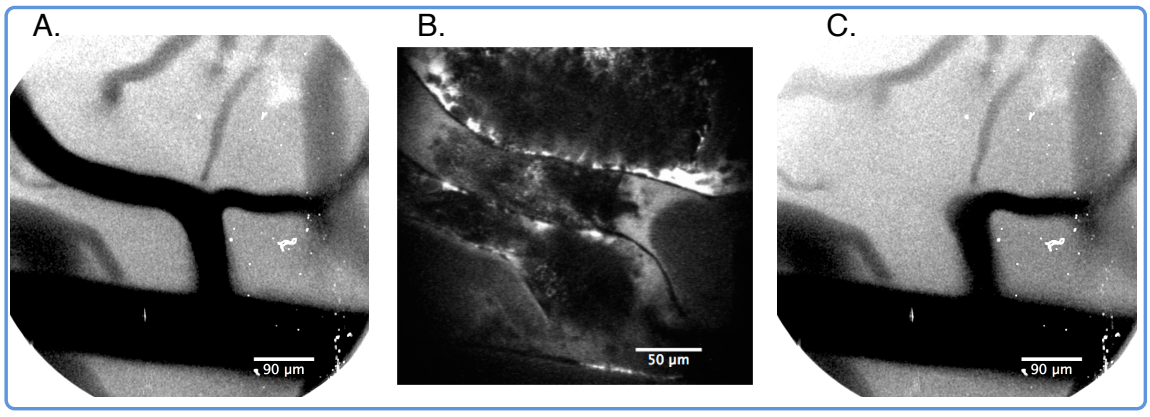

Figure 55: Images of photo-thrombosis.

Figure 55A is an LSCI taken with a 40x objective (0.75 NA, Water) just prior to photo-thrombosis. The thrombus was formed by first administering a 0.1 ml bolus injection of Rose Bengal, then delivering ~5 mW of laser light through the fiber. The

formation of the thrombus was monitored in real-time by concurrently using LSCI while photo-activation was occurring. Irradiation continued for approximately 30 seconds. This was enough time to form a stable thrombus in the blood vessel of interest. Figure 55B is a 40x TPM image of the thrombus in the lumen of the blood vessel of interest. Prior to photo-thrombosis, fluorescein-dextran functions as a TPM vasculature contrast agent. The details of the injection were described in the methods section of Chapter 3. Figure 55C is again a 40x LSCI image, but taken after photo-thrombosis. Note that the left branch appears to be missing in this image compared to Figure 55A. This missing branch signifies a complete blockage of flow.

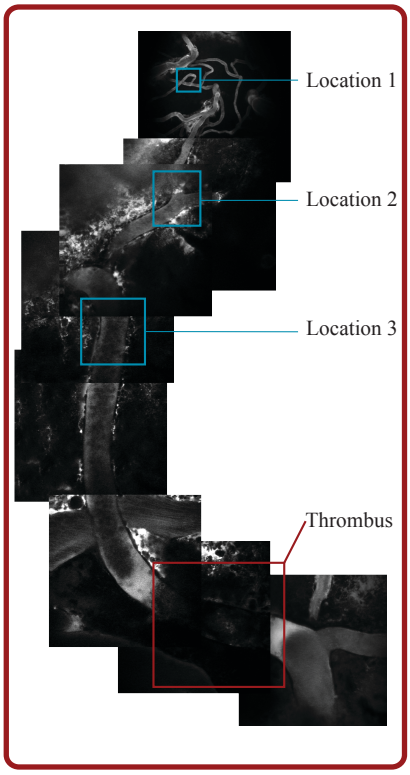

Figure 56: TPM image mosaic of branch of vasculature where velocity and PO_2 data were taken.

Figure 56 is a TPM image of the vasculature branch occluded by the thrombus. It is the same branch highlighted in red in Figure 54 above. Three locations were selected along this branch as locations to take blood velocity and PO_2 measurements before and after photo-thrombosis (Figure 57). These three locations are highlighted in blue in Figure 56.

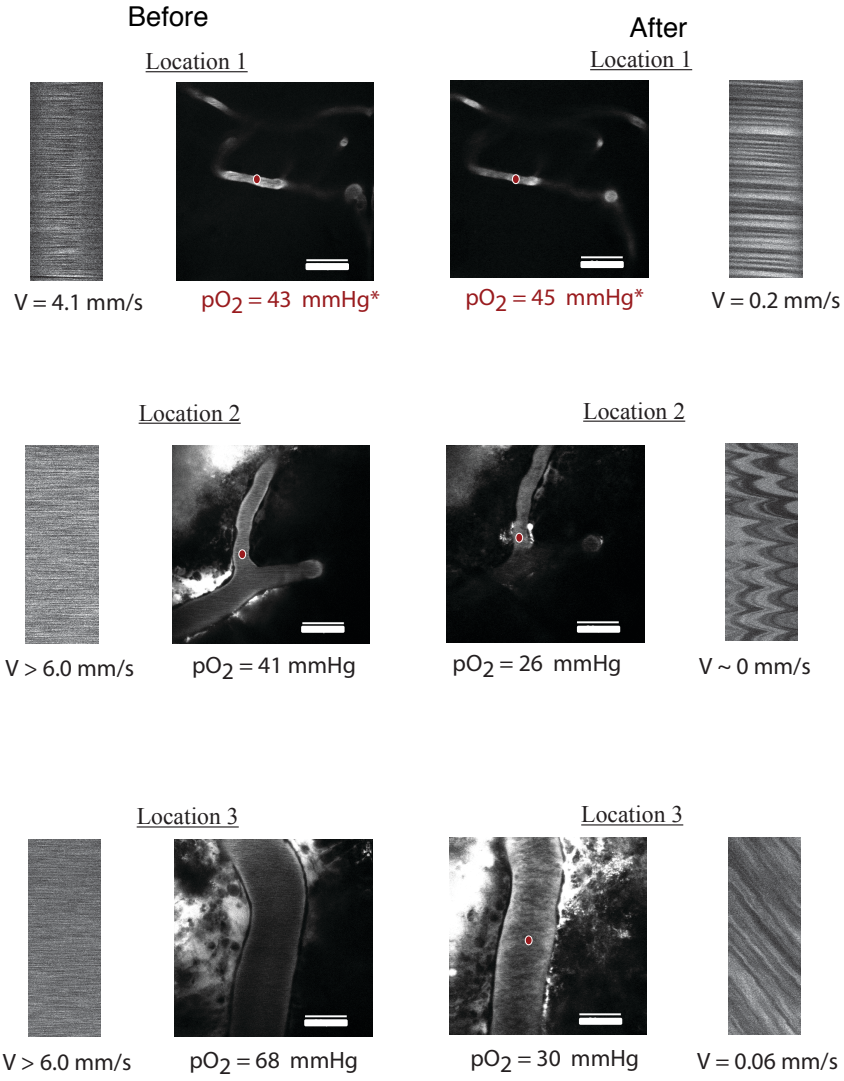

Figure 57: Velocity and PO_2 measurements before and after photo-thrombosis.

Note that the scale bars in figure 57 represent 30 μm. PO_2 measurements were generally made as described in the methods section of Chapter 3. However, for these measurements, the photon-correlator board was used for recording the detector signal. Phosphorescence photons were collected for a duration of 10 seconds for each measurement.

From the data in figure 57, changes in the mass flow rate of oxygen can be calculated at the three locations as a result of the photothrombosis. To do this, we first measure the vessel sizes from the before and after images, to determine the cross sectional areas. In this experiment the blood vessels at the three locations retained their size after the formation of the thrombus. We then calculate the flow rates by multiplying the cross-sectional areas and the measured velocities. Then we multiply the flow rates and the oxygen concentrations to arrive at the mass flow per second past the measurement site. We chose to convert from mmHg to moles/Liter by dividing by the solubility constant for oxygen in water at 25 C (584592 mmHg/Molar). At location 1, the velocity changes from 4 mm/s to 2 mm/s. This corresponding flow change was from 1.5E-10 L/s to 7.7E-11 L/s. Since appreciable flow is maintained after formation of the thrombus, we can assume that it is fed by an additional branch. The PO_2 does not change in response to the thrombus at location 1. The resulting mass flow rate of oxygen changes from 1.1E-14 moles/s to 5.9E-15 moles/s. At location 2, the flow rate changes from 6.8E-10 L/2 to ~0 L/s. The corresponding mass flow rate of oxygen changes from 4.7 moles/s to ~0 moles/s. At location 3, nearest to the thrombus, the flow rate changes from 6.8E-9 L/s to 6.8E-11 L/s. The mass flow rate of oxygen changes from 7.9E-13 moles/s to 3.5E-15 moles/s.

These data were taken prior to the availability of PtP-343 and prior to the upgrades made to our setup. Consequently, better SNR performance in our PO_2

measurements, improved imaging, and improved velocity measurements can be expected when this experiment is repeated with our latest improvements.

IN VIVO PTP-C343 EXPERIMENTS

Samples of PtP-C343 became available late in the course of this research project. Consequently, the data presented in this section are preliminary. Our lab received an initial sample of PtP-C343, which we used in our *in vitro* evaluations, followed by a second sample to be used for our *in vivo* evaluation. For our preliminary *in vivo* evaluation, we sought to measure PO_2 under normal physiologic conditions. To verify that the PtP-C343 probe was in deed sensitive to PO_2 we verified that we could see changes in our measurements in response to changes in the fraction of inspired oxygen (FIO2). The same chronic, mouse surgical preparation referenced above was followed for these experiments [83]. 18 mg/ml of PtP-C343 was dissolved in isotonic saline as our stock solution. 10 ml/kg of the stock solution was injected retro-orbitally, resulting in a probe concentration of approximately 80 μM in the blood plasma. Recall that PtP-C343 contains Coumarin-343 moities, which absorb the two-photon radiation and transfer the energy to the platinum-porphyrin core. Because the transfer of energy is not 100% efficient, residual Coumarin fluorescence is emitted and can be used as the contrast agent for vasculature imaging. In these experiments, a fluorescein injection was not needed to label the vasculature. We used our emission filter centered at 510 nm to detect the residual Coumarin fluorescence for imaging the vasculature.

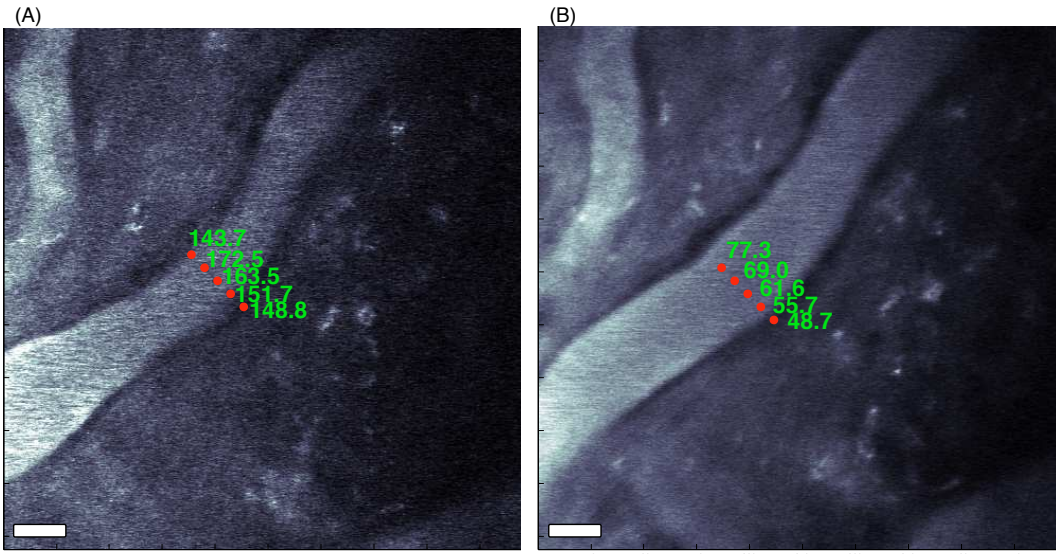

Figure 58: *In vivo* PO_2 data taken with first sample of PtP-C343 we received under hyperoxic (A) and hypoxic conditions (B). Values are in units of mmHg

Figure 58 shows PO_2 data taken 80 µm below the surface. The scale bar in the images represents 60 µm. The hyperoxic data was taken under 100% FIO2 conditions. The mouse arterial oxygen saturation (SAO2) was monitored with a mouse pulse-oximeter. Under hyperoxic conditions, the SAO2 was ~98%. Hypoxic PO_2 data was taken by reducing the FIO2. The SAO2 under hypoxic conditions was ~76%. In both the hyperoxic and hypoxic data, the PO_2 values are higher than what we have typically measured using Oxyphor R2 in blood vessels of this size. Under similar hyperoxic conditions, we have typically measured ~50-100 mmHg for vessels this size. Additionally, under hypoxic conditions, we have typically measured ~20-70 mmHg for similar sized vessels. In our early PO_2 measurements made with Oxyphor R2, we used urethane as the anesthetic; with our more recent data, we used isofluorane. It is possible

that the discrepancy seen in the PO_2 data is due to the fact that urethane is known to suppress PO_2 much more drastically than isofluorane [87].

The experiment described above was repeated using the second batch of PtP-C343 sample that we received (Figure 59).

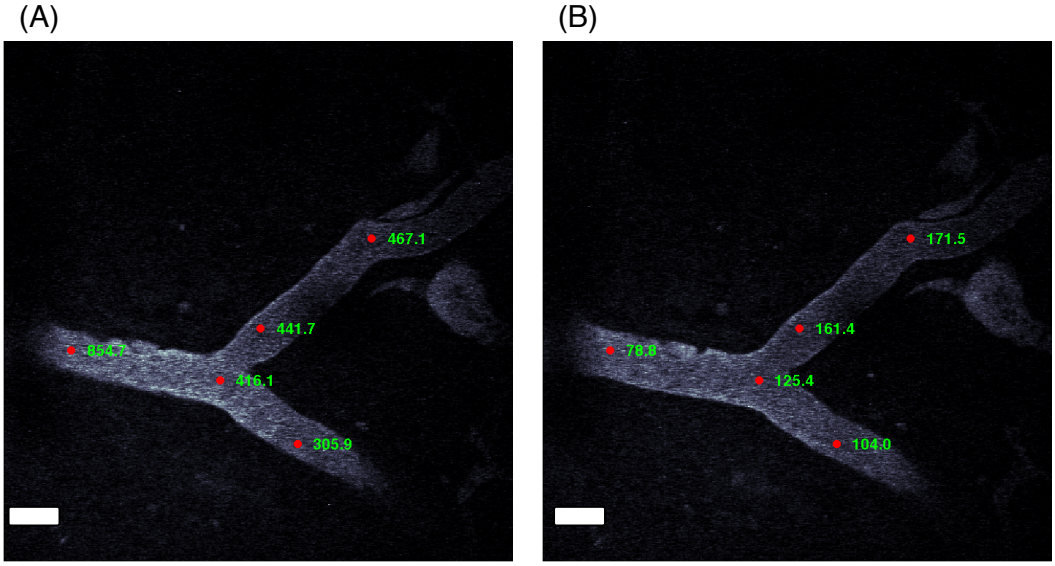

Figure 59: *In vivo* PO_2 data taken with second sample of PtP-C343 we received under hyperoxic (A) and hypoxic conditions (B). Values are in units of mmHg

The scale bar in the images represents 60 μm. The PO_2 data taken with the second sample of PtP-C343 are clearly too high to be accurate. The high PO_2 results were consistent across multiple animals. Why the lifetimes measured with the second sample of PtP-C343 are so short remains a question we are investigating. *In vitro* measurements taken under anoxic conditions resulted in the unquenched lifetimes that we expected. Additionally, calibration data provided to us by Dr. Vinogradov's lab

demonstrated normal lifetime values in the presence of oxygen for this sample of PtP-C343. We are currently working with Dr. Vinogradov to understand why this second sample of PtP-C343 had such different quenching characteristics in our *in vivo* experiments.

Chapter 7: Conclusion

SUMMARY

Due to the current lack of adequate techniques for quantifying dissolved oxygen concentration, many important biomedical research questions have remained unanswered. For instance, there is still debate about questions as fundamental as the primary site within the vasculature of oxygen delivery to cells. In this dissertation, I have described a novel method of quantifying dissolved oxygen concentration *in vivo* that addresses many of the shortcomings of previous techniques. The primary shortcoming of previous techniques is the inability to perform repeated, high spatial resolution PO_2 measurements, throughout a volume of tissue. The technique I have presented here is can perform depth-resolved, high-resolution PO_2 measurements.

The method described combines phosphorescence quenching oximetry with two-photon microscopy. I have presented the theory behind the technique and described the required instrumentation. Additionally, I have included a reprint of our publication in which we report the first demonstration of image-guided, high-resolution, depth-resolved PO_2 measurements. In this dissertation, I have also presented evidence that suggests that many if not all microscope objectives produce anti-stokes shifted luminescence. This luminescence greatly resembles the phosphorescence we detect in our PQO measurements. We looked at ways to optimize the technique and found that using the PtP-C343 phosphorescent oxygen probe with the excitation source tuned to 870 nm produced the optimal results. Our *in vivo* demonstrations of the technique highlighted some of its capabilities. In particular, we demonstrated the ability to produce high-resolution three-dimensional images of the vasculature morphology and absolute velocity measurements in conjunction with PO_2 measurements. Additionally, we modified our

system to add speckle contrast imaging and photo-thrombosis capabilities. We used these new capabilities to produce acute focal ischemia models, which tested our system's ability to quantify the effects on oxygen transport.

FUTURE WORK

Although we have demonstrated that our two-photon microscopy setup is currently capable of producing detailed vasculature images, there are a few areas where improvements can easily be made. One such improvement would be to change the way we scan in the depth dimension. Currently, we use a stepper motor coupled to the fine focus knob and a Nikon focusing unit to translate the microscope objective up and down. We have had problems with the positional stability of this unit as it is not designed to carry the amount of weight that it currently supports in our microscope. Additionally, translating the microscope objective is not ideal in that there is an optimal location for the back aperture of the objective. Translating the objective therefore moves the back aperture out of the optimal location. As a consequence, the expanded excitation beam "walks" around the back aperture plane and produces vignetting on the image. We frequently see vignetting in our images as a result. A better way of scanning in the depth dimension would be to keep the back aperture fixed and translate the animal model up and down. The requirements for such a z-translation stage are not trivial, as it needs to move the weight of the animal and its immobilization frame with an accuracy of better than 1 μm. However, such translation stages are commercially available.

Another area for improving our microscope setup is to use a PMT that is sensitive over the entire emission spectrum of our PQO probe. From Figure 34, we can see that the sensitivity drops off rapidly near 700 nm, but the emission spectra of our probes

extend out to 730 nm. Our detection efficiency can be improved with a more appropriate choice of PMT such as Hamamatsu H10770PB-50. Modulating our excitation source with an electro-optic modulator (EOM), instead of the AOM that we currently use, is another way we could improve the instrumentation of our system. The transmission efficiency of our AOM is roughly 50%. The excitation power lost at the AOM limits how deep we can excite our PQO probe when the laser is tuned to longer wavelengths. EOMs have transmission efficiencies near 90%.

In addition to improving our imaging instrumentation, more work should be done in developing an *in vitro* calibration setup for our PQO measurements. A proper calibration setup would allow us to directly test the performance of our PQO probes under differing PO_2 conditions. We currently rely on the manufacturers of our PQO probes to provide the necessary calibration information. In theory, the calibration constants should remain constant over time. However, as was the case with the second sample of PtP-C343, there are occasionally instances where anomalous lifetimes are measured. A calibration setup would allow us to better investigate these occurrences. Furthermore, in chapter 5, I extrapolate SNR performance at various PO_2 conditions based on the SNR performance under anoxic conditions. A calibration setup would allow us to verify those predictions with direct measurements.

Future work on this project should also include development of an *in vivo* verification setup, which would allow our group to have greater confidence in the accuracy of our PO_2 measurements. A Clarke style PO_2 meter with a micro-tipped electrode (~ 10-20 μm diameter) should be used to obtain readings while we take measurements with our optical technique. To do this, an optical window protocol, which allows insertion of the micro-tipped electrode, should be used. A micro-manipulator

would be needed to accurately position the electrode tip in the lumen of a vessel within the imaging field of view.

More *in vivo* experiments need to be performed with the PtP-C343 PQO probe. Specifically, efforts should be made to figure out why the second sample produced such short lifetimes during *in vivo* measurements. Additionally, the project should start to shift over from the technique-development phase into the utilization phase. Now that our lab has a unique capability to measure PO_2, we can chose to start looking at the interesting research questions related to oxygen transport to cells. For instance, we might design experiments to characterize how acute ischemic events in the cortical vasculature impact PO_2 distribution and how this is correlated with loss of neural function.

Although it is not critical for this project, future work should also include investigation and publication of the mechanism behind the interfering luminescence. This is an area that could impact many researchers who perform two-photon imaging with excitation tuned to near 800 nm and with fluorophores that emit near 700

References

1. R. C. Mesquita, T. J. Huppert, and D. A. Boas, "Exploring neuro-vascular and neuro-metabolic coupling in rat somatosensory cortex," Physics in medicine and biology **54**, 175-185 (2009).
2. G. Strangman, D. A. Boas, and J. P. Sutton, "Non-invasive neuroimaging using near-infrared light," Biol Psychiatry **52**, 679-693 (2002).
3. A. Villringer, J. Planck, C. Hock, and L. Schleinkofer…, "Near infrared spectroscopy (NIRS): a new tool to study hemodynamic changes during activation of brain function in human adults," Neuroscience … (1993).
4. W. ARMSTEAD…, "Different cerebral hemodynamic responses following fluid percussion brain injury in the newborn and juvenile pig," Journal of neurotrauma (1994).
5. P. Mertes, K. Abassi, Y. Jaboin, and P. Burtin…, "Changes in hemodynamic and metabolic parameters following induced brain death in the pig," … (1994).
6. A. Villringer and B. CHANCE, "Non-invasive optical spectroscopy and imaging of human brain function," Trends Neurosci **20**, 435-442 (1997).
7. R. Grubb Jr, C. Derdeyn, and S. Fritsch…, "Importance of hemodynamic factors in the prognosis of symptomatic carotid occlusion," Jama (1998).
8. W. Shoemaker, D. Thangathurai, and C. Wo…, "Intraoperative evaluation of tissue perfusion in high-risk patients by invasive and noninvasive hemodynamic monitoring," Critical care … (1999).
9. A. G. Tsai, P. C. Johnson, and M. Intaglietta, "Oxygen gradients in the microcirculation," Physiol. Rev. **83**, 933-963 (2003).
10. M. Intaglietta, P. C. Johnson, and R. M. Winslow, "Microvascular and tissue oxygen distribution," Cardiovasc Res **32**, 632-643 (1996).
11. A. G. Tsai, B. Friesenecker, P. Cabrales, N. Hangai-Hoger, and M. Intaglietta, "The vascular wall as a regulator of tissue oxygenation," Curr Opin Nephrol Hypertens **15**, 67-71 (2006).
12. Q. Fang, S. Sakadzić, L. Ruvinskaya, A. Devor, A. M. Dale, and D. A. Boas, "Oxygen advection and diffusion in a three- dimensional vascular anatomical network," Optics express **16**, 17530-17541 (2008).
13. D. J. Heeger and D. Ress, "What does fMRI tell us about neuronal activity?," Nat Rev Neurosci **3**, 142-151 (2002).
14. A. Viswanathan and R. D. Freeman, "Neurometabolic coupling in cerebral cortex reflects synaptic more than spiking activity," Nat. Neurosci. **10**, 1308-1312 (2007).
15. N. K. Logothetis, "What we can do and what we cannot do with fMRI," Nature **453**, 869-878 (2008).
16. Y. Nir, I. Dinstein, R. Malach, and D. J. Heeger, "BOLD and spiking activity," Nat. Neurosci. **11**, 523-524; author reply 524 (2008).

17. B. M. Ances, D. F. Wilson, J. H. Greenberg, and J. A. Detre, "Dynamic changes in cerebral blood flow, O2 tension, and calculated cerebral metabolic rate of O2 during functional activation using oxygen phosphorescence quenching," J Cereb Blood Flow Metab **21**, 511-516 (2001).
18. K. A. Kasischke, H. D. Vishwasrao, P. J. Fisher, W. R. Zipfel, and W. W. Webb, "Neural activity triggers neuronal oxidative metabolism followed by astrocytic glycolysis," Science **305**, 99-103 (2004).
19. J. Sonn and A. Mayevsky, "Effects of brain oxygenation on metabolic, hemodynamic, ionic and electrical responses to spreading depression in the rat," Brain Res **882**, 212-216 (2000).
20. H. Piilgaard and M. Lauritzen, "Persistent increase in oxygen consumption and impaired neurovascular coupling after spreading depression in rat neocortex," Journal of Cerebral Blood Flow & Metabolism (2009).
21. Y. Huang and F. J. Giordano, "Chapter 13 oxygen as a direct and indirect biological determinant in the vasculature," Meth Enzymol **444**, 285-304 (2008).
22. C. deDeugd, M. Wankhede, and B. Sorg, "Multimodal optical imaging of microvessel network convective oxygen transport dynamics," Applied optics (2009).
23. H. Shin, A. Dunn, P. Jones, D. Boas, E. Lo, M. Moskowitz, and C. Ayata, "Normobaric hyperoxia improves cerebral blood flow and oxygenation, and inhibits peri-infarct depolarizations in experimental focal ischaemia," Brain (2007).
24. S. Liu, H. Shi, W. Liu, T. Furuichi, G. S. Timmins, and K. J. Liu, "Interstitial pO2 in ischemic penumbra and core are differentially affected following transient focal cerebral ischemia in rats," J Cereb Blood Flow Metab **24**, 343-349 (2004).
25. S. S. Velan, R. G. Spencer, J. L. Zweier, and P. Kuppusamy, "Electron paramagnetic resonance oxygen mapping (EPROM): direct visualization of oxygen concentration in tissue," Magn Reson Med **43**, 804-809 (2000).
26. K. Matsumoto and S. Subramanian…, "Electron paramagnetic resonance imaging of tumor hypoxia: enhanced spatial and temporal resolution for in vivo pO2 determination," … Resonance in … (2006).
27. J. M. Vanderkooi and D. F. Wilson, "A new method for measuring oxygen concentration in biological systems," Adv Exp Med Biol **200**, 189-193 (1986).
28. J. M. Vanderkooi, G. Maniara, T. J. Green, and D. F. Wilson, "An optical method for measurement of dioxygen concentration based upon quenching of phosphorescence," J Biol Chem **262**, 5476-5482 (1987).
29. D. F. Wilson, J. M. Vanderkooi, T. J. Green, G. Maniara, S. P. DeFeo, and D. C. Bloomgarden, "A versatile and sensitive method for measuring oxygen," Adv Exp Med Biol **215**, 71-77 (1987).
30. W. L. Rumsey, J. M. Vanderkooi, and D. F. Wilson, "Imaging of phosphorescence: a novel method for measuring oxygen distribution in perfused tissue," Science **241**, 1649-1651 (1988).

31. R. D. Shonat and A. C. Kight, "Oxygen tension imaging in the mouse retina," Annals of biomedical engineering **31**, 1084-1096 (2003).
32. R. D. Shonat and P. C. Johnson, "Oxygen tension gradients and heterogeneity in venous microcirculation: a phosphorescence quenching study," Am J Physiol **272**, H2233-2240 (1997).
33. S. Kimura, K. Matsumoto, K. Mineura, and T. Itoh, "A new technique for the mapping of oxygen tension on the brain surface," J Neurol Sci **258**, 60-68 (2007).
34. H. Kobayashi and N. Takizawa, "Imaging of oxygen transfer among microvessels of rat cremaster muscle," Circulation **105**, 1713-1719 (2002).
35. D. F. Wilson, W. M. F. Lee, S. Makonnen, O. Finikova, S. Apreleva, and S. A. Vinogradov, "Oxygen pressures in the interstitial space and their relationship to those in the blood plasma in resting skeletal muscle," J Appl Physiol **101**, 1648-1656 (2006).
36. M. Göppert-Mayer, "Über Elementarakte mit zwei Quantensprüngen," Annalen der Physik **401**, 273-294 (1931).
37. W. Denk, J. H. Strickler, and W. W. Webb, "Two-photon laser scanning fluorescence microscopy," Science **248**, 73-76 (1990).
38. W. R. Zipfel, R. M. Williams, and W. W. Webb, "Nonlinear magic: multiphoton microscopy in the biosciences," Nat Biotechnol **21**, 1369-1377 (2003).
39. E. G. Mik, T. G. van Leeuwen, N. J. Raat, and C. Ince, "Quantitative determination of localized tissue oxygen concentration in vivo by two-photon excitation phosphorescence lifetime measurements," J Appl Physiol **97**, 1962-1969 (2004).
40. J. R. Lakowicz, "Principles of Fluorescence Spectroscopy," in *Principles of Fluorescence Spectroscopy,* 3 ed. (Springer Science + Business Media, LLC, New York, NY, 2006), pp. 171,192-194.
41. S. A. Vinogradov, L. W. Lo, W. T. Jenkins, S. M. Evans, C. Koch, and D. F. Wilson, "Noninvasive imaging of the distribution in oxygen in tissue in vivo using near-infrared phosphors," Biophys. J. **70**, 1609-1617 (1996).
42. T. Itoh, K. Yaegashi, T. Kosaka, T. Kinoshita, and T. Morimoto, "In vivo visualization of oxygen transport in microvascular network," Am J Physiol **267**, H2068-2078 (1994).
43. M. Paxian, S. A. Keller, B. Cross, T. T. Huynh, and M. G. Clemens, "High-resolution visualization of oxygen distribution in the liver in vivo," Am J Physiol Gastrointest Liver Physiol **286**, G37-44 (2004).
44. W. Denk and K. Svoboda, "Photon Upmanship: Techreview Why Multiphoton Imaging Is More than a Gimmick," Neuron (1997).
45. P. S. N. Tsai, N.; Yoder, E. J.; Dolnick; White G. A.; Kleinfeld D., "Principles, Design and Construction of a Two-Photon Laser Scanning Microcope for *In Vitro* and *In Vivo* Brain Imaging," in *In Vivo Optical Imaging of Brain Function*, R. D. Frostig, ed. (CRC Press, 2002), pp. 113-172.

46. M. Oheim, E. Beaurepaire, E. Chaigneau, J. Mertz, and S. Charpak, "Two-photon microscopy in brain tissue: parameters influencing the imaging depth.," J. Neurosci. Methods **111**, 29-37 (2001).
47. E. Beaurepaire and J. Mertz, "Epifluorescence collection in two-photon microscopy," Applied optics **41**, 5376-5382 (2002).
48. R. P. Briñas, T. Troxler, R. M. Hochstrasser, and S. A. Vinogradov, "Phosphorescent oxygen sensor with dendritic protection and two-photon absorbing antenna.," J Am Chem Soc **127**, 11851-11862 (2005).
49. R. D. Shonat, K. Richmond, and P. Johnson, "Phosphorescence quenching and the microcirculation: An automated, multipoint oxygen tension …," Review of Scientific Instruments (1995).
50. M. Shibata, S. Ichioka, J. Ando, and A. Kamiya, "Microvascular and interstitial PO(2) measurements in rat skeletal muscle by phosphorescence quenching," J Appl Physiol **91**, 321-327 (2001).
51. L. Zheng, A. S. Golub, and R. N. Pittman, "Determination of PO2 and its heterogeneity in single capillaries," Am J Physiol **271**, H365-372 (1996).
52. R. D. Shonat, K. N. Richmond, and P. C. Johnson, "Phosphorescence quenching and the microcirculation: An automated, multipoint oxygen tension …," Review of Scientific Instruments (1995).
53. R. Yuste, F. Lanni, and A. Konnerth, "Imaging Neurons: A Laboratory Manual," (2000).
54. I. Dunphy, S. A. Vinogradov, and D. F. Wilson, "Oxyphor R2 and G2: phosphors for measuring oxygen by oxygen-dependent quenching of phosphorescence," Anal Biochem **310**, 191-198 (2002).
55. R. D. Shonat, E. S. Wachman, W. Niu, A. P. Koretsky, and D. L. Farkas, "Near-simultaneous hemoglobin saturation and oxygen tension maps in mouse brain using an AOTF microscope," Biophys. J. **73**, 1223-1231 (1997).
56. N. J. D. Durr, T. Larson, D. K. Smith, B. A. Korgel, K. Sokolov, and A. Ben-Yakar, "Two-Photon Luminescence Imaging of Cancer Cells Using Molecularly Targeted Gold Nanorods," Nano Lett. **7**, 941-945 (2007).
57. J. Park, A. Estrada, K. Sharp, K. Sang, J. A. Schwartz, D. K. Smith, C. Coleman, J. D. Payne, B. A. Korgel, A. K. Dunn, and J. W. Tunnell, "Two-photon-induced photoluminescence imaging of tumors using near-infrared excited gold nanoshells," Optics express **16**, 1590-1599 (2008).
58. G. Piszczek, B. Maliwal, and I. Gryczynski…, "Multiphoton ligand-enhanced excitation of lanthanides," Journal of … (2001).
59. M. Y. Berezin and S. Achilefu, "Fluorescence lifetime measurements and biological imaging," Chem Rev **110**, 2641-2684 (2010).
60. G. G. Blasse, B. C., *Luminescent Materials* (Springer-Verlag, Berlin, 1994), p. 232.
61. J. F. Suijver, "Upconversion Phosphors," in *Luminescence, From Theory to Applications*, C. Ronda, ed. (Wiley-VCH, 2008), pp. 133-178.

62. A. D. Estrada and A. K. Dunn, "Improved sensitivity for two-photon frequency-domain lifetime measurement," Optics express **18**, 13631-13639 (2010).
63. M. Drobizhev, F. Meng, A. Rebane, Y. Stepanenko, E. Nickel, and C. W. Spangler, "Strong two-photon absorption in new asymmetrically substituted porphyrins: interference between charge-transfer and intermediate-resonance pathways.," The journal of physical chemistry. B, Condensed matter, materials, surfaces, interfaces & biophysical **110**, 9802-9814 (2006).
64. O. Finikova, A. Lebedev, A. Aprelev, T. Troxler, F. Gao, C. Garnacho, S. Muro, R. Hochstrasser, and S. Vinogradov, "Oxygen Microscopy by Two-Photon-Excited Phosphorescence," Chemphyschem : a European journal of chemical physics and physical chemistry (2008).
65. S. Sakadžić, S. Yuan, E. Dilekoz, S. Ruvinskaya, S. A. Vinogradov, C. Ayata, and D. A. Boas, "Simultaneous imaging of cerebral partial pressure of oxygen and blood flow during functional activation and cortical spreading depression," Applied Optics, Vol. 48, Issue 10, pp. D169-D177.
66. D. F. Wilson, W. M. Lee, S. Makonnen, O. Finikova, S. Apreleva, and S. A. Vinogradov, "Oxygen pressures in the interstitial space and their relationship to those in the blood plasma in resting skeletal muscle," J Appl Physiol **101**, 1648-1656 (2006).
67. A. D. Estrada, A. Ponticorvo, T. N. Ford, and A. K. Dunn, "Microvascular oxygen quantification using two-photon microscopy," Optics letters **33**, 1038-1040 (2008).
68. I. Vanzetta and A. Grinvald, "Increased cortical oxidative metabolism due to sensory stimulation: implications for functional brain imaging," Science **286**, 1555-1558 (1999).
69. J. Van Houten and R. Watts, "… the photophysical and photochemical properties of the tris (2, 2'-bipyridyl) ruthenium (II) ion in …," J. Am. Chem. Soc (1976).
70. W. Zhong, P. Urayama, and M. Mycek, "Imaging fluorescence lifetime modulation of a ruthenium-based dye in living cells: the potential for …," JOURNAL OF PHYSICS-LONDON-D APPLIED PHYSICS (2003).
71. H. M. R. Gonçalves, C. D. Maule, P. A. S. Jorge, and J. C. G. Esteves da Silva, "Fiber optic lifetime pH sensing based on ruthenium(II) complexes with dicarboxybipyridine," Anal Chim Acta **626**, 62-70 (2008).
72. C. W. Chang, D. Sud, and M. A. Mycek, "Fluorescence lifetime imaging microscopy," Methods Cell Biol **81**, 495-524 (2007).
73. D. Sud and M. Mycek, "Calibration and validation of an optical sensor for intracellular oxygen measurements," Journal of biomedical optics (2009).
74. O. S. Finikova, A. Y. Lebedev, A. Aprelev, T. Troxler, F. Gao, C. Garnacho, S. Muro, R. M. Hochstrasser, and S. A. Vinogradov, "Oxygen Microscopy by Two-Photon-Excited Phosphorescence," Chemphyschem : a European journal of chemical physics and physical chemistry (2008).

75. P. T. So, C. Y. Dong, B. R. Masters, and K. M. Berland, "Two-photon excitation fluorescence microscopy," Annual review of biomedical engineering **2**, 399-429 (2000).
76. C. Xu and W. W. Webb, "Measurement of two-photon excitation cross sections of molecular fluorophores with data from 690 to 1050 nm," J. Opt. Soc. Am. **13**, 481 - 491 (1996).
77. F. Helmchen and D. Kleinfeld, "Chapter 10 in vivo measurements of blood flow and glial cell function with two-photon laser-scanning microscopy," Meth Enzymol **444**, 231-254 (2008).
78. A. Y. Shih, B. Friedman, P. J. Drew, P. S. Tsai, P. D. Lyden, and D. Kleinfeld, "Active dilation of penetrating arterioles restores red blood cell flux to penumbral neocortex after focal stroke," J Cereb Blood Flow Metab **29**, 738-751 (2009).
79. C. E. Brown and T. H. Murphy, "Livin on the Edge: Imaging Dendritic Spine Turnover in the Peri-Infarct Zone During Ischemic Stroke and Recovery," Neuroscientist (2007).
80. I. R. Winship, N. Plaa, and T. H. Murphy, "Rapid astrocyte calcium signals correlate with neuronal activity and onset of the hemodynamic response in vivo," J Neurosci **27**, 6268-6272 (2007).
81. S. Zhang and T. H. Murphy, "Imaging the Impact of Cortical Microcirculation on Synaptic Structure and Sensory-Evoked Hemodynamic Responses In Vivo," PLoS Biol. **5**, e119 (2007).
82. I. R. Winship and T. H. Murphy, "In vivo calcium imaging reveals functional rewiring of single somatosensory neurons after stroke," J Neurosci **28**, 6592-6606 (2008).
83. R. Mostany and C. Portera-Cailliau, "A Craniotomy Surgery Procedure for Chronic Brain Imaging," J Vis Exp, e680 (2008).
84. W. B. and G. M. D., " Induction of Reproducible Brain Infarction by Photochemically Initiated Thrombosis " Ann Neurol **17**, 497-504 (1985).
85. B. Friedman, P. Lyden, F. Ebner, and D. Kleinfeld, "All-optical thrombotic stroke model for near-surface blood vessels in rat: focal illumination of …," … III. Edited by Neev (2003).
86. D. A. Boas and A. K. Dunn, "Laser speckle contrast imaging in biomedical optics," Journal of biomedical optics **15**, 011109 (2010).
87. H. Hou, O. Y. Grinberg, S. Taie, S. Leichtweis, M. Miyake, S. Grinberg, H. Xie, M. Csete, and H. M. Swartz, "Electron paramagnetic resonance assessment of brain tissue oxygen tension in anesthetized rats," Anesthesia & Analgesia **96**, 1467 (2003).